Title
Integration of Lithography and DNA Mediated Self-Assembly for the Synthesis of Responsive Metamaterials

Author
Litt, David B.

Publication Date
2017

Peer reviewed|Thesis/dissertation

Integration of Lithography and DNA Mediated Self-Assembly for the Synthesis of Responsive Metamaterials

By

David B. Litt

A dissertation submitted in partial satisfaction of the

requirements for the degree of

Doctor of Philosophy

in

Chemistry

in the

Graduate Division

of the

University of California, Berkeley

Committee in charge:

Professor A. Paul Alivisatos, Chair

Professor Matthew B. Francis

Professor Hayden Taylor

Spring 2017

Abstract

Integration of Lithography and DNA Mediated Self-Assembly for the Synthesis of Responsive Metamaterials

by

David B. Litt

Doctor of Philosophy in Chemistry

University of California, Berkeley

Professor A. Paul Alivisatos, Chair

Dynamic materials have always held the interest of scientists because they change their properties in response to some stimulus. Being able to program the desired material properties before and after a stimulus is important to many sensing technologies. One interesting class of materials are termed 'metamaterials' because they interact with light in exotic ways that naturally occurring materials do not. These engineered materials are able to interact with light (or other frequencies of electromagnetic waves) in novel ways is due to the low symmetry arrangement of their components. In order to achieve the low symmetry arrangement, lithographic techniques are commonly used to fabricate these materials, because lithography can arrange nanoscale components in arbitrary patterns. However, most lithographed materials are static and do not react to external chemical stimuli. This dissertation lays out a novel approach to rationally assemble dynamic metamaterials by combining lithographic techniques with DNA mediated self-assembly, which imparts a responsive, organic component to the metamaterial.

Integrating DNA into a metamaterial allows for several advancements over lithographed-only metamaterials. First it allows for sub-nanometer control over the spacing of the constituent components. Second, DNA is responsive to a wide variety of stimuli—such as other DNA strands, salt, proteins, certain organic molecules, and temperature. Depending on the stimuli, one could then program a single metamaterial to respond in divergent ways to different chemical stimuli.

The model metamaterial examined here is a three nanorod system that exhibits a property known as electromagnetically induced transparency (EIT). Two rods are defined with lithography, and the third is assembled with DNA. This hybrid organic-inorganic structure behaves in accordance to plasmon hybridization theory and finite difference time domain (FDTD) simulations. Finally, external chemical stimuli, such as removing sodium cations or dehydrating the DNA, can cause the components to either decouple or couple more strongly, causing the EIT effect to either disappear or become enhanced, respectively. This assembly method allows for creating of dynamic metamaterials that can be predictably perturbed in order to change their desired optical properties.

Acknowledgements

I would first like to thank my grandfather, Professor Emeritus Morton H. Litt, who gifted me many books that opened my eyes to the wonders of science.

I thank my mentors in the Alivisatos group, Dr. Mario Hentschel and Dr. Matthew R. Jones, for giving me guidance and helping to shape my scientific career.

I want to thank Matthew Koc, Dr. Son Nguyen, Dr. Xincheng Ye, Dr. Sui Yang, Ying Wang, and Hyun Dong Ha for their help throughout my time in graduate school.

I would like to thank Greg Mullins and Dr. Kathy Durkin for help with nanofabrication and simulations, respectively. I would also like to thank Dr. Noah Bronstein for giving me the advice to “just make a decision”.

I would also like to thank my friends (Andrew, Daniel F., Daniel L., Daniele, Erin, Hoduk, Laura, Marissa, Paul, Sophie, Tamara, Tobias and others) and family (Maria, Jonathan, Daniel, Michael, Lola and Eugenia) for their great help and support over the last five years.

Finally, I would like to thank Professor A. Paul Alivisatos for his support and for the pieces of wisdom he lets slip every year at the group retreat at Point Reyes. Two that have stuck with me are that the purpose of graduate school is to learn how to create a “new unit of knowledge”, and that “interesting science happens on the interfaces of different fields”. I hope that this thesis has succeeded at doing both those things.

Table of Contents

List of Figures

List of Tables

Chapter 1 : Introduction

Chemistry is a field that asks fundamental questions about interactions. How do atoms and molecules react to form new complexes and substances? What are the properties of these new materials—that is, how do they interact with light, other molecules and other particles? How do they behave?

A lot of research in chemistry is therefore fundamental, and concerns itself with the "how" and "why" questions. Some of these questions led to discoveries about how exotic materials work, from magnetic lodestones to birefringent Iceland spar (calcite).[1,2] After the groundwork is laid down and understood, chemists then begin to ask the "what" questions. Specifically, "what properties are interesting?" or "what can we synthesize or create that would be useful", and "what can be done to improve on the properties of naturally occurring materials"?

To answer the first question—"what properties are interesting?"—one can look to the study of nanoscience as an example. Nanoscience is predicated on the fact that materials that are about one to one hundred nanometers (nm) in size have very different properties than the same material on the bulk scale.[3,4] For example, semiconductor quantum dots are one of the first examples of quantum confined objects that exist on size scales much larger than one would normally expect to see quantum phenomena. That is, it is an object made out of hundreds to thousands of atoms that behaves like a particle in a box; the larger the particle is, the redder its emission is. Some metals also follow this size dependent trend on the nanoscale. In the study of plasmonics, gold and silver (and to some extent copper and aluminum) will absorb and scatter different wavelengths of light in a size-dependent manner.[5]

To answer the follow up questions—"what can we synthesize or create that would be useful?", and "what can be done to improve on the properties of naturally occurring materials?", we can think of taking the nanoparticles that we have already studied, and putting them in complex arrangements that change their properties. This is nothing new; some of the most exciting work that tries to deal with these "what" questions is research on stimuli responsive molecules and materials. Upon a stimulus, the molecule or material will change its properties, and behave in a different, predictable, and useful manner.

From the simplest azobenzene and spiropyran systems to the most complex DNA origami assemblies, functional materials are a burgeoning field with a wealth of applications from sensing and diagnostics to physics.[6,7] More recently, a form of engineered structures, called metamaterials, have captured the imagination of scientists because they display properties not found in any known naturally occurring material. These properties include negative index materials, slowing light, invisibility cloaks, and more.[8–11] The way these materials interact with electromagnetic radiation is of great interest to the scientific community. The purpose of this thesis is to increase the functionality of these materials, to expand the range of interactions a single fabricated material can have, and create a methodology that enables us to chemically switch between multiple functional states of the metamaterial.

This thesis is broken into six subsequent chapters. Chapter 2 gives general background on the motivation and theory for the metamaterial herein discussed. Chapter 3 discusses the lithography techniques traditionally employed to fabricate metamaterials. Chapter 4 covers colloidal nanoparticle synthesis, which is used to fabricate the dynamic component of the metamaterial. Chapter 5 covers DNA mediated self-assembly, which is used to complete assembly of the metamaterial and to impart dynamics to the material. Chapter 6 discusses the spectrographic analysis of this functional material, illustrating how the metamaterial responds to chemical and environmental stimuli. Finally, Chapter 7 looks to the future for these types of materials.

Chapter 2 : Plasmonics and Theory

The forward movement of science depends on having a strong motivation and understanding of the underlying principles. If one wants to design a responsive metamaterial, a next-generation plasmon ruler, a DNA sensing platform, or anything of interest, we need to understand what has been done, how it has been done, and what is next. We also need to ask ourselves why the "what is next" has not already been done. What are the theoretical or technical challenges that we will face going forward? This chapter will cover the basics in the field of plasmonics, as well as explore the underlying theory of metamaterials exhibiting an effect known as electromagnetically induced transparency (EIT).

2.1 Plasmonics: Light-Matter Interactions in Metals

A plasmon occurs when electromagnetic radiation interacts with the conduction electrons in a material, causing the electrons to oscillate in such a way that creates a net dipole on the material.[5] In the scope of this work, the electromagnetic radiation is in the visible and near infrared frequencies, and is interacting with gold nanoparticles assembled in low symmetry arrangements. Basically, the conduction electrons in the metal nanoparticle oscillate at a specific natural resonance. When a light source of the same frequency as the natural resonance of the electron cloud impinges upon the particle, it drives this oscillation. During this oscillation, the electrons cause an electric dipole on the particle as they cluster on one side of the particle. This dipole creates a restoring force, pulling the electrons toward the other, positively charged, side of the particle, and continuing the oscillation (Figure 2.1). This interaction between the electron cloud and the impingent light wave causes the light to either be absorbed or scattered.

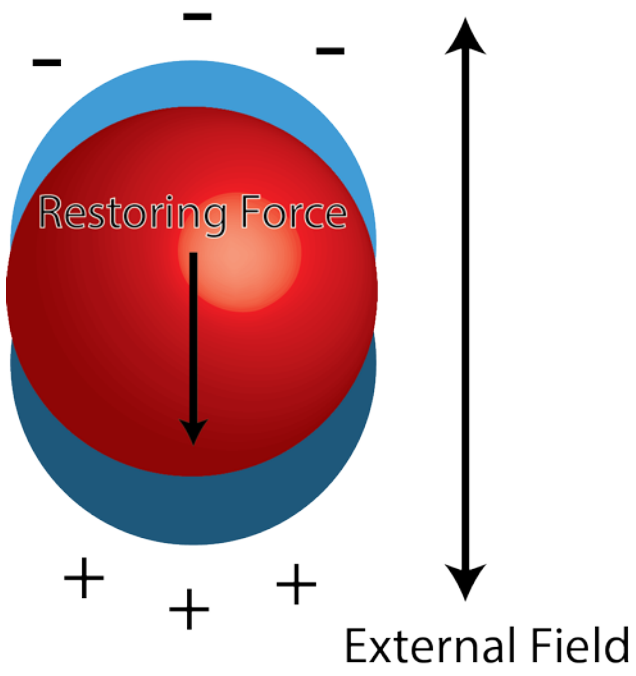

Figure 2.1: Plasmon resonance schematic. A plasmon is caused by light impinging on a material (red sphere) with loosely held electrons. When the electron cloud oscillates (blue), a dipole is created across the particle, causing the electrons to periodically change direction and to continue to oscillate as long as they are being driven by the external field.

This oscillating motion, caused by a restoring force, immediately calls to mind a mass-and-spring model. Unsurprisingly, the mass-and-spring model can qualitatively be used to model plasmonic particles. A more mathematically rigorous method involves solving Maxwell's equations because plasmons are electromagnetic in nature, but the mass-and-spring model is the one of the simplest and most elegant ways to understand plasmons.[12] The "mass" in this case is the mass of the electron could, *m*, which is the mass of all the electrons in the particle. It is calculated my multiplying the rest mas of an electron, m_e, by the carrier density, *n*, the cross-sectional area of the nanoparticle, *A*, and the distance of the oscillation, *d* (m=$n*m_e*A*d$). This electron cloud mass is mostly invariant with nanoparticle size because electrons are not particularly massive. The spring constant of the restoring force, *k*, does vary with size because the distance between the two ends of the dipole varies with size. This variation occurs because the farther apart the positive and negative ends of the dipole are, the weaker the electrostatic attraction becomes, and the smaller *k* becomes. One way to think about it is that the further the ends of the nanoparticle are, the weaker the coloumbic attraction is between the negatively and positively charged sides of the nanoparticle because coulombic attraction is inversely proportional to the square of the distance. One can also imagine the dipole as a rubber band or a guitar string—the closer the ends of the dipole are, the more taught the rubber band or string is, and the faster it vibrates or oscillates. The farther apart the ends of the dipole are, the less taught the rubber band or string is, and it will oscillate at a lower frequency. The resonant frequency, ω_{res}, is just the root of the spring constant over the electron cloud mass (Equation 1).

$$\omega_{res} = \sqrt{\frac{k}{m}} \propto \sqrt{\frac{k}{m_e}} \tag{1}$$

The restoring force that drives the oscillation obeys Hooke's Law. In the mass and spring model, the restoring force, F, is equal to the spring constant, *k* times the distance between the ends of the dipole, *x* (Equation 2). Though it should be pointed out that because we are dealing with electrons and protons, we are dealing with coulombic potentials (force is proportional to $1/r^2$) the expression for *k* is quite involved.[12]

$$\vec{F} = -k\vec{x} \tag{2}$$

The simplest case is that of a sphere. For instance, 5 nm gold spheres exhibit a resonance at about 520 nm. If the size of the nanoparticle is increased to 50 nm, the resonance correspondingly redshifts.

If we decide that spheres are too simple for our tastes, we can then examine more anisotropic shapes, such as rods. In this case, we have the longitudinal (long) axis, and the transverse (short) axis. To reiterate, changing the size of the particle can be thought of as changing the spring constant. As this spring constant changes, the resonant frequency changes with it in a predictable manner (Equation 3). In the case of a rod the resonant frequency is:

$$\omega_{res} = \frac{\omega_p}{2\sqrt{2}} \frac{1}{R} \tag{3}$$

Where R is the aspect ratio, and ω_p is the plasma frequency in the bulk material.[12] As can be seen from the equation, as the aspect ratio increases, the resonance should decrease in energy. Ergo, if spectra were taken of four rods of different aspect ratios, one would expect the longitudinal resonances to red-shift as the aspect ratio increases, which is seen experimentally (Figure 2.2).

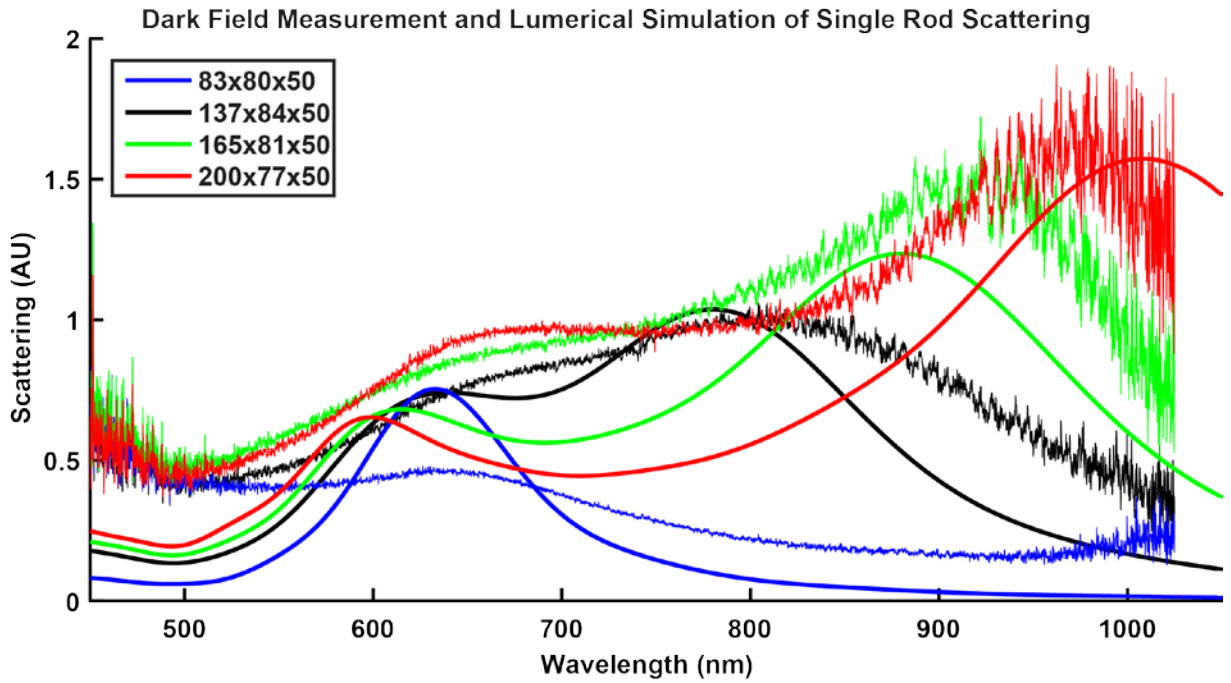

Figure 2.2: Dark field spectra and FDTD simulation of lithographed gold nanorods. As the rods get larger (blue, black, green, red), the longitudinal resonance redshifts. The transverse mode is slightly greater than 600 for all the rods. The thick solid lines are the simulation results from Lumerical FDTD with light polarized along the short and long axis. The dark field spectra (thin lines) were taken with unpolarized light.

Now that we have discussed isolated spheres and rods, we should examine the case when two plasmonic particles are brought close together. In this case, the plasmons couple; that is, if they are close (about one diameter's length away from one another) their electromagnetic fields are able to interact, changing the overall resonance frequency of the nanoparticles. Perhaps the easiest way to visualize this is to model it after hybrid orbital theory (Figure 2.3). In this case, two identical, isolated plasmons (that have an electric dipole) of a certain energy are separated at a large distance. When they are brought closer together, the electromagnetic dipoles can couple in two ways. The first way is to have a (+ -) (+ -) arrangement, which is low energy because the charges are always alternating (in an attractive manner) and has a net dipole. This is analogous to a bonding orbital. The second arrangement (- +) (+ -) is a high energy state because there is a strong repulsive component from the two like charges being near each other. This anti-bonding like orbital also has no net dipole. The plasmonically active mode is simply the one that has a net dipole, which for the case of spheres is the low energy mode. This leads to a red shifting of the resonance to a lower energy. Other shapes and configurations have high energy modes that are plasmonically active, which leads to a blue shift of the plasmon resonance when the plasmonic particles couple. The plasmonically inactive modes are considered to be so-called 'dark' modes because they should not be excited by light and do not contribute to the optical spectra.

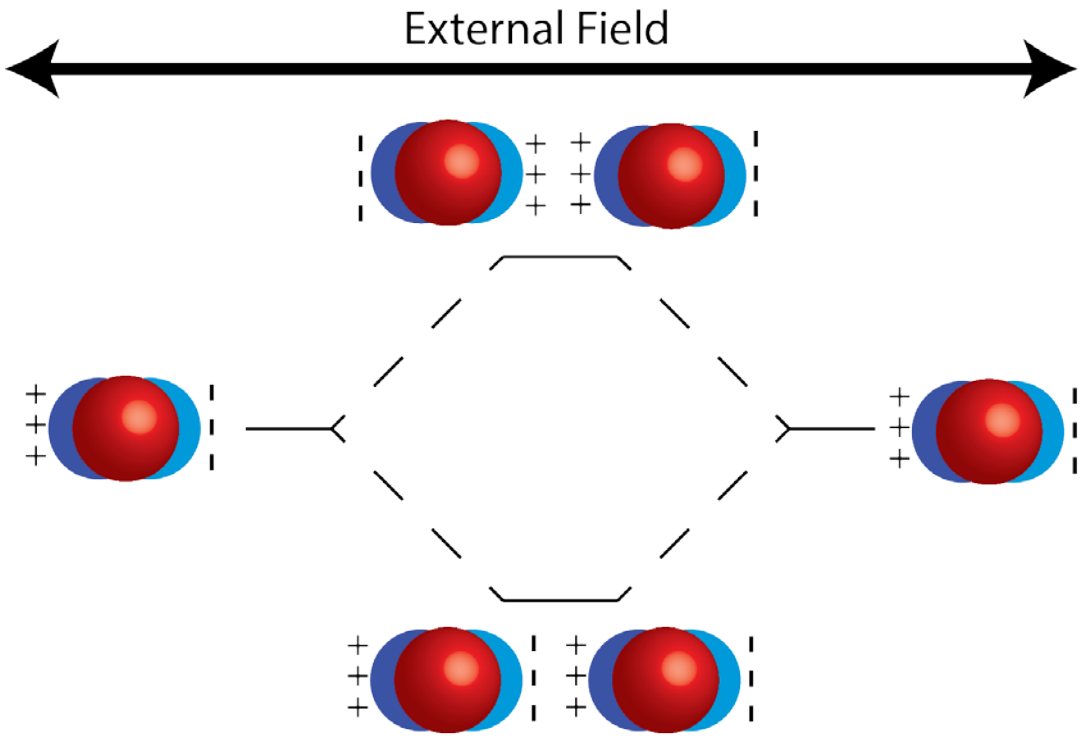

Figure 2.3: Plasmon hybridization model. When two identical plasmonic particles (red) are isolated, their energies are equal. When they are brought together, they can couple in two ways. Either they can have a net dipole (bottom, low energy mode) or no net dipole (top, high energy mode). Because plasmons need a net dipole (so there can be a restoring force and therefore an oscillation), then in this case the low energy case represents the plasmonic coupling and there is a red shift when two plasmonic spheres are brought together.

Anisotropic rods are unsurprisingly more complex than the isotropic spheres, and as a result, the polarization of the incident light will play a major role in how the rods couple and whether this coupling results in a red or blue shift of the rods.

For rods aligned in a tip-to-tip direction with the incident light polarized along the longitudinal axis, the behavior will be similar to that of two spheres (Figure 2.4) However, for two rods aligned side-by-side (with the incident light still in the longitudinal direction), the dipole is seen in the high energy form of the hybridization model, and there will actually be a blue shift in the spectra of this assembly (Figure 2.5).

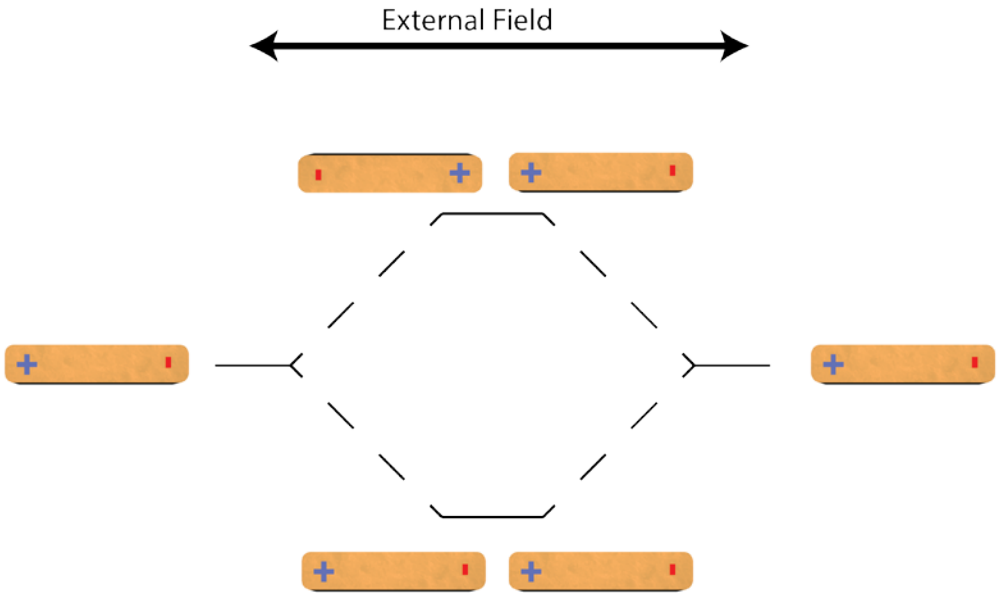

Figure 2.4: Hybridization model for two tip-to-tip rods excited along the longitudinal axis. Like the case of spheres, the 'bonding', low energy mode is a dipole, and the 'anti-bonding' mode is not a dipole. Therefore, if two rods align in this way, we expect to see a red shift in the plasmon peak.

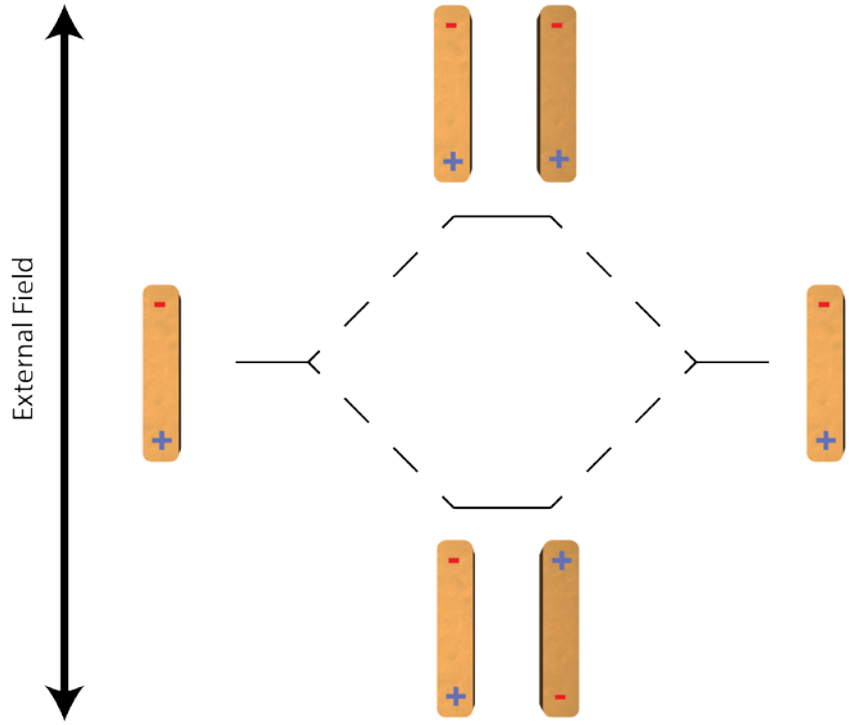

Figure 2.5: Plasmon hybridization model for two side-to-side rods excited along their longitudinal axis. In this case, the high energy 'antibonding' mode is a dipole, so a blue shift is expected when two rods align in this way. The low energy 'bonding mode' is a quadrupole resonance, and does not display a net dipole, and is thus a 'dark' mode. However, it is this quadrupole mode that is extremely important for metamaterials that exhibit electromagnetically induced transparency.

So far we have only discussed simple, dipolar resonances. There are higher order electromagnetic modes, such as a quadrupole. In the case of identical, parallel rods, the quadrupole mode has no net dipole, and is not plasmonically active. It is thus considered a 'dark mode' (Figure 2.6). However, this quadrupole resonance is very important for making metamaterials that exhibit electromagnetically induced transparency, which will be discussed in detail later (see Section 2.2.1).

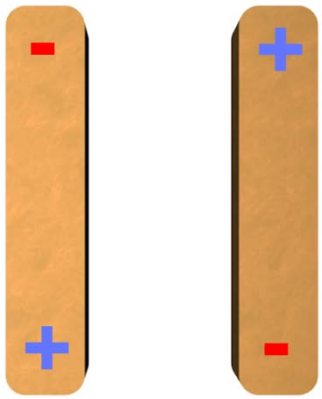

Figure 2.6: Quadrupolar resonance on two parallel rods. This resonance does not have net dipole, and is plasmonically "dark".

In summary, plasmons are a facile and well understood tool to explore interactions of light with certain metals, and plasmonic metals are an ideal candidate material for creating a metamaterial.

2.2 Metamaterials

Now that we understand the basics of plasmonics we can begin to appreciate how light and matter interact with each other, and by engineering materials, we can control this interaction. Metamaterials are engineered objects that interact with light in ways that are not seen in naturally occurring materials. Many kinds of metamaterials have been made to interact with electromagnetic radiation ranging from radio waves down to visual wavelengths.[8] These metamaterials demonstrate exotic behavior such as negative index of refraction, slowed light, and other interesting phenomena. I will focus on a specific property known as "electromagnetically induced transparency" as that is the basis of this thesis.

It should be noted that in order to engineer the material to interact exotically with light, the constituent parts should be placed in low symmetry arrangements. To do this, lithographic procedures are used, so even though the final material exhibits exotic behavior, it is a static structure (see Chapter 3).

2.2.1 Electromagnetically Induced Transparency

Electromagnetically induced transparency (EIT) is a phenomenon that was first seen in atomic systems, where one can cause destructive interference in a three level atom in such a way that what is normally a strong absorption feature no longer absorbs, and is instead transparent.[13–16] In our case, we are studying a plasmonic analogue of an atomic EIT system. It has been described extensively using mass-spring models, LC circuit models, and plasmon hybridization models. For simplicity and consistency with the previous section, I will use the plasmon hybridization model

to explain this effect in this thesis. This system was first created using lithographic techniques by the Zhang group in 2008, with three rods in a plane.[17] In 2009, Na Liu, who was in the Giessen group at the time, created the system that is used here, using two parallel rods with an orthogonal rod bridging them.[15] She later expanded this system to a more sensitive five rod system in 2011, and modeled the response of this system to small perturbations in the relative positions of the five rods and angular changes.[18]

The structures used in this work most closely follow the 2009 design, but the three rods were made smaller to shift the resonances to the visible and near IR so they could be detected with a Si CCD detector attached a dark field microscope (see Chapter 6). The base of the structure consists of two parallel rods that have a dark quadrupolar resonance (it is not plasmonically active due to the orthogonal polarization of incident light). When an orthogonal rod bridges the parallel rod across at center in an 'H' shape, it sits in the node of the parallel rods' quadrupolar resonance and EIT is not seen. If the orthogonal rod bridges the parallel rods near their tips in a 'Π' shape, then the dipolar resonance of the orthogonal rod can couple into the quadrupolar mode, and due to the plasmon hybridization the EIT peaks can be seen (Figure 2.7 and Figure 2.8). It should be noted that to excite the EIT resonances, incident light must be polarized along the orthogonal rod.

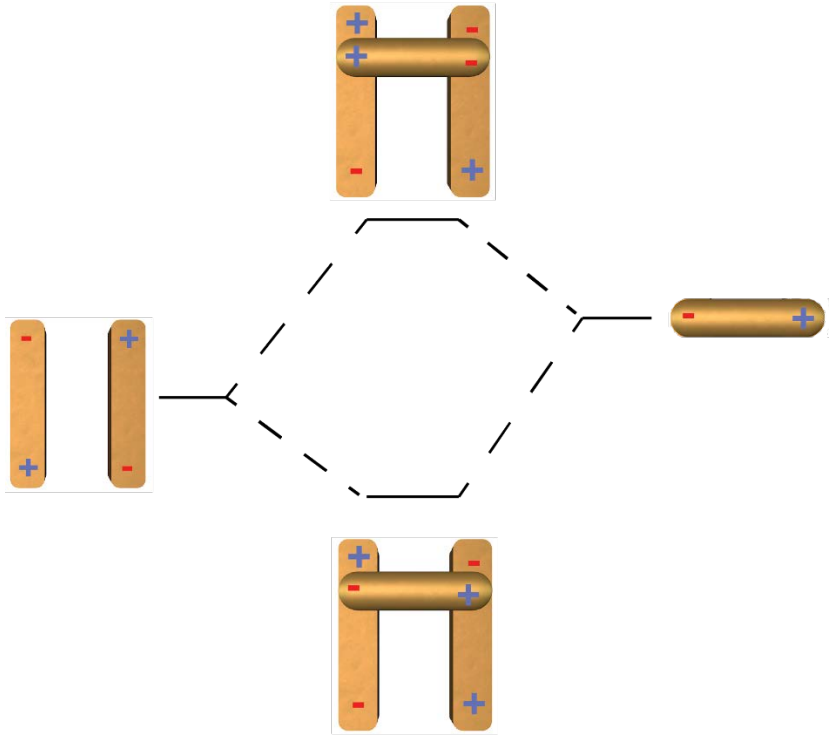

Figure 2.7: Plasmon hybridization model for EIT structures. The orthogonal rod's dipole mode is higher energy than the parallel rods' quadrupole mode (remember that the quadrupole mode is the lower energy bonding mode for two side by side rods). The resonances for the bonding and antibonding modes are shown and are plasmonically active (both have a net dipole). The incident field is polarized along the orthogonal rod.

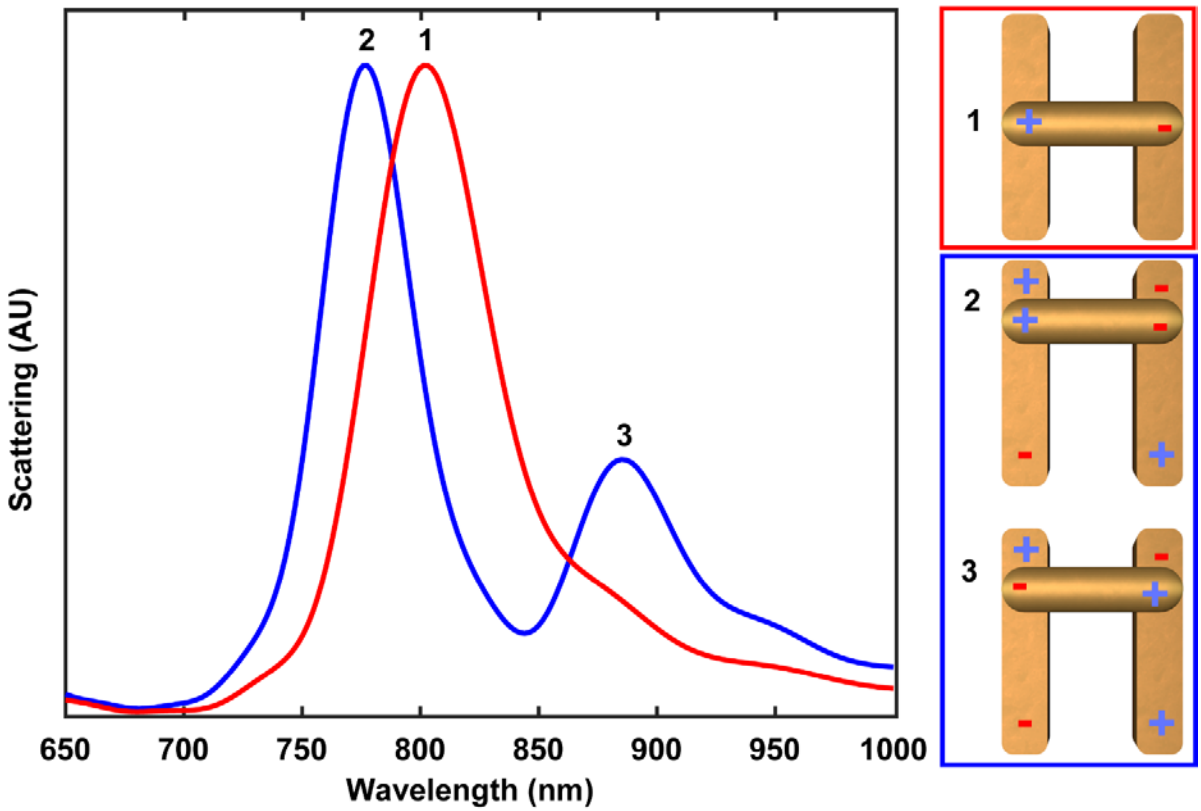

Figure 2.8: FDTD simulation of the three rod system. The symmetric 'H' Structure (red box and red peak, 1) does not exhibit EIT because the orthogonal rod is sitting in the node of the quadrupolar resonance, and cannot couple with it. However, the low symmetry 'II' structure (blue box and peaks 2 and 3), does exhibit EIT due to the dipolar resonance of the orthogonal rod coupling with the quadrupolar mode of the parallel rods.

2.3 Finite Difference Time Domain (FDTD)

In order to accurately predict the positions of the peak and have more than just a qualitative understanding of the trends, one actually has to solve Maxwell's equations. Such modeling is tremendously useful in designed materials that are programmed to interact with a particular frequency of light. To do this, we employ finite difference time domain (FDTD) simulations, though other methods exist, such as discrete dipole approximation and boundary-element methods.[5]

The FDTD algorithm was first developed in 1966 by Kane Yee.[19] Because the math involved is beyond the scope of this thesis, the general idea will be loosely summarized, and then the simulations of the metamaterials will be discussed in greater detail. Briefly, the FDTD algorithm solves for how incident light will interact with a material in a time evolving way, and allows for absorption, scattering, transmission, reflection, and electromagnetic modes to be accurately modeled and predicted. It does this by making a three dimensional grid around the particle of interest, and explicitly solving Maxwell's equation for the electric and magnetic fields in time and space for each voxel. The boundary conditions for the grid are set so that it is highly absorbing, and the light does not re-interact with the particle in a non-physical way.[5]

Lumerical FDTD was used in both at the beginning and the end phases the project. At first, simulations were used to sweep the parameter space of potential three rod structures to determine the optimal dimensions of the assembly. This encompasses length, width, height and gap distance of parallel rods and the radius and length of the orthogonal rod, as well as the surface to surface distance between the parallel and orthogonal rods. (The surface to surface distance of 15 nm was constrained by the length of the purchased double stranded DNA linker.) The preliminary simulations resulted in the following dimensions (Table 1):

Table 1: Optimal theoretical parameters for EIT structures from FDTD parameter sweep

Name	Length (nm)	Width (nm)	Thickness (nm)	Gap (nm)	Distance (nm)
Parallel Rods	120	35	35	30	NA
Orthogonal Rods	100	30	30	NA	15

Due to experimental limitations with DNA based assembly (Figure 5.14), the parallel rods were redesigned to be thinner and shorter than what is optically optimal. Because of additional experimental limitations, there is inherent variation in size in every nanorod (both lithographed and colloidally made) in every structure. In order to correlate dark field spectroscopy, scanning electron microscopy (SEM), and FDTD simulations, the dimensions of the actual nanorods were taken from the SEM images of the assemblies and used in the simulations (Table 2).

Table 2: Optimal parameters for EIT structures with experimental constraints.

Name	Length (nm)	Width (nm)	Thickness (nm)	Gap (nm)	Distance (nm)
Parallel Rods	115	35	30	30	NA
Orthogonal Rods	96	30	30	NA	15

EIT structures were simulated using the Lumerical FDTD software using the following parameters. The simulations were run with a mesh accuracy of 8 (‘very high accuracy’) with a 1 nm minimum mesh step. The lighting source is a total field scattering field source (TFSF) that is polarized along the longitudinal axis of the orthogonal rod. We used this light source as it only simulates the scattering spectra (as opposed to the extinction spectra, which is scattering and absorbance), as the dark field microscope only measures scattering. The refractive index was approximated as 1.33 (the refractive index of water). The gold material used for the parallel rods and the orthogonal rod is Johnson and Christy. We use PML boundaries in all simulations. The orthogonal rod was approximated by a cylinder with spheres capping both ends (Figure 2.9).

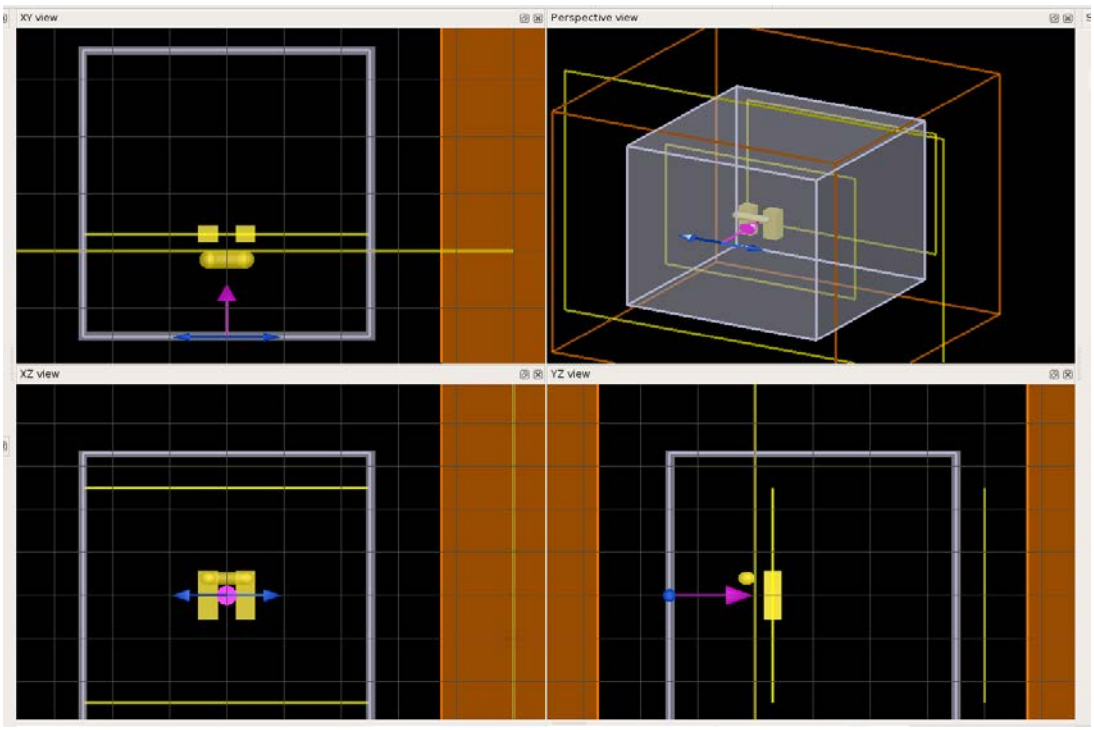

Figure 2.9: Screenshot of Lumerical FDTD simulation.

For simulations of dry samples, the dimensions and angles of the parallel rods and orthogonal rod were extracted from the SEM image, and plugged into Lumerical. For hydrated samples, the orthogonal rods were estimated to be about 15 nm from the surface of the parallel rods, and were allowed a few nanometers worth of rotation and lateral movement from the SEM image (the DNA can collapse and change shape during dehydration, so we assume that the position of the orthogonal rod in the dry state can be slightly different than the orthogonal rod while it is hydrated).

In summary, a complete picture of the target structure can be understood and simulated by having a solid understanding of the underlying theory. Once data is collected, the theory and simulations can be refined to more accurately describe the empirical data.

Chapter 3 : Lithographic and Metrology Techniques

In order to create a metamaterial, the components of the system must be arranged in a symmetry broken architecture. The most common way of doing this for metamaterials that interact with electromagnetic radiation in the optical regime is to use lithographic techniques. This chapter will focus on the tools I used in my thesis work: electron beam lithography, metal evaporation, and scanning electron microscopy (SEM). These represent only a few lithographic techniques that can be used to create low symmetry materials.

3.1: Electron Beam Lithography

Electron beam (e-beam) lithography is a technique used to write very small features on a polymer resist. It is a widely used technique because it is one of the highest resolution techniques available to researchers, and many cleanrooms have e-beam tools that can write lines as thin as ten nanometers with ten nanometer gaps separating them. Furthermore, under ideal operating conditions, multi-layer exposures can be made with ± 10 nm accuracy in both the x and y directions. This accuracy is vital for making nanostructured metamaterials small enough to interact with light in the optical frequencies (recall from Chapter 2 that as particles increase in size, many of the resonances correspondingly redshift). E-beam lithography will be necessary in order to fabricate a structure that exhibits EIT in the optical regime.

The e-beam tool is simply a modified SEM (discussed in section 3.3). The researcher first makes a desired pattern to expose using a CAD program such as L-edit (generally used by the community) or CABL-2000 (which was used for this work, as the e-beam tool is made by CRESTEC Japan, and CABL is their custom software). This program is fed into a pattern generator, and the e-beam tool sweeps the pattern over the substrate, exposing those (and hopefully only those) areas to the electron beam. However, this picture is rather simplistic, and there are many considerations to be made at each step of the process if a good exposure is to be made.

The first step is to identify the substrate to be used. The most common substrate is a Si wafer as many lithography tools were invented and developed for the semiconductor industry. For optical applications however, we want an optically transparent substrate so we can shine light on our metamaterial, making glass (SiO_2) and ideal candidate. However, glass is an insulator, so during the writing process incident electrons would hit the surface and stick there, making the surface negatively charged. This causes the negatively charged electron beam to deflect away from its programmed path, and deviate from exposing the desired features. One option to work around this is to spin coat a conductive polymer on top of the resist to whisk the electrons away from the writing area.[20] Another option is to evaporate a thin layer of a conductive metal on the substrate.[9] For this work, both were attempted, but I found a thin (10 nm) layer of indium tin oxide (ITO) worked best for the multi-layer exposures, as the conductive polymer could sometimes obscure the alignment markers under non-ideal conditions. Many researchers, however, have found the opposite, so each researcher should try both ways to find what works best for them.[5]

The second step is to identify a polymer resist that will react with electrons, such a poly(methyl methacrylate) (PMMA). This resist is spin coated and baked on a conductive substrate, and placed in the e-beam tool. The tool then exposes a predetermined pattern of the substrate to a stream of high energy electrons. PMMA is a positive resist, which means that the areas of the polymer that

were exposed to the electrons can be removed by development in certain solvents, while the unexposed regions stay intact. Other so-called negative resists have the property that the exposed areas remain, while the unexposed resist is washed away. (Under higher doses, PMMA can crosslink and act as a negative resist, but for this work PMMA was used as a positive resist.[21]) The two major properties of a resist (other than its positive or negative tone) are its final thickness after spin-coating, and molecular weight. The thickness will determine the amount of electrons that are needed to properly expose the feature; in order for the shape to be written, the entire polymer from top to bottom must be exposed so it can be later washed away. The resist thickness will also play a role in the evaporation step, as the maximal thickness of an evaporated metal can only be about half the height or less of the thickness of the resist (this will be expanded upon in section 3.2). The molecular weight of the polymer resist will also affect the dose required. The higher the molecular weight of the polymer, the more dose is required to break the covalent bonds in the polymer for the exposed areas to be washed away. Therefore, many higher molecular weight resists are referred to as low sensitivity resists, whereas low molecular weight resists are highly sensitive to the electron beam.[5]

The third step is to conduct a dose test. This entails the desired pattern to be written multiple times on the substrate with slightly different exposure times. At low doses, the pattern will be 'under exposed', that is, only some of the polymer resist will be exposed, but the trench won't reach all the way to the substrate, and no feature will be seen after development. At the other end of the spectrum, the pattern will be 'over exposed', and the features will be much too large. Finding the optimal region requires trial-and error. Often, researchers will find that 'under-sizing and over-dosing' helps find the correct final size. This means that a design will have the features slightly smaller than desired are exposed to a dose large enough that the developed features will have the correct proportions. One of the biggest problems that one encounters during a dose test of densely packed features is that of electron scattering. In this case, electrons will scatter off the polymer in a lateral direction and expose other areas of the resist that were not intended to be exposed. This causes features to be larger than planned, and is called a 'proximity effect'.[22] Researchers can use commercially available software, such as BEAMER® to help model these effects and modify doses to help eliminate these proximity effects.

The final step is development of the resist. In the case of PMMA, a 1:3 mixture of methyl isobutyl ketone (MIBK) to isopropanol (IPA) is used to wash away the exposed PMMA, while leaving the unexposed PMMA intact.

It is important to keep in mind that if the features being written are particularly thin compared to the height of the resist layer, there is a possibility that the side walls of the patterned areas of the resist will collapse in on each other due to capillary forces during the development step.[23] In this case, any subsequent evaporation step will fail because the metal will not be able to reach the surface of the substrate. If this occurs, a thinner resist layer should be used. This layer can be made by spin coating at a faster rate or diluting the polymer resist so the final thickness is less, and all dose tests will have to be redone for this new resist thickness. At this point, the substrate is now ready for downstream processes, such as metal evaporation.

3.1.1: Design of Lithography for EIT structures

The design of the EIT structures is based on previous literature.[15] For the first layer, an array of parallel rods are written. The parallel rods are designed to be 115 x 35 nm with a 30 nm gap between them. These parallel rods are patterned in an array with a five micrometer gap between each structure to ensure that they can be individually discriminated in the dark field set up at 60x magnification. This large distance between structures also conveniently means that proximity effects from the electron beam will not be a problem.

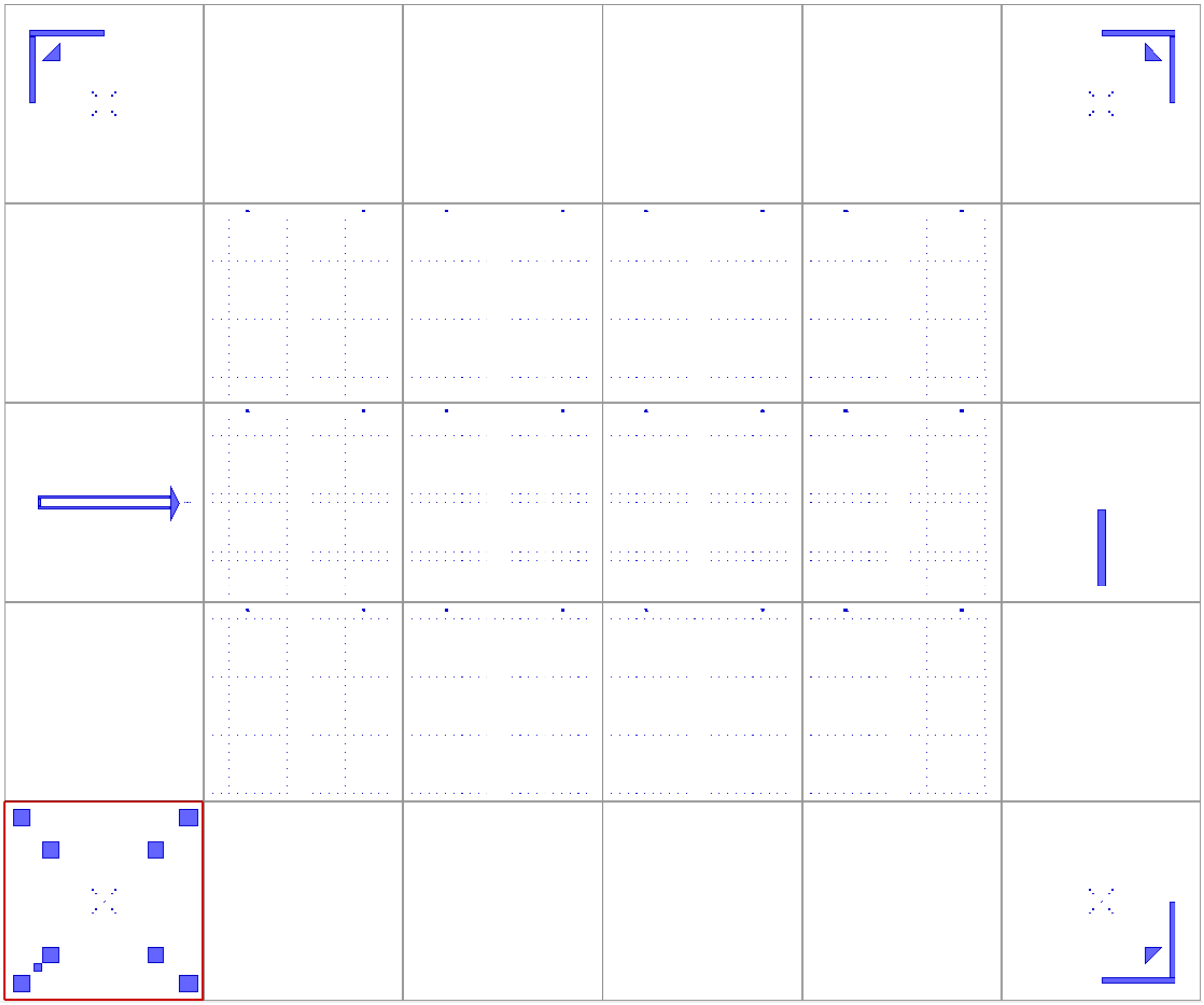

Figure 3.1: Screen shot of zoomed-out view of first layer e-beam exposure. The corners and edges have alignment markers. The center arrays are too zoomed out to see the continuous arrays, but the parallel rods are placed in a large array with a 5 µm pitch. The thick square looking dots are markers such as 1A, 1B, 2A, 2B, etc., to help identify individual assemblies.

The second layer has only the orthogonal opening for the orthogonal rod, which defines the rod shaped trench that the colloidally synthesized rod falls into, and binds to the parallel rods via DNA hybridization. Because there is inherent alignment error (± 10 nm in both the x and y directions on the CRESTEC machine assuming ideal writing conditions) we cannot be sure that the opening will be directly where it was programmed to be, the second layer openings are staggered along the length of the parallel rods, moving upwards from the bottom of the parallel rods to the top of the

parallel rods in 16 nm increments (Figure 5.10). The openings are programmed to be 50 x 140 nm to account for the hydrodynamic size of the rod functionalized with DNA.

3.2: Evaporation

Evaporation is a simple process—a liquid is heated until the intermolecular forces can no longer hold the atoms or molecules together, and the high energy moieties fly off. Evaporating a metal to conformally cover a substrate is useful for many applications, and techniques like evaporation or sputtering are commonly used to achieve this. However, evaporating metals like titanium, chromium, and gold takes place at very high temperatures, and require specialized equipment.

3.2.1: Introduction *to Evaporation*

There are two main types of evaporators, thermal and electron beam. In thermal evaporation, the metal to be evaporated is first placed in a tungsten boat. A voltage is placed across the boat, and the solid metal undergoes resistive heating until it melts and then evaporated. In an electron beam evaporation, the metal of interest in placed in a tungsten or coated carbon graphite crucible, and is irradiated by an electron beam until enough energy is transferred to the metal that it melts and then evaporates.[5] In this work, an electron beam based evaporator is used. It is also important to ensure that the vacuum of the chamber is as low as possible, as both the optical and material quality of the film is directly related to the vacuum of the chamber.[24,25]

In order to create structures of the same dimensions suggested by the Lumerical FDTD simulations, we have to accurately measure the thickness of the deposited film. To do this, a piezoelectric quartz crystal microbalance is used. This crystal microbalance has a natural resonance of vibration, and if any mass is added to it (such as evaporated metal), the frequency will shift. This microbalance is sensitive to masses of less than a nanogram, and is of great use for measuring deposition of thin films as a result.[26] Another important factor is the ‘tooling factor’. The tooling factor is a reflection of the geometry of the evaporator, and the fact that the sample and the quartz crystal microbalance cannot be mounted in exactly the same position (sometimes they are quite far apart), and therefore may be receiving a different rate of metal deposition. To account for this, a calibration run is conducted, and the actual thickness of the deposited film is measured by AFM or surface profiler and is compared to the thickness reported by the microbalance. The evaporator is calibrated with this new ‘tooling factor’, and will automatically adjust the output of the quartz crystal microbalance by this amount. The final major parameter is called the ‘z-ratio’, which describes the acoustic impedance ratio of a film deposited on a quartz crystal microbalance, and is element dependent. Put simply, correlating the frequency shift of the quartz crystal microbalance with the mass added is only a first-order approximation, and different evaporated metals will change the vibration of the microbalance by slightly different amounts, even if the added mass is the same. The z-ratio corrects for this material dependent change.[27]

Due to the high surface tension of gold, it does not bond easily to the glass substrate when it is evaporated at thin thicknesses (< 20 nm) and prefers to form islands instead.[28,29] To combat this, a thin (2-3 nm) adhesion layer of another metal, usually chromium or titanium, is evaporated first, followed by the desired amount of gold, which then deposits smoothly at much thinner thicknesses.[30]

There are two drawbacks of evaporated metals that make them of lower plasmonic quality than colloidally synthesized rods. First, chromium and titanium have much higher plasmonic losses than gold, so the presence of the adhesion layer could degrade the plasmonic properties of the lithographed rods.[31,32] Second, evaporated metals are usually polycrystalline at these length scales compared to colloidal rods, which are single crystals. The grain boundary can cause plasmonic losses as well.[33]

After evaporation, the metal film that is covering the resist needs to be lifted off. In order to do this, the substrate is submerged in a solvent that can dissolve the unexposed resist, such as acetone or n-methylpyrrolidone in the case of PMMA, and the metal layer can be rinsed off. Of particular importance in this step is the ratio of the heights of the resist and the evaporated metal film. If the evaporated film is too thick, the metal inside the lithographed trench will come in contact with the metal film on top of the resist, and lift-off will not work. A general rule of thumb is that the evaporated layer should not exceed half the height of the resist layer.

3.2.2: Experimental

A 2 nm titanium adhesion layer and 30 nm of gold were evaporated in an e-beam evaporator (Angled/Cooled Chuck Electron Beam Evaporator, Ultek). Lift-off was performed in warm (37 °C) acetone for 45 minutes to 1 hour followed by rinsing in IPA, and dried under nitrogen gas. A flow of the lithography and evaporation steps are shown below (Figure 3.2).

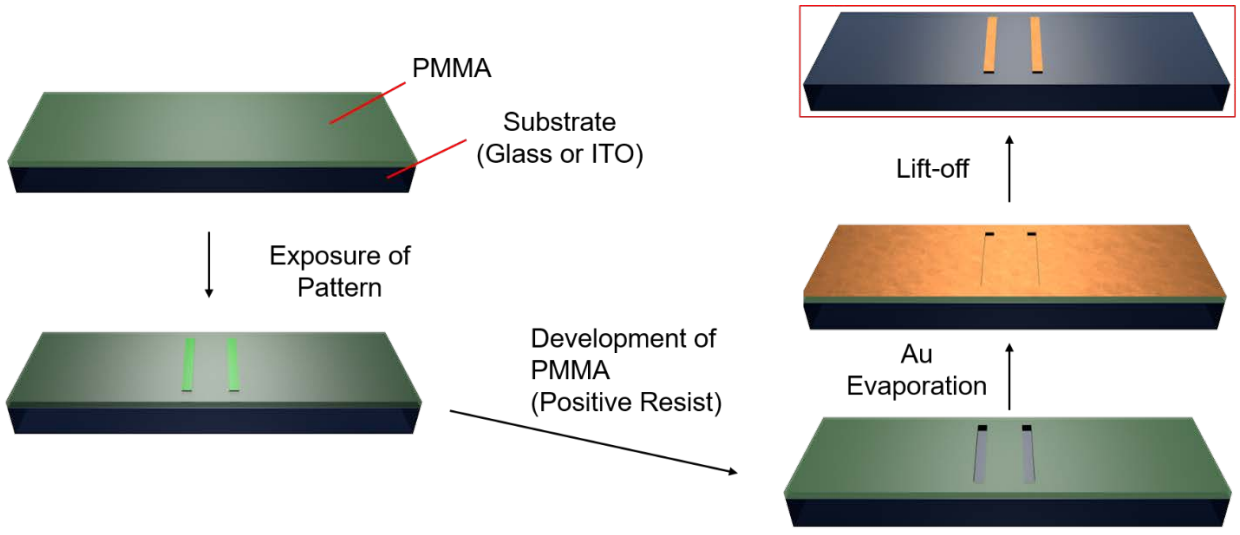

Figure 3.2: Electron beam lithography and evaporation steps that covers all the steps for chapter three up to this point. First, PMMA is spin coated on an ITO coated glass coverslip. Next, the parallel rods are exposed to the e-beam. The pattern is then developed in a 1:3 MIBK to IPA solution, and gold is evaporated into the trenches. The PMMA is dissolved, and the gold film is lifted off, leaving the parallel gold rods that are adhered to the ITO surface.

3.3: Scanning Electron Microscopy (SEM)

The principle of SEM is almost identical to that of electron beam lithography—many instruments used for electron beam lithography are in fact modified SEMs. A filament produces a beam of electrons, which are collimated and focused by electromagnets into a very tight beam only a couple nanometers or less. This beam rasters across the sample, scanning in a rectangular grid pattern.[5]

Many of the same sample requirements that apply to electron beam lithography also apply to SEM. For example, initial experiments were done a glass substrate, and acquiring decent images were very difficult due to the charging of electrons on the glass which caused deflection of the rastering beam. This problem was fixed when the slides were coated with ITO.

For this work, SEM is the only direct probe of the positions of the gold nanorods in the fabricated structures. While dark field spectroscopy gives a spectrum of a single assembly, there are several arrangements of the nanoparticles that could give similar shapes. However, SEM only can take images in high vacuum, causing the DNA holding the structures together to collape, so the orthogonal rod would be closer to the parallel rods compared to their hydrated state. When possible, SEM is used to look at the structure either before or after the dark field to validate if the spectra corresponds to the programmed structure or is due to an off-target configuration.

3.3.1: Validation of Electron Beam Lithography.

SEM is the major tool used to validate the steps in the electron beam lithography process. It is first used to examine the many dose tests to determine which of the programmed values and doses yields the parallel rods of the desired dimensions. Once the dose tests are complete and parallel rods can be repeatedly written with high fidelity, SEM was used to validate that the second layer lithography worked. To do this, a second layer exposure was written as planned, and trenches were opened above the middle and tips of various parallel rods. Instead of functionalizing the parallel rods with DNA, a second evaporation was done to evaporate the orthogonal bar. Only after this step was validated did the work progress to DNA, because if we tried to assemble the EIT structures and did not see them assemble, we would not know if there was a problem with the DNA, or if there was a problem that the experimenter simply did not have master over multi-layer alignment (Figure 3.3).

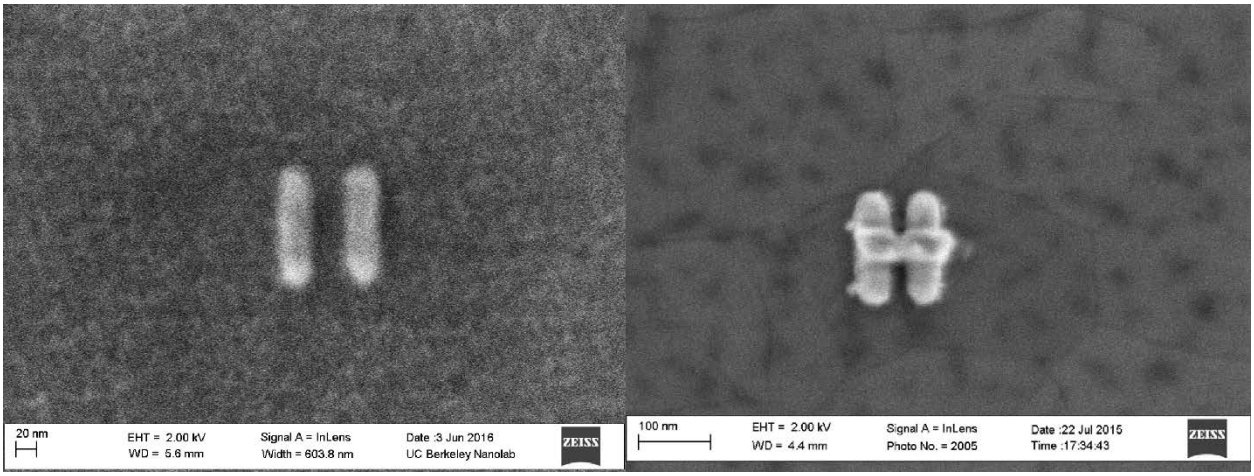

Figure 3.3: SEM validation of lithography steps. Left: parallel rods written with e-beam lithography, demonstrating that the e-beam lithography tool can nicely fabricate two parallel rods with the desired dimension and spacing. Right: An evaporated gold rod orthogonal to the lithographed parallel rods. The distortion in the middle of the rod is where the metal was evaporated into the gap between the parallel rods, giving a sagging appearance. This demonstrates that the second layer alignment step works well and a trench can be opened over the middle of the parallel rods and bridge the gap.

3.3.2 Sample Preparation for SEM

The following procedures are followed to prepare the slides for SEM (assuming Dark Field spectra have already been taken or will not be taken for the slide, see Chapters 5, 6, and Appendices 3 and 4). The slide is first washed in 0.3 M ammonium acetate to remove any NaCl that could crystalize and make imaging difficult. The slide is then put in a vacuum desiccator, as ammonium acetate salt sublimes at low pressure and will not leave a salty residue.[34] The PMMA is removed by submerging the slide in acetone for several minutes followed by a quick rinse in isopropanol, and dried under a stream of nitrogen gas. The presence of acetone and isopropanol do not cause the DNA to dehybridize, merely it dehydrates the DNA, collapsing it and brings the dipole rods closer to the quadrupole wires. SEM images were taken on either a Zeiss Ultra 60-SEM or a FEI Nova NanoSEM 650 SEM, using a 2 keV acceleration voltage.

This chapter has given an overview of the lithographic techniques necessary to create low symmetry structures. Furthermore, the experimental results in this chapter show that it is possible to fabricate and characterize the structures desired in the FDTD simulations given in Chapter 2. The next chapter will deal with colloidal synthesis of plasmonic gold nanoparticles.

Chapter 4 : Colloidal Nanoparticle Synthesis

Colloidal nanoparticle synthesis is a maturing field in the community. While growth mechanisms of nanoparticles are not as well understood as the mechanisms of organic synthesis, chemists still have a decent handle on why and how we can synthesize our current library of shapes.

For this project, the orthogonal gold rod used for creating the plasmonic EIT analogue had to be made colloidally if we want to make it the 'dynamic' part of the structure. Colloidal nanoparticles are easily functionalized with DNA (see Chapter 5), and can therefore be the mobile component of the assembly. This chapter will briefly discuss only two of the many gold nanoparticle shapes (spheres and rods) available to synthetic chemists.[35–37] Colloidal synthesis has several advantages over electron beam lithography in that it is a batch process and all the particles grow in parallel (as opposed to a serial process), a huge number of particles can be created at once, and colloidal particles are usually single crystalline.[37,38] However, colloidal synthesis cannot achieve some of the low symmetry shapes that can be made with e-beam lithography, and these synthesized nanoparticles cannot be easily arranged in arbitrary patterns on a substrate.

4.1 Gold Spheres

The simplest gold nanoparticle shape to grow is that of a sphere. I use the term 'sphere' rather broadly, as high resolution TEM images of very small gold and silver 'spheres' sometimes do show that they are actually faceted, and some seeds are actually cuboctahedra.[38] Overall, most spherical particles are single crystalline, which means that there will be fewer defects that will cause losses in their plasmonic modes.

One common method for making large spheres (twelve to one hundred fifty nanometers in diameter) is to use the method developed by Turkevich and improved by Frens, which requires the Au(III) chloride solution to be reduced to Au(0) at elevated temperature by citrate.[39,40] The citrate then works as a capping agent to stabilize the gold nanoparticles via electrostatic repulsion.

Gold spheres are thought to follow the LaMer growth mechanism (Figure 4.1).[41–44] This mechanism consists of two phases, a nucleation phase and a growth phase. The nucleation phase occurs upon injection of the reductant into the precursor solution. As long as the precursor concentration is greater than some critical threshold, small nanoparticles spontaneously nucleate. Once enough nanoparticles have nucleated, the precursor concentration drops below this critical threshold, and new nuclei no longer form (at this point there can be quite a variation in nanoparticle size, depending on how long the nucleation phase lasted). Instead, precursors bind to already formed nuclei, and they grow in size, hence this phase is called the growth phase. The growth regime also allows for 'size focusing'. Early on in the growth phase, the smaller nanoparticles grow more quickly than then larger nanoparticles.[45–47] Thus the average heterogeneity decreases. As the precursor concentration further decreases, a process called Ostwald ripening occurs. Due to different surface energies between the smaller and larger nanoparticles (depending on when they nucleated), the larger nanoparticles are more stable than the smaller ones. As a result, the smaller nanoparticles actually dissolve and reform on the larger nanoparticles. This process decreases the number of nanoparticles in solution while simultaneously increasing the average particle size. As the smaller particles are dissolving and the larger ones are growing, the size distribution increases, and this phase can be referred to as 'defocusing'. Eventually, the monodispersity of the solution

increases over time through this process as the smaller particles completely dissolve. At some certain size, the difference in surface energies becomes more or less negligible, and Ostwald ripening no longer plays a role in nanoparticle morphology.

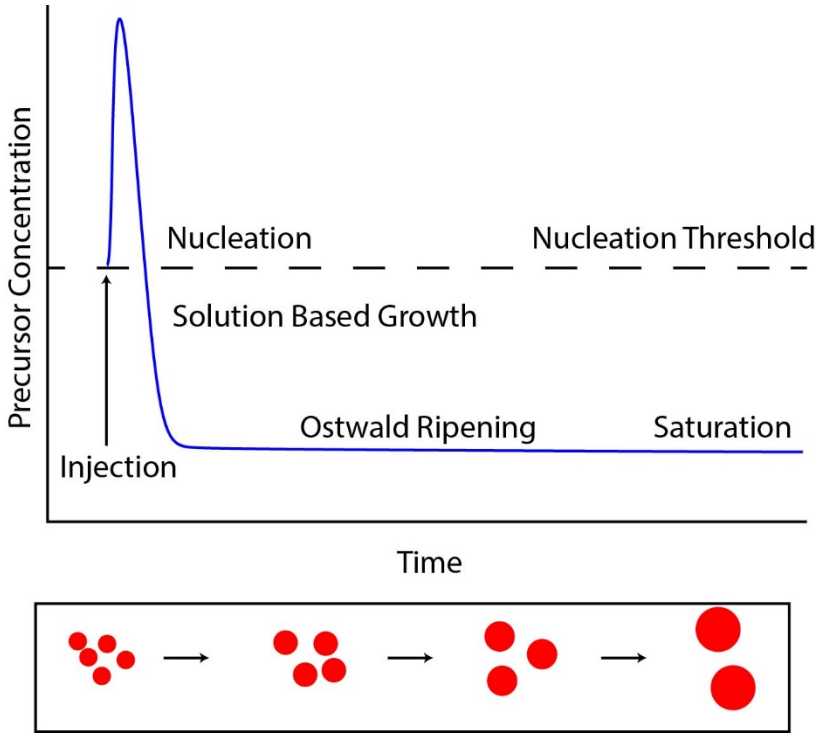

Figure 4.1: Scheme of LaMer growth model.

4.2 Gold Rods

For this work, a colloidal gold nanorod is needed to couple into the quadrupolar mode of the lithographed parallel rods. While gold nanorods can be synthesized, the community is still debating the minutiae of the mechanisms that cause symmetry breaking in gold nanoparticles.

4.2.1 Murphy Method

A seed based synthesis of colloidal gold nanorods was first reported from the Catherine Murphy group.[48,49] To create gold nanorods, they first created small gold nanospheres to use as seeds through a fast reduction of gold (III) chloride with sodium borohydride and used tri-sodium citrate as a capping agent (the citrate will not reduce the gold salt at room temperature). They then place these seeds in a growth solution of cetyltrimethylammonium bromide (CTAB), gold (III) chloride ($HAuCl_4$), and ascorbic acid (AA). They controlled the aspect ratio of the rods based on the ratio of seeds to growth solution. The fewer seeds added, the longer the rods became as more growth took place on each rod before the precursors were depleted.

4.2.2 El-Sayed Method

Perhaps the most common synthesis for anisotropic gold nanoparticles is the gold nanorod preparation created by the El-Sayed group.[50] They improved on the Murphy synthesis by demonstrating that it is possible to control the aspect ratio by changing the amount of silver in the growth solution. The more silver, the longer the rods became, increasing the aspect ratio of the

rods until they reached an aspect ratio of 4 or 5. After this point, additional silver ions did not affect the aspect ratio. The largest, high quality nanorods that this paper created were about 50 by 12 nm, which is slightly too small for metamaterial targeted in this work—to have the resonances of the lithographed parallel rods match the resonances of a rod this size, the limits of the lithography tool would have to be pushed to their limit. Therefore, larger rods are needed. (While the El-Sayed paper describes a slightly different preparation using a binary surfactant mixture, CTAB and benzyldimethylhexadecylammonium chloride (BDAC) to make larger nanorods, they are too polydisperse for the work in this thesis.)

4.2.3 Ye Method (Murray Group)

When Xingchen Ye was a graduate student in Chris Murray's lab at UPENN, he developed a synthesis that could create larger, monodisperse rods in excellent yield.[51] He did this by adding a second surfactant, sodium oleate (NaOL), to the growth solution in addition to CTAB (this approach is similar to the El-Sayed method of CTAB and BDAC, but has other components that make the overall quality higher). He theorized that the double bond in the sodium oleate acted as a mild reducing agent to turn Au(III) into Au(I), and the ascorbic acid (AA) is then used to reduce the Au(I) to Au(0). They believe that this improves upon previous methods, because while using AA to reduce Au(III) to Au(I) works to make the rods, the oxidation product of AA still has reducing power. This oxidized organic molecule still has the potential to reduce Au(I) to Au(0) prematurely, which could start some nucleation and create a more polydisperse sample. NaOL reduces the amount of AA necessary in the prep, and the quality of rods increases. NaOL is also a basic molecule, so they adjusted the pH of their growth mixture to be acidic with hydrochloric acid, as rod growth is best at low pH. Using this synthetic approach, it was possible to attempt to make rods that were 100 nm long with a 30 nm diameter. The closest batch of rods achieved were 96 x 30 nm, and those conditions are given in Appendix 3, although conditions may vary slightly for synthesis to synthesis.

4.2.4 Symmetry Breaking

One of the biggest points of contention in the literature of anisotropic growth is the exact mechanism of symmetry breaking. That is, what is the role of CTAB and silver nitrate that causes rods to form, instead of larger spheres? It has been postulated that the CTAB micelle (or the bromide ion in particular) helps template the formation of the rod by binding slightly more strongly to the {110} facet than others, biasing the growth in one direction.[50] Other groups that conducted TEM studies on the symmetry breaking step suggest that the silver ion plays a stronger role in binding to defects that form on the seed surface during growth. Specifically, they believe it is the silver that binds strongly in the <110> direction and is responsible for breaking symmetry.[38]

4.3: Experimental

Rods were synthesized according to previous protocols using the Ye method (see Appendix 3).[51] The rods and their UVvis spectrum used for this work are shown below (Figure 4.2).

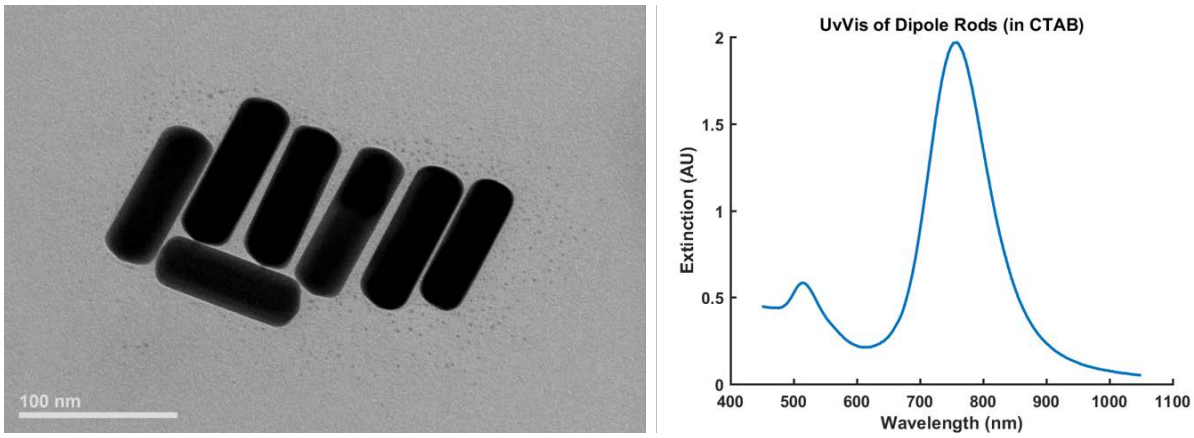

Figure 4.2: TEM of 96x 30 gold nanorods and their UVvis spectrum. The transverse peak can be clearly seen at 515 nm, whereas the longitudinal peak is at 759 nm.

In Chapter 4, we have synthesized the orthogonal rod for the assembly and have understood the mechanism behind its growth. The next chapter will deal with the functionalization of this orthogonal rod and the DNA mediated assembly process.

Chapter 5 : DNA mediated self-assembly

5.1: Introduction

Deoxyribonucleic acid (DNA) is perhaps the most famous polymer in the world. It is commonly called the 'blueprint' of life and is found in every living organism. The specific sequence of the four nucleic acids, adenine (A), thymine (T), guanine (G), and cytosine (C), regulates genes, dictates the amino acid sequences that are incorporated into proteins, and controls a vast number of other cellular functions. To understand how I used DNA (which is usually thought of as controlling the biology of organisms) as a scaffolding material for nanoparticles, I will first discuss the basics of how DNA behaves, then the history of DNA in the nanotechnology field, and finally explain how I used DNA for my work.

5.1.1 Basics of DNA Structure

DNA behaves in a predictable manner—scientists can program its behavior from first principles simply by defining its structure—the sequences of A, T, G, and Cs. One of the most important discovery of DNA is 'Chargaff's Rules', which found that across all species, the amount of purines (A and G) and pyrimidines (T and C) are equal in any organism.[52] This was explained by the work of Rosalind Franklin, Francis Crick, and James D. Watson, who figured out that DNA was a double helix composed of two anti-parallel strands, with adenine pairing with thymine via two hydrogen bonds (A=T) and guanine pairing with cytosine with three hydrogen bonds (G≡C).[53,54] The nucleobase is bonded to a ribose sugar (this unit is known as a nucleoside), and when the nucleoside is bound to a negatively charged phosphate, the entire unit is referred to as a nucleotide. When the nucleotides are polymerized into a chain, the ribose sugars and phosphates will alternate along the backbone of the polymer. Each ribose will have a phosphate on the 5' and 3' carbon, and this connectivity defines the convention for direction along the DNA strand. DNA strands are 'read' in the 5'→3' direction, and are synthesized this way in biological systems (as an aside, DNA is artificially synthesized in the 3'→5' due to chemical constraints).[55] Two strands are considered complementary if, when one strand is laid in the 5'→3' direction and another strand is laid next to it in the 3'→5' direction, all the As are paired with Ts and Gs are paired with Cs. If this is the case, the two strands will form a double helix. This helix has a diameter of 2 nm. Depending on the salt conditions of the DNA strand, the helix can take different conformations. In the common B-form of DNA, a single turn of the helix occurs every 10.5 base pairs, and is 3.4 nm in height. The distance between subsequent bases is about 0.34 nm. In the A form, the helix is slightly more compressed, and the distance between bases is about 0.255 nm.[55,56]

5.1.2 Basics of DNA Behavior

Now we know how DNA forms through base pairing, and which bases interact. Because DNA is held together by relatively weak hydrogen bonding between bases in anti-parallel strands and pi-stacking interactions between adjacent bases in the same strand, we expect that this interaction is reversible.[57] By simply raising the temperature, one can cause the DNA to 'melt', or fall apart into single strands.[55,58] The melting temperature (T_m) is defined as the temperature at which half the strands are in their single stranded state (ssDNA) instead of the double stranded state (dsDNA). The longer the DNA strand is, and the higher the GC content of the strand, the higher the melting temperature.

Because the DNA backbone has many negatively charged phosphate groups, one might correctly expect the strands to electrostatically repel each other. The strength of this repulsion can be modulated by the amount of salt present in solution; the more positively charged cations are present, the more the electrostatic repulsion is screened and the higher the melting temperature is. If the salt concentration is lowered, the DNA strands repel each other more strongly, and the lower the T_m becomes. Therefore, salt is the third handle on T_m in addition to DNA length and GC content (Figure 5.1).

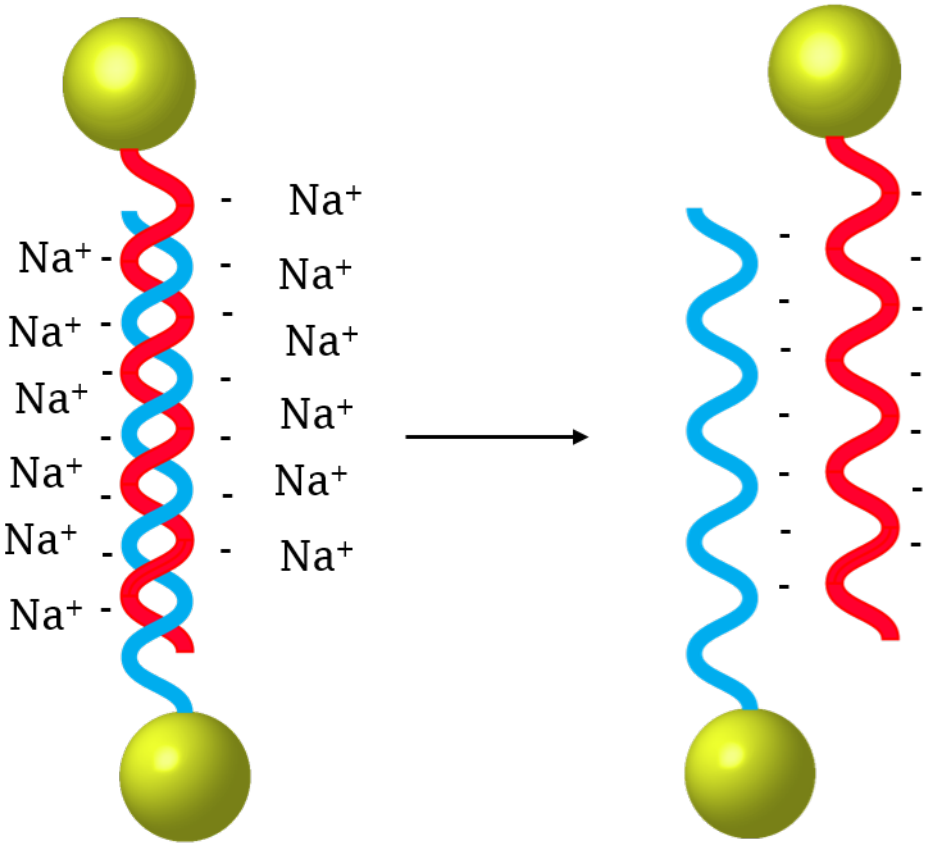

Figure 5.1: Salt mediated melting of DNA strands attached to gold spheres. The sodium cations screen the negatively charged phosphate backbones of the DNA, allowing two strands to hybridize. At low salt concentration, the T_m will decrease, and the electrostatic repulsion can overcome the hydrogen bonds and base stacking holding the DNA together.

5.2: History of DNA Mediated Self-Assembly

Nadrian ("Ned") Seeman is credited as the father of DNA nanotechnology for his seminal paper and work on using DNA as a structural, scaffolding material (with the hope of using it to help crystalize difficult-to-crystalize proteins).[59] He was able to create complex tiling patterns using DNA that self-assembled into extended and crystallizable motifs.[60] (As an aside, several of his students, including Chengde Mao, now use his DNA tiling techniques with nanoparticles.[61,62])

DNA was first used as a scaffold to direct assembly of nanoparticles in 1996, in papers published simultaneously by the Alivisatos and Mirkin groups, and the field has since exploded.[63–65] The approach taken by the Alivisatos group was to place a single DNA on a gold nanoparticle using a thiol linking group (Figure 5.2). This allowed the researchers to make structures with discreet

numbers of nanoparticles, such as dimers, trimers, tetramers and hexamers.[63,66] Later work explored making interesting shapes, such pyramids with differently sized nanoparticles at each vertex, which showed chiral optical properties, and has been explored by the Kotov group.[67,68] Other work out of the Alivisatos group focused on developing 'plasmon rulers', or gold nanoparticle assemblies (usually dimers) that changed their plasmon resonance when a protein would interact with the DNA scaffold and change the distance between the gold nanoparticles.[69–72] Based on the plasmonic shift, it was possible to back out how some of these proteins interacted with the DNA.

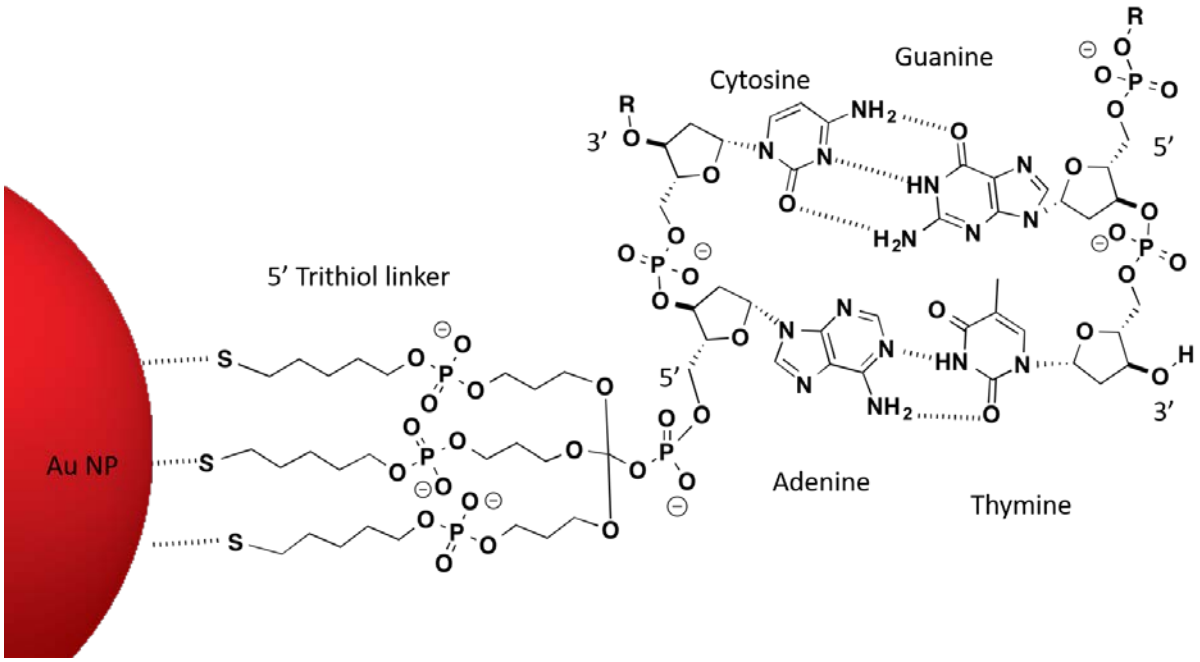

Figure 5.2: Schematic of thiolated DNA connected to a nanoparticle. On the right side, a G≡C and A=T pair are shown connecting via hydrogen bonds. The 5' and 3' ends are shown, and in this case, a 5' thiol linker is added to the terminal 5' ribose, and is connected to a nanoparticle. Note that the phosphate backbone is negatively charged.

The Mirkin group, on the other hand, covered their nanoparticles with hundreds to thousands of DNAs. These dsDNAs have a four or five base pair 'sticky end' that is complementary to DNA on another nanoparticle. These nanoparticles, when assembled, form large aggregates or superlattices. At room temperature, any single DNA interaction is too weak to be stable, but the many DNA interactions between two nanoparticles are stable. Through this weak but multivalent interaction, they are able to create superlattices with very sharp melting temperatures. By raising the superlattices to above the T_m and slowly cooling to below the T_m, the Mirkin group is able to anneal their assemblies to form a variety of crystal structures.[73–76] Recent work has been focused on assembling more anisotropic nanoparticles and making their superlattices dynamic and reconfigurable.[77–79]

In 2006, Paul Rothemund at Caltech had a brilliant idea to use a single stranded viral DNA and shape it using short, carefully chosen 'staple strands' of complementary DNA to force the DNA into a plethora of arbitrary assemblies.[80] This field is known as DNA origami, and its simplicity combined with its power to access almost any imaginable shape has convinced me that it is likely

the future of DNA based assembly for the majority of applications. This work was extended by many groups, and quickly three dimensional, curved, and dynamic assemblies were being constructed as well as small machines.[81,82] Soon, DNA functionalized nanoparticles were being used to decorate the DNA origami structures. The Liedl and Liu groups have taken a lead in using DNA origami to place plasmonic particles in optically interesting arrangements. Their work covers a variety of chiral assemblies, some of which even switch handedness upon a DNA strand displacement reaction.[83–88] Shawn Douglas, now at UCSF, created a free program called cadnano that can be used to design DNA origami structures of almost any shape and will automatically output the staple strands (Figure 5.3).[89]

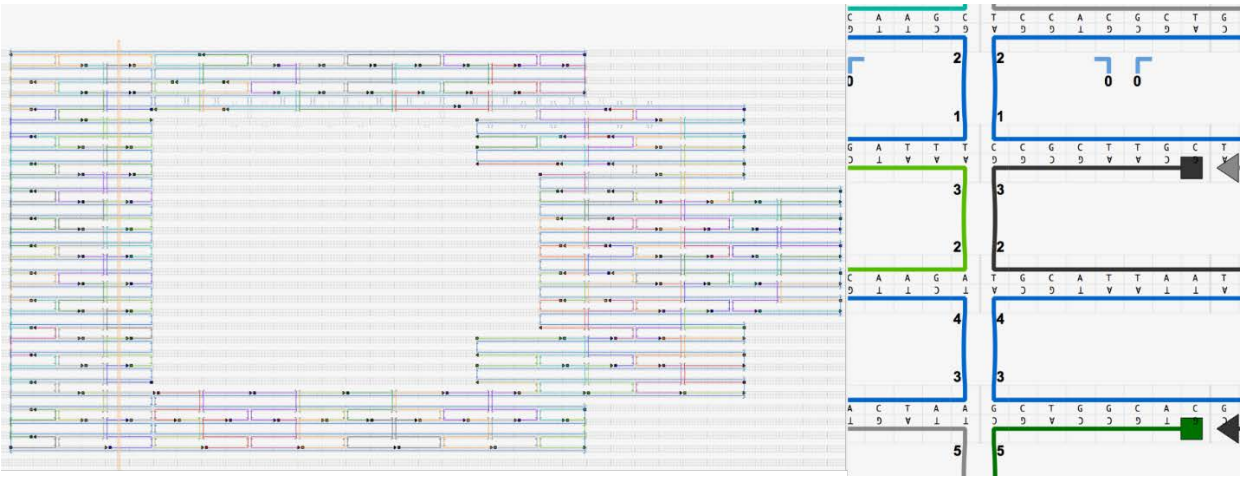

Figure 5.3: DNA origami of the letter 'D' rendered in cadnano. The left side is a zoomed out picture of the whole letter. Each staple strand is a different color. On the right is a zoom in of a small portion of the D. The blue line is the viral DNA, and the different colors are the staple strands. The squares and arrowheads are the 5' and 3' end of the staples, respectively. Once can see that each A is paired with a T, and each G with a C.

5.3: Assembling a Dynamic Metamaterial that Exhibits EIT

As mentioned in Chapters 2 and 3, most metamaterials are made via lithography, and are therefore static. Some groups have taken advantage of various substrates that the metamaterials are lithographed on to impart some form of dynamics. For example, the Atwater group at Caltech lithographed split ring resonators (SSRs) on a polydimethylsiloxane (PDMS) substrate. When they stretched the PDMS, the components of the SSRs would move in relation to each other and the resonances would shift based on the amount the PDMS was stretched.[90] The Kim group at Seoul National University used photolithography to pattern a metasurface on a vanadium dioxide (VO_2). The distance of the gaps between the metasurface components tuned the insulator-to-metal transition of the surface.[91] However, these metamaterial 'dynamics' rely on the dynamic nature of the substrate, and not on the metamaterial components themselves—the property and the substrate are inexorably linked. Furthermore, the perturbations are on a global scale and aren't local changes. It would be a step forward to make a metamaterial that itself is dynamic. If the plasmonic EIT analogue can be made with DNA, then metamaterials that are truly dynamic and can react to both global and local chemical stimuli can be fabricated.

If the orthogonal rod of the structure was assembled with DNA, one would be able to adjust how close it is to the parallel rods, and hence be able to tune the coupling.

5.3.1: Historic Motivation

In addition to the motivation of creating dynamic metamaterials, there is hope that architectures that display EIT can be used as plasmon rulers. Traditional plasmon rulers (see section 5.2) are made by two spheres connected by DNA. However, because these dimers used spherical nanoparticles, the change in plasmon resonance was usually quite small upon a binding event.[69,72] In 2011, Na Liu, then a post-doc in the Alivisatos group, theorized that a low symmetry arrangement of five nanorods that exhibited EIT would be an excellent target structure for a ruler.[18] Theoretical modeling by Na Liu and experimental work by Mario Hentschel (then in the Giessen group, and later a post-doctoral scholar in the Alivisatos group) showed that lithographed assemblies of these type showed non-linear responses to even nanometer changes in the relative positions and angular directions of the rods. Mario suggested I pursue this project using this motivation.

5.3.2 Early Problems

Creating, isolating, and assembling gold nanorods with single DNA strands has proven very difficult, though ensembles of dimers have been made in our group.[92] The Kotov group has also reported limited success in making nanorod dimers, though there was often more than one DNA per nanorod, and trimers and higher order assemblies were formed.[93] To make nanorods assemble into a structure that exhibits EIT, one would have to be able to selectively functionalize a single DNA at the tips or side of nanorod and isolate it in high yield, which has not yet proven practical. First, if thiolated DNA is added to a batch of rods in a 1:1 ratio, it will result in a mixture of rods that have zero, one, two, or three conjugated DNAs following a Poisson distribution. At most the researcher can hope for a 36.7% yield of rods with a single DNA. Second, there is very little driving force that would cause the DNA molecule to selectively bind to the tip versus the side of the nanorod. Third, techniques to separate this Poisson distribution of functionalized rods, such as gel electrophoresis and high pressure liquid chromatography (HPLC) have high intrinsic losses.

To separate rods with different numbers of DNAs from each other using gel electrophoresis, the electrophoretic mobility of the conjugate rods should dramatically change with each added DNA. This includes significant changes to the mass and charge of the overall nanoparticle. Because rods are so massive, and are usually already stabilized in solution by charged ligands, the DNA would have be very long to change the electrophoretic mobility enough to give discretely separated bands. The longer the DNA is, the weaker the plasmonic coupling would be in an assembly, and the weaker the plasmonic effect. While the Alivsiatos group had slightly better results when using an HPLC to separate rods with DNA than gel electrophoresis, yield was still quite low, and the separation suffered due to the same reasoning.[94] It does not bode well for the success of a project when the desired parameters for the separation technique and the desired plasmonic properties are in contention with each other.

Due to these practical problems, we decided not to create the assembly completely using colloidal rods. In collaboration with my mentor, Mario Hentschel, I decided to use a simple system of three rods, and place two of them on a substrate using electron beam lithography (see Chapter 3), and have only one colloidally synthesized rod that was functionalized with hundreds of DNAs bridge the gap between the parallel rods. The major drawback of having numerous DNA connections is

that the usefulness of a plasmon ruler is limited, as a single protein or small molecule interacting with a single DNA will likely not perturb the structure as strongly as if there were a single DNA connection. As a result, the project is framed in terms of creating dynamic metamaterials, and not a next generation plasmon ruler.

5.4: Experimental Results

The DNA strands used in this work are based on work done in the Mirkin lab.[95] DNA A Anchor and DNA B Anchor are 28-mer sequences with a thiol group on their 3' end to anchor them to a gold surface (either the orthogonal rod or parallel rods, respectively). They have a flexible spacer region of 10 adenines on their 3' end, followed by an 18 base pair region that will bind to either Linker A or Linker B, respectively. Linker A and Linker B are 24 bases long, and 18 bases will hybridize with Anchor A or Anchor B respectively on the 5' end, and the 5 terminal bases on the 3' end are sticky ends and will hybridize with each other (there is one flexer adenine base on the linker DNA that does not participate in pairing, this is on the 19th base from the 5' end). The Random Anchor and Random Linker were used as negative control DNA to ensure that assembly was in fact DNA dependent (Table 3 and Figure 5.4).

Table 3: DNA bases used

A Anchor	5′-TCAACTATTCCTACCTACAAAAAAAAAA-SH-3′
A Linker	5′-GTAGGTAGGAATAGTTGAATCTCT-3′
B Linker	5′-TTGCTGAGTATGAGTGGAAAGAGA-3′
B Anchor	5′-TCCACTCATACTCAGCAAAAAAAAAAAA-SH-3′
Random Anchor	5′-AAGTCTACACAATCTAGTAAAAAAAAAA-SH-3′
Random Linker	5′ ACTAGATTGTGTAGACTTATTAGA-3′

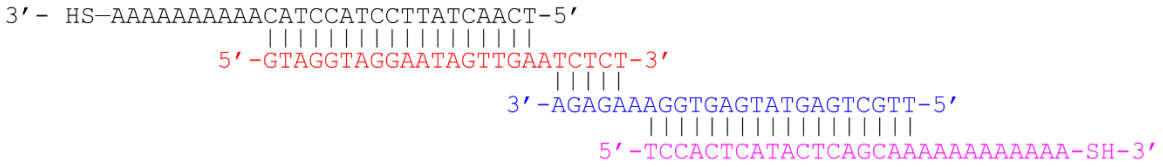

Figure 5.4: Schematic of DNA hybridization between the A and B DNA, the vertical line indicates the base pairing of complementary strands. The 3' thiols will bind to a gold surface, either on the parallel rods or the orthogonal rods.

The total surface-to-surface distance is predicted to be around 15 nm, which is shorter than one expects with a 0.34 nm rise per DNA base in B-form DNA. The Mirkin group found a 0.255 nm rise per base to be more accurate for this DNA design, and discuss in it detail in their papers.[74] Briefly, the high salt concentration of the buffer used in functionalizing the nanorods may be causing the DNA to adopt the A-form conformation, and the single stranded polyadenine tail on the anchor strands may be sitting on the gold surface, bringing the nanoparticles closer together. The experimental for adding DNA to rods is discussed in Appendix 4.

5.4.1 Using DNA to attach Rods to surfaces:

DNA coated rods binding to a gold surface functionalized with complementary DNA follows the Langmuir adsorption model (Equation 4).[95] In this model, there are several assumptions made about the interaction between the substrate and the binding moieties. First, all the binding sites are

independent and binding at one site does not affect binding at another site. Second, all sites have an equal probability of adsorption. Third, adsorption will occur in a monolayer. Fourth, the binding moieties do not-interact with each other. Finally, binding is an equilibrium process (that is, it is reversible).

The isotherm can be put in the form:

$$\theta = \frac{[Adsorbate]}{[Adsorbate]+K_d} \tag{4}$$

Where θ is the fraction of occupied sites, [Adsorbate] is the concentration of rods, and K_d is the dissociation constant, or the equilibrium constant for the release of the rod from the surface (and has units of concentration).[55] In our case, all the assumptions are met except possibly the first one (two rods could bind in such a way as to make an area of the gold surface inaccessible to further rod binding). Other work by the Mirkin group used lithographed gold landing pads instead of a bulk surface to account for this—each binding site can bind exactly one nanoparticle.[95] Therefore, I will treat the binding of the rods to the surface as if they follow a Langmuir isotherm.

It was determined that a 10 nM solution of rods was necessary to attach rods to a gold surface. Physically, this means that the K_d is slightly under 10 nM— if we have less than 10 nM of rods in solution, it will be more thermodynamically favorable for them not to bind to the surface. If we have more than 10 nM rods, it will be thermodynamically favorable for them to bind to the gold surface. In these control studies, glass coverslips had thin layers of gold evaporated on both sides. They were functionalized with DNA B Anchor and DNA Linker B as described in Appendix 5. They were then submerged into different concentrations of rods functionalized with DNA A Anchor and DNA Linker A for four hours (see Appendix 5). It was found that the solution needed to be 10 nM for full coverage of rods on the surface (Figure 5.5 and Figure 5.6). As a result of these experiments, all assemblies of the structures plasmonic EIT analogues were done in 10 nM rod solution.

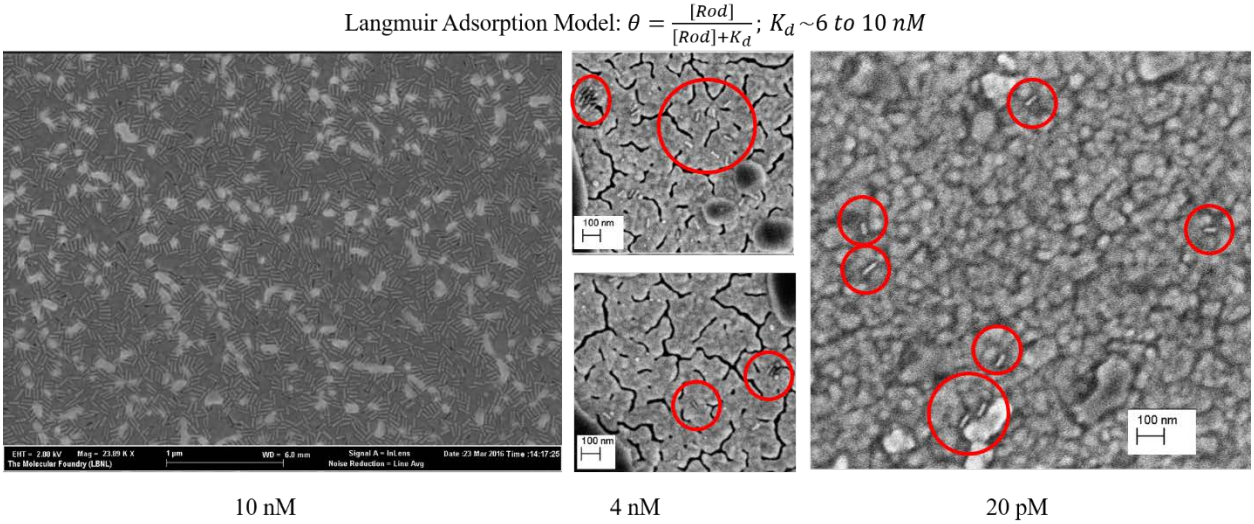

Figure 5.5: Langmuir isotherm test of binding. It was determined that the concentration of rods needed to bind on the surface was around 10 nM. Lesser concentrations, such as 4 nM and 20 pM do not favor binding to the surface.

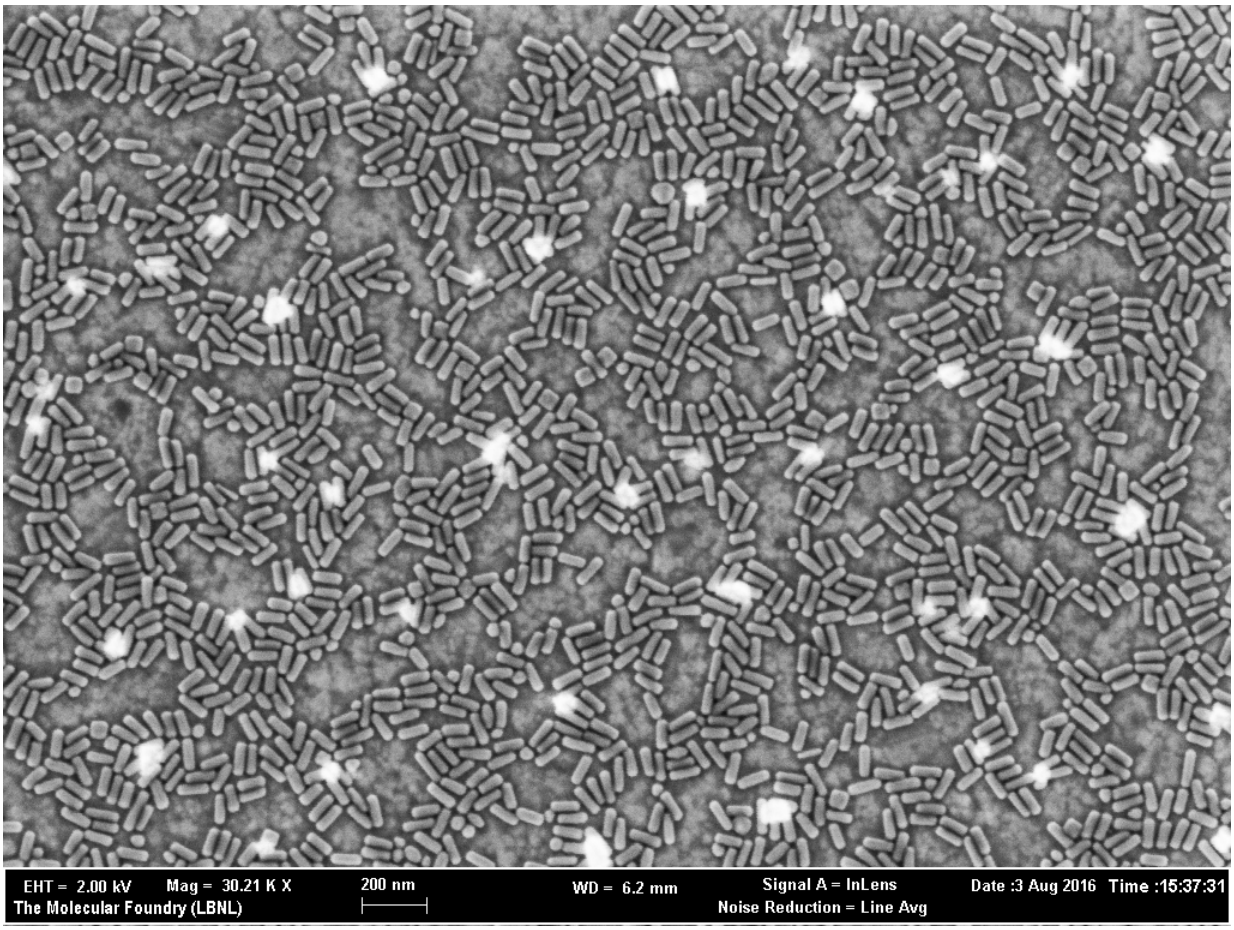

Figure 5.6: Positive control of DNA mediated binding to a gold surface. SEM of 10 nM rods with A DNA on gold substrate with B DNA. The bright white specks are salt crystals.

A negative control with rods with 'Random DNA,' or DNA that is not complementary to B Anchor and B Linker (see Table 3) did not show significant binding to the gold surface, even at 20 nM concentration of rod (Figure 5.7). We can therefore be confident that assembly of the orthogonal rod to the parallel rods is indeed DNA mediated.

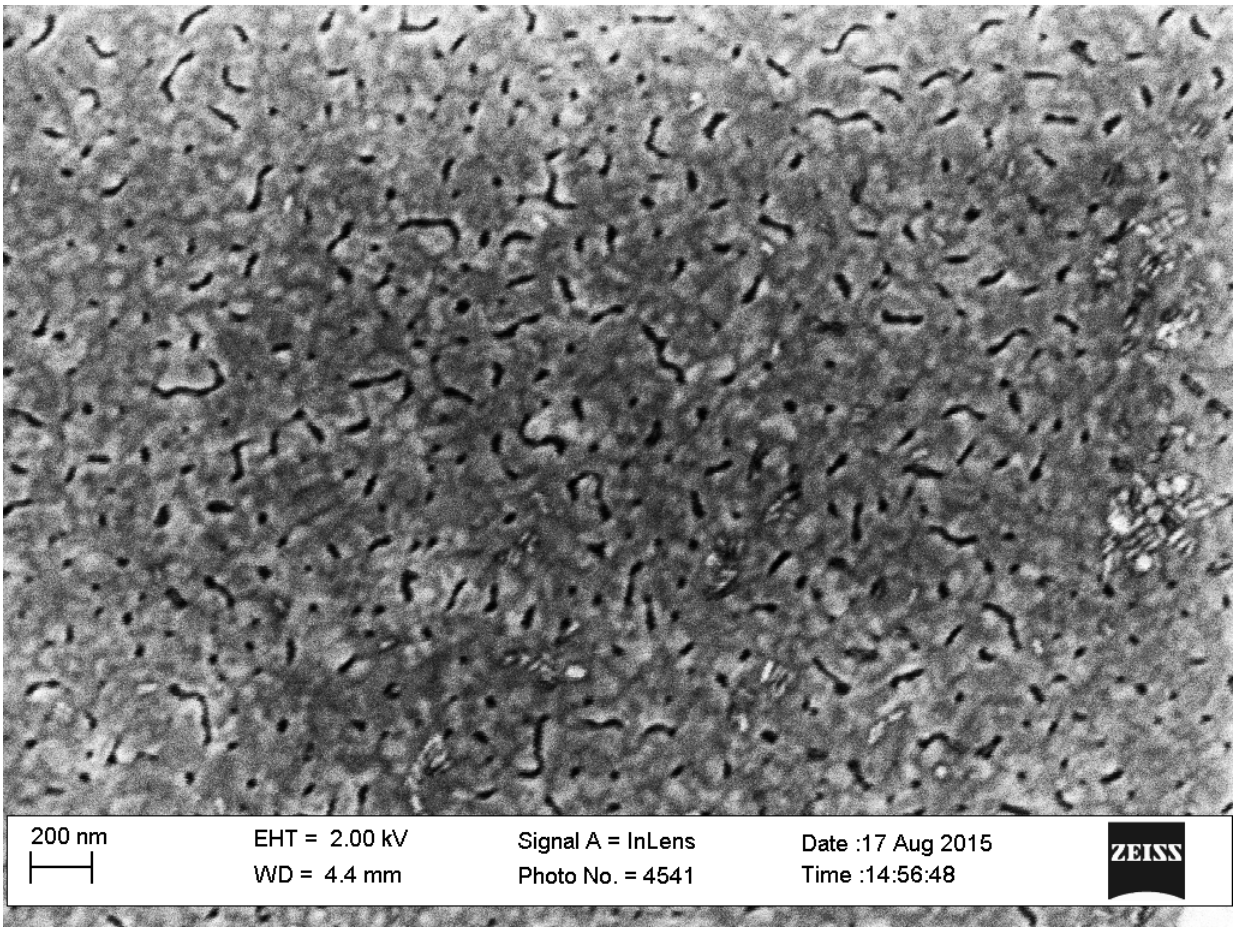

Figure 5.7: Negative control of DNA binding to a gold surface. Control using 20 nM rods functionalized with non-complementary 'Random' DNA on a gold surface with B. DNA. The black pockmarks are due to a less than perfect evaporated gold layer. Some rods (white specks) can be seen, but binding is much less than 10 nM rods with complementary DNA. (The rods used in this experiment were 48x12 nm, instead of 96x30. Not shown are the positive control with 48 x 12 nm rods because the 96x30 data is more relevant, see Figure 5.6)

5.4.2 Quantification of Results

Now that we have shown that DNA functionalized rods will bind to a gold surface that is functionalized with complementary DNA through DNA interactions, we can attempt to create our dynamic metamaterial (Figure 5.8). Using lithography, we have already written our parallel rods and opened a trench over either the tips or the middle of the parallel rods using multi-layer exposures. *The next critical step is to expose the substrate with PMMA to a 30 second O_2 plasma etch on low to remove residual PMMA that is not removed during the development stage using 1:3 MIBK to IPA.* Even with MIBK development, there is about a 1 nm residual layer of PMMA, and the DNA will not be able to bind to the gold surface. The O_2 plasma etch ensures that the gold will be exposed. We can now add thiolated DNA to the surface (See Appendix 5), and add the orthogonal rod with complementary DNA (Figure 5.8).

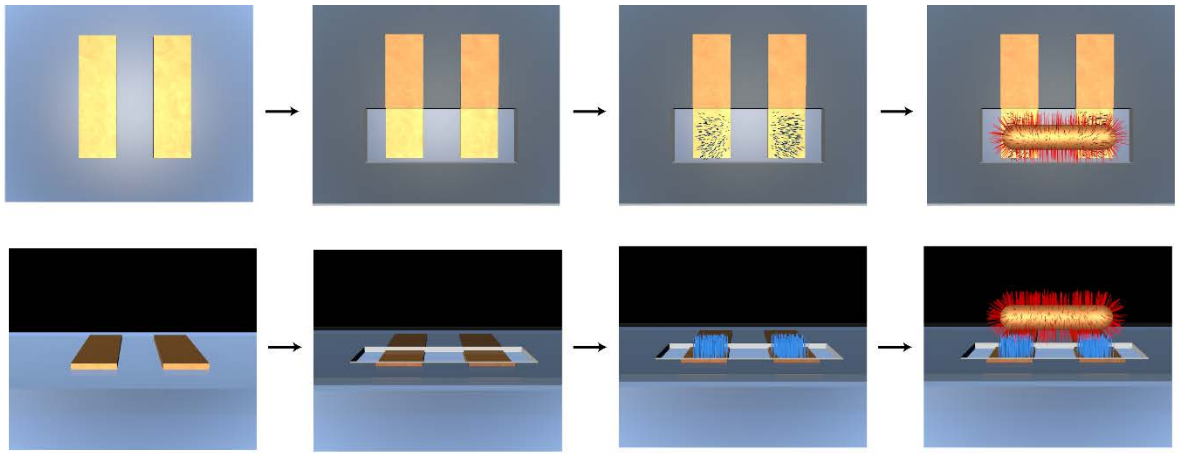

Figure 5.8: DNA assembly flow. A second layer exposure is done over the lithographed parallel rods to open a trench over the tips of the parallel rods. After a brief O_2 plasma etch to remove residual PMMA in the trench, thiolated B DNA (blue) is added. Finally, the colloidally prepared rod functionalized with complementary A DNA (red) is added and will fall into the trench and bind.

The assembly works rather well on a large scale with 96 x 16 nm rods (Figure 5.9), with variable yield (about 15-70% depending on the second layer trench and rod size combinations).

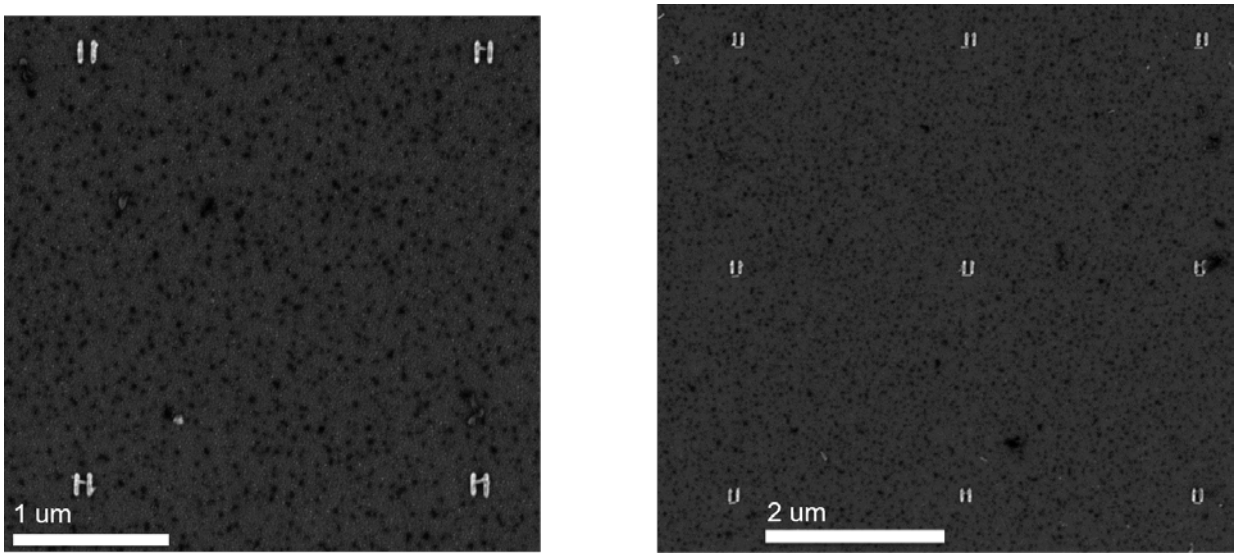

Figure 5.9: Large view SEM of DNA based assembly of orthogonal rod on parallel rods. Left: Three out of four orthogonal rods have bound about ¾ or the way up along the parallel rods. Right: rods bound along the bottom of the parallel rod structures. The rods used in this test were 96 x 16 nm, not the 96 x 30 used in the actual measurements of EIT. (Binding of these rods were higher than that of the 96 x 30 nm rods, but their plasmon resonance is too far in the red.)

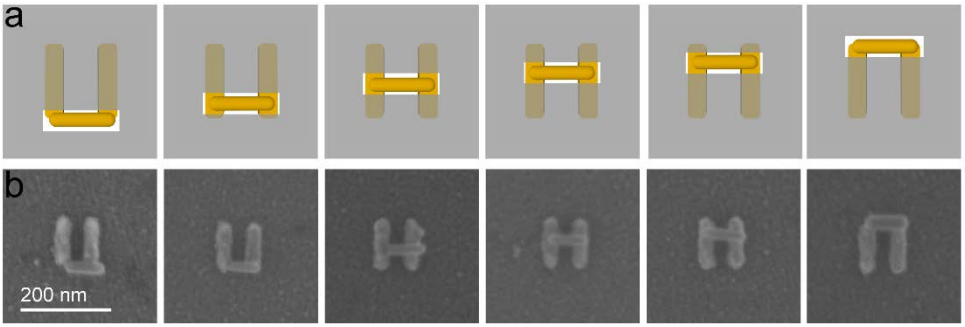

Figure 5.10: Symmetry control of organic-inorganic hybrid EIT structures. (a) Schematic showing the parallel rods covered in PMMA (grey) except for the trench opened by e-beam lithography over a specific location along the length of the parallel rods. (b) SEM images of assembled structures showing that the two layer exposure can direct assembly of the orthogonal rod over along the length of the parallel rods. The PMMA is removed for SEM acquisition because it is insulating.

At this point, I wanted to quantify what the error in rod placement was. This 'error' is the difference in the measured placement of the rod from the programmed placement of the rod (Figure 5.10). The bottom tips of the parallel rods were arbitrarily set as the '0 nm' mark. For instance, if I wanted to place the center of the orthogonal rod at the bottom tip of the parallel rods, I would open the trench so the middle of it would be at the 0 nm mark. If I measured the center of the rod at 21 nm above the bottom tips of the parallel rods, I would record that as a +21 nm from the bottom of the rods, and that would give me a +21 nm 'absolute distance from the programmed height'. Another example is if I wanted the orthogonal rods near the middle of the parallel rods, I would program the trench to be opened at 64 nm from the bottom tips of the parallel rods. If I measured the center of the orthogonal rod at 62 nm from the bottom of the parallel rods, I would record that as the measured distance, and the 'absolute distance from the programmed height' would be –2 nm because it was 2 nm bellow where I wanted it to be (Table 4). The results show that the median displacement of the measured position of the orthogonal rod from the programmed position is 7.5 nm with a standard deviation of 33 nm. This is a promising result because the median offset is within the error of the tool (±10 nm in the x and y directions) and even with a standard deviation of 33 nm, which is equivalent to the transverse axis of the colloidal rod, one would still observe an EIT effect as long as the final assembly is symmetry broken.

Table 4: Orthogonal rod placement along the parallel rods

Column Number	1,2,3	4,5,6	7,8,9	10,11,12	13, 14	15,16,17	18,19,20	21,22
Programed Height Offset from Bottom of Parallel rods (nm)	-16	0	16	32	48	64	80	96
Measured Distance from Bottom of Parallel rods to Center of Bound Orthogonal rod (nm)	-6	-50	79	15	69	45	87	*
	-19	26	-26	40	131	62	89	131
	-23	21	0	42		47	83	
		42	15	50		84	81	
		-30	-22	18		150	72	
		26	-27	79			110	
							142	
Average Distance (nm)	-16	6	3	41	100	78	95	131
Standard Deviation (nm)	9	37	41	23	44	43	24	N/A
Absolute Distance from Programmed Height	10	-50	63	-17	21	-19	7	*
	-3	26	-42	8	83	-2	9	35
	-7	21	-16	10		-17	3	
		42	-1	18		20	1	
		-30	-38	-14		86	-8	
		26	-43	47			30	
							62	
Composite Absolute Average Distance from Programmed Height	**Mean Distance: 8.9 nm** **Median Distance: 7.5 nm**							
Standard Deviation	**±33.2 nm**							

*****One data point was removed as an outlier according to the Grubbs outlier test; it was measured at -7 nm in column 21. The most reasonable explanation for this is that the structure was mislabeled as column 21 instead of column 1 or column 2 when saving the file names on the SEM.

The data is also expressed in two plots below (Figure 5.11). The plot on the left expresses the measured distance of the rod from the programmed position in terms of a histogram. The x-axis shows the absolute distance of the orthogonal rod from the programmed position. Most measurements are within ± 20 nm from where they were programmed to be along the length of the parallel rods. The graph on the right plots the programmed position of the rod versus the measured position of the rod. One would expect the slope of this line to be 1 (for every nanometer increase in programmed height along the length of the parallel rods, the measured height would correspondingly increase by one nanometer). However the best fit line (not shown for clarity) has a slope of about 1.3. This illustrates that the e-beam lithography tool coupled with the DNA assembly isn't perfect, but most data points fall within error. Overall, this process lends to acceptable control over the 2nd layer trench and directed assembly of the orthogonal rod.

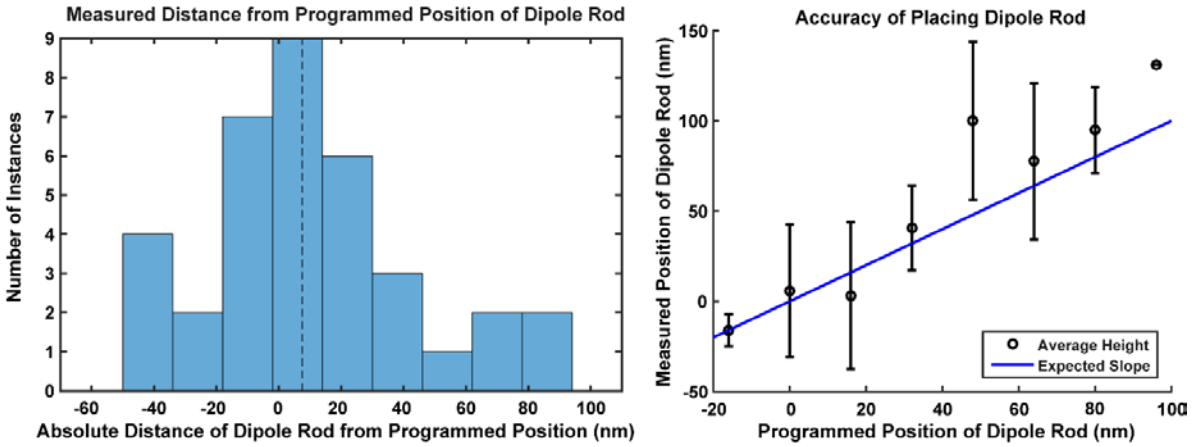

Figure 5.11: Error in placement of orthogonal rod. Left: Histogram of absolute difference in measured placement of orthogonal rod from the programmed placement relative to the bottom of the parallel rods. The median difference is 7.5 nm (dashed line). The standard deviation of the measured distance relative to the programmed distance from the 2nd layer exposure is 33 nm. Right: Plot showing the standard deviation of the measured position relative to the programmed position for each programmed position. For example, rods that were programmed to be 32 nm from the bottom of the parallel rods are centered at 41 nm and with a standard deviation of 23 nm. We expect that the slope of the measured position vs the programmed position would be unity (for every 16 nm increase in programmed position along the length of the parallel rods, the measured position should also increase by 16 nm). This is not quite the case, as the measured displacement increases by slightly more than the change in programmed displacement, the slope of the data is nearer to 1.3 than it is to 1 (blue line, 'expected slope'). This problem is most likely to some artifact in the way the electron beam lithography tool functions or to some small alignment error.

Percent Yield

An analysis of 71 structures using 96 x 30 nm rods shows that during typical assembly, orthogonal rods will bind to parallel rods 39% of the time ($\frac{28}{71}$). Of these 28 structures, 11 are assembled correctly in such a way that an EIT effect would be observed, for a total of 15% yield of correct structures out of all total chances ($\frac{11}{71}$). Therefore, of the structures in which an orthogonal rod does assemble to the parallel rods, 39% are assembled correctly ($\frac{11}{28}$). The remaining 17 structures in this sample have off target binding (orthogonal rods only on one quadrupole wire, orthogonal rods bound parallel to the quadrupole wire, or orthogonal rods binding in the gap between the parallel rods, sticking straight up in the z direction) and are discussed in detail in the Assembly Failure Mechanisms section, below.

Percent attachment and Accuracy of Placement are Inversely Related

It is interesting to note that the percent attachment of orthogonal rods to the parallel rods and the accuracy of placement are inversely related. In order to increase the efficacy of rod binding, the second layer exposure should create a wider trench, to increase the probability of a rod falling in and binding. However, the wider the trench is, the more positions the orthogonal rod could conceivably land in, leading to less control over the position of the orthogonal rod along the parallel rods. For the skinny rods (96 x 16 nm) shown in Figure 5.9, 11 out of 13 rods have bound (the trench was much wider than the rod). For the actual dark field experiments 96 x 30 rods were used with a much thinner trench width, leading to the 15% yield reported above.

Assembly Failure Mechanisms:

There are three major off-target arrangements in which a rod can bind. The likelihood of these-off target interactions can be mitigated by optimizing the conditions of the gold evaporation step for the parallel rods and the second layer exposure.

Class 1: The orthogonal rod is only attached to one parallel rod (Figure 5.12). This is most likely a result of the second layer exposure alignment issue in which the trench was only opened up over one parallel rod. One other potential cause for this is if the second layer trench is very long, perhaps 200 nm, the orthogonal rod may only come in contact with one of the two parallel rods (the minimum distance it should be is about 110 nm to account for the hydrodynamic size of the rod with DNA). To mitigate this, the maximum length of the 2nd layer trench was programmed to be 140 nm.

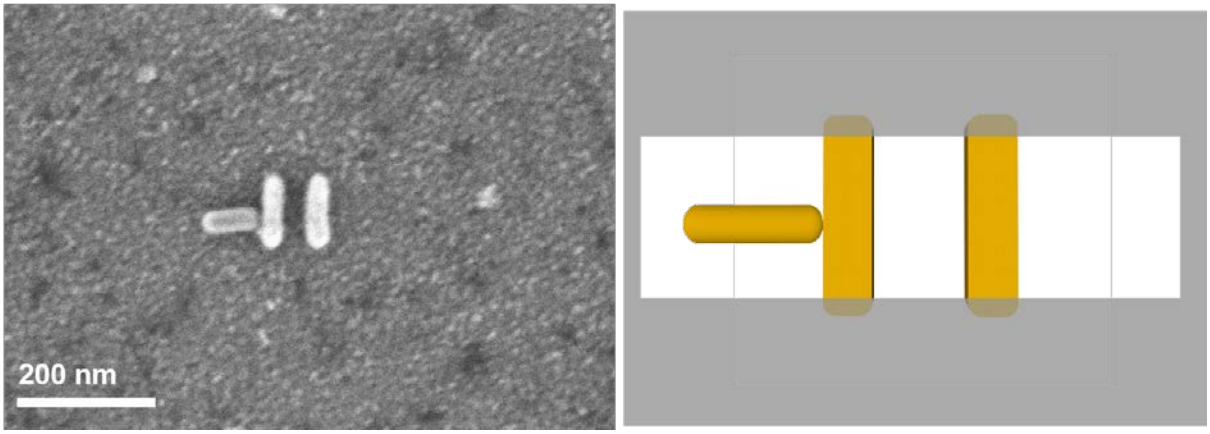

Figure 5.12: Class 1 assembly failure. The orthogonal rod is bound to just one of the two parallel rods and does not bridge the gap.

Class 2: The orthogonal rod is bound parallel to the parallel rods (Figure 5.13). This is almost certainly due to the second layer trench being too wide (the minimum distance it should be is about 50 nm to account for the hydrodynamic size of the rod with DNA). To account for the widening of the trench, perhaps the electron beam dose was too high or the residual layer was removed by too much oxygen plasma, enlarging the trench. This arrangement will maximize the DNA interactions between the orthogonal rod and the parallel rods; the full length of the rod (96 nm) could be bound on both sides for up to 192 nm of total DNA interactions maximum. In this case, the thermodynamics of binding parallel to the parallel rods would be much greater than binding orthogonally across the parallel rods.

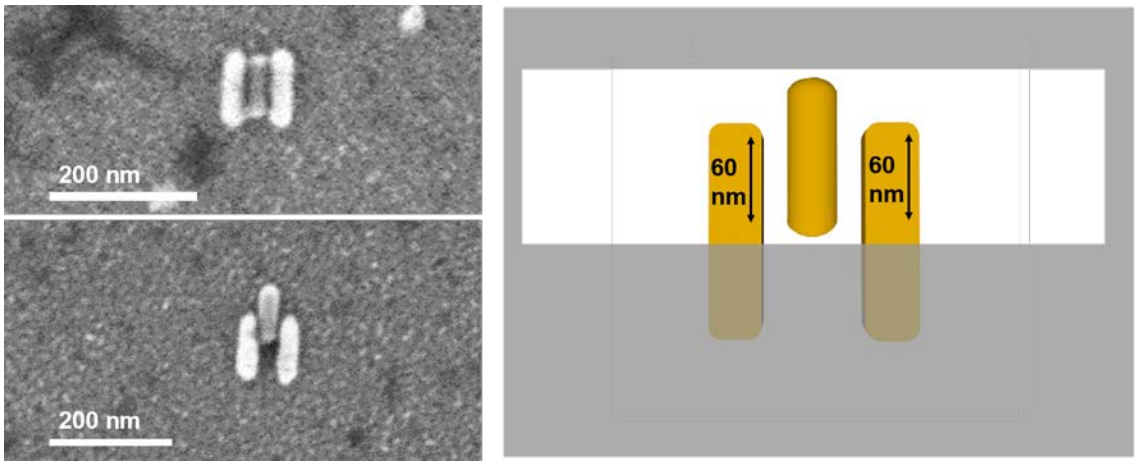

Figure 5.13: Class 2 assembly failure. The orthogonal rod falls in the gap between the parallel rods to maximize DNA connections with the DNA on the side of the lithographed parallel rods.

Class 3: The orthogonal rod is wedged between the parallel rods and is pointed in the z-direction (Figure 5.14). This is perhaps the most interesting of the three failure mechanisms, and is most likely due to DNA interactions between the orthogonal rod and various parts of the parallel rods. The parallel rods are 115 nm long and 35 nm wide on average. If the orthogonal rod bridges the two parallel rods, it will have DNA interactions with 70 nm worth of parallel rods (35 nm on each parallel rod). If the evaporated gold thickness of the parallel rods is 35 nm, then the total length of interaction the orthogonal rod will have with the insides of the parallel rods if it binds sticking straight up will be 70 nm of DNA interactions. This 70 nm of DNA interactions would mean the thermodynamics of the assembly with the orthogonal rod binding sticking straight up would be equal to that of the desired assembly. For this reason, the evaporated thickness of gold is not let to exceed 30 nm. In the 30 nm case, a rod sticking straight up will only have 60 nm of DNA interactions as opposed to 70 nm of DNA interactions if it were properly assembled across the parallel rods, and thermodynamics will favor the correct assembly. It was seen that decreasing the thickness of the parallel rods from 35 to 30 nm greatly decreases the amount of Class 3 assembly failures.

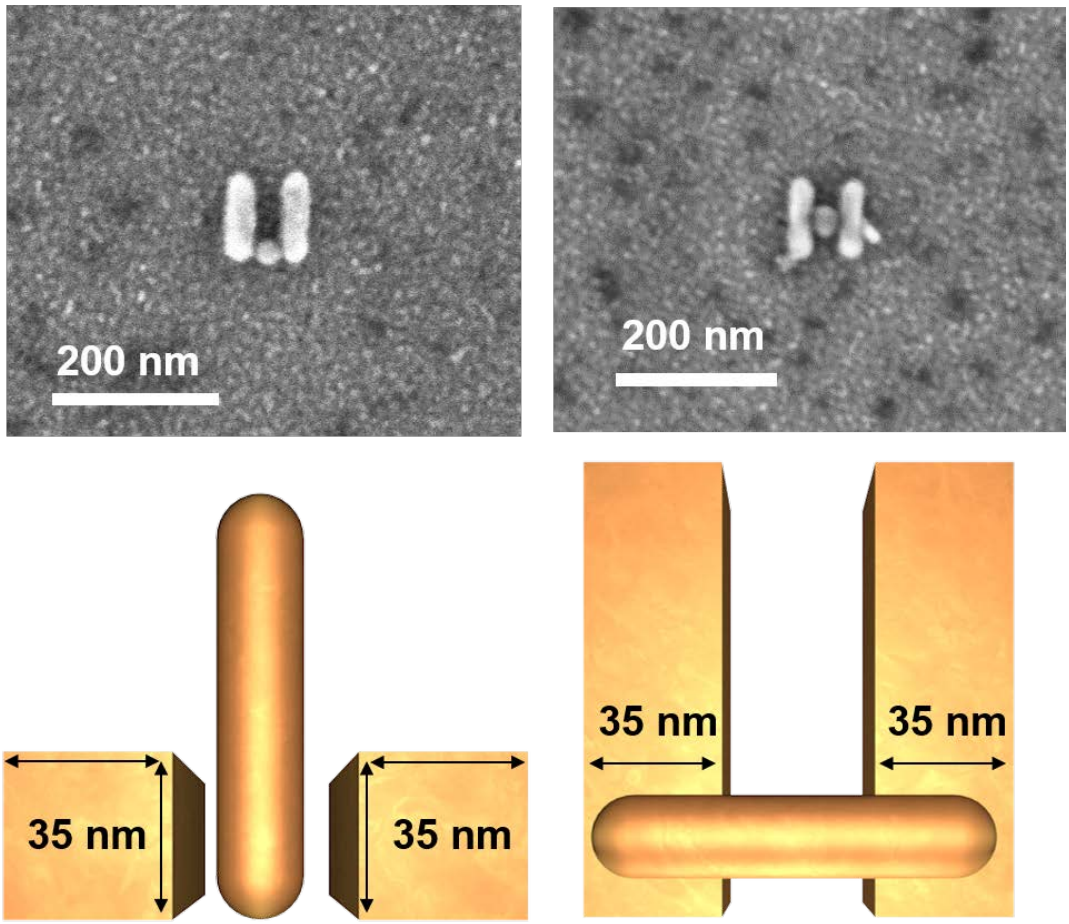

Figure 5.14: Class 3 assembly failure. The orthogonal rod falls in the gap between the parallel rods and sticks straight up to maximize DNA connections. This off-target assembly can be mitigated by making sure the parallel rods are no more than 30 nm thick.

In Chapter 5, we have shown that we can combine lithographed parallel rods with DNA self-assembly to build the structures that should exhibit EIT.

Chapter 6 : Dark Field Spectroscopy

In order to visualize our plasmonic structures on an individual particle level, we use dark field spectroscopy. This technique allows us to acquire the spectra of individual assemblies even though they are below the diffraction limit, and is an indispensable tool for validating that our structures exhibit EIT. Furthermore, flow cells can be mounted on the dark field microscope, allowing us to measure perturbations to the structure in real-time.

6.1: Dark Field Introduction

Dark field spectroscopy allows researchers to 'image' sub-diffraction sized objects. It does this by collecting the scattering of these nanoparticles. Briefly, the microscope lamp shines light through a dark field condenser, which blocks the center of this column with an annular beam block. At this point, a hollow cone of light is focused to a point on the specimen at an oblique angle. The light scattered by the plasmonic metal structures is collected by the microscope objective and directed to either the eyepiece or to the monochromator and CCD detector. The light that is transmitted through the sample will not be collected because it is sent at an oblique angle, and will miss the microscope objective. In this way, only objects that scatter light will be detected, and everything else will be dark, hence the moniker 'dark field' (Figure 6.1 and Figure 6.2).[5]

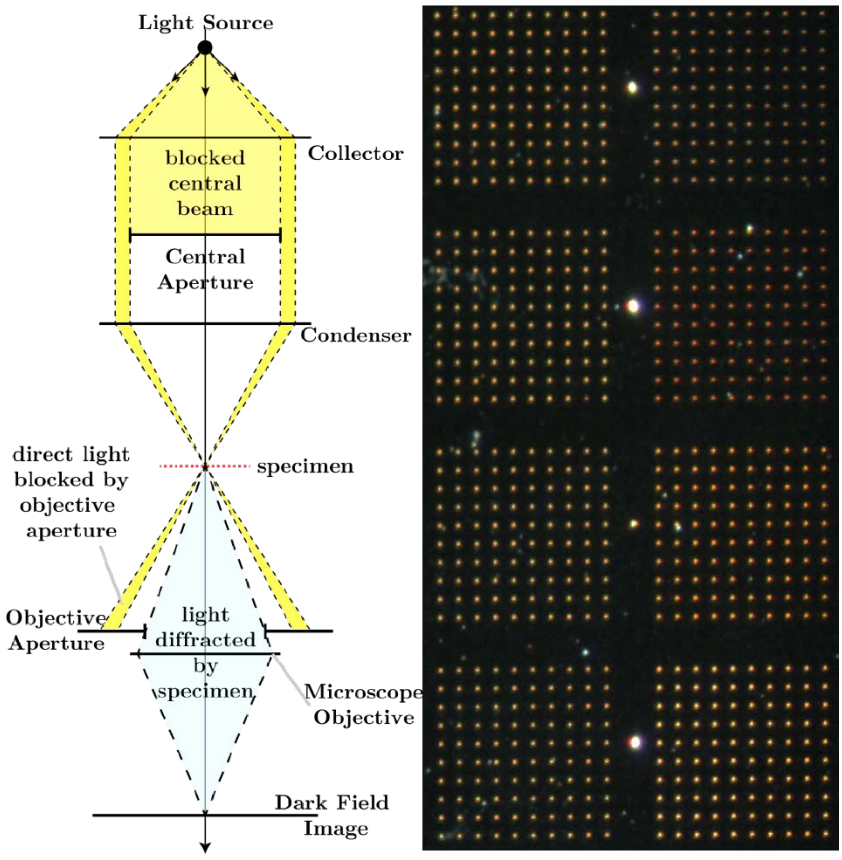

Figure 6.1: Dark field microscopy Left: Dark field microscope schematic (figure from Wikimedia Commons). Right: Picture of an array of gold nanorods of different lengths, which scatter strongly and were used as a calibration sample. Dust particles can also scatter, which is why it is important to keep the sample very clean.

For the determination of wavelength specific scattering, the scattered light is then sent to a monochromator. It first passes through an entrance slit that blocks out light from extraneous particles, such as non-specifically bound rods or dust, that could make the spectra uninterpretable (Figure 6.3). The light reflects off a flat mirror and is directed to a parabolic mirror. It then hits a grating which disperses the light based on wavelength (making a spectrum). This spectrum is re-collimated with a second parabolic mirror onto a Si CCD (Figure 6.4). This image is then exported and undergoes post processing (see section 6.5).

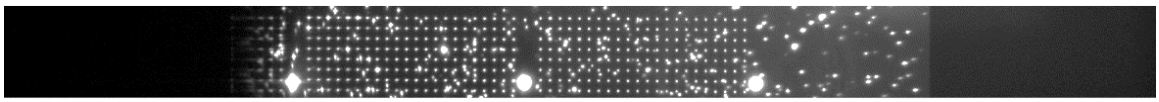

Figure 6.2: CCD image of the assembled structures in a flow cell set up. The arrays are clearly visible, but non-specifically bound rods and dust can be a problem. The brightest dots are alignment markers for SEM so the specific assembly that generates the spectra can be correlated to an SEM image of that assembly.

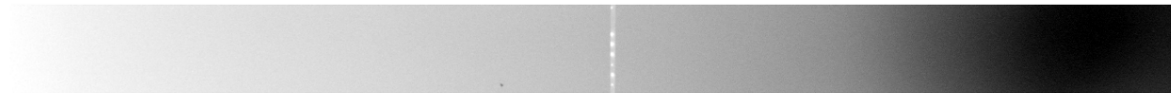

Figure 6.3: CCD of structures with slit in. Only one strip of structures (white dots in the center) can be seen. Light from all other structures are blocked with the entrance slit of the monochromator.

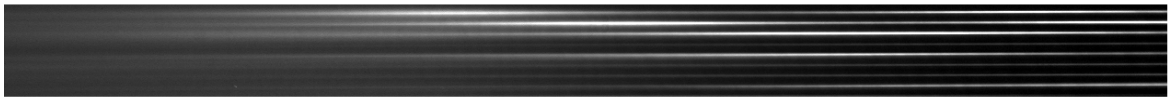

Figure 6.4: CCD spectra of individual assemblies seen through the slit. In this case, only the assemblies whose light was directed through the slit are spread after hitting the diffraction grating and are collected by the CCD. The white lines are the spectra. Where the white intensity is strongest is the maximal scattering of (or resonant frequency) of each structure.

The grating in the monochromator is blazed at 750 nm, which means that the diffraction envelope of incident light is most efficiently dispersed away from the zeroth order mode towards a higher order mode where it can be used, and that resolution (in this case) is greatest at near 750 nm. There are 300 grove per mm on the grating, which also determines the resolution of the monochoomator.[2,96]

6.2 Main Results

Because of the sheer number of experiments, I will front load the main results in this section, and the experimental and other results will be delayed for subsequent sections. The first major measurement is that of the assembled plasmonic EIT analogues (Figure 6.5). This measurement proves that the combination of lithography and DNA based self-assembly does create structures that exhibit EIT.

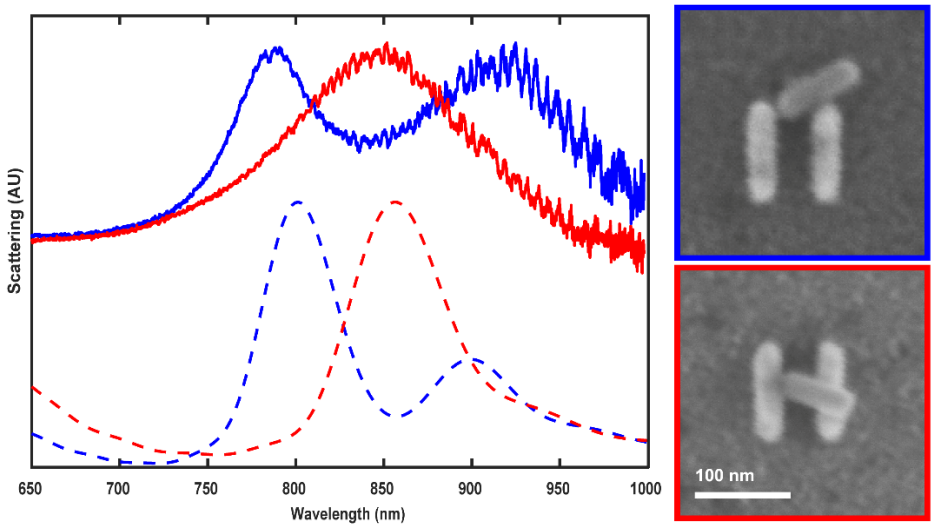

Figure 6.5: Dark field spectra of hybrid organic-inorganic structures Left: Low symmetry structure (blue solid line) and high symmetry structure (red solid line). The Lumerical FDTD simulations closely match for both the low and high symmetry structures (blue and red dashed lines, respectively). Right: Correlative SEM of low symmetry structure (top, blue box) and high symmetry structure (bottom, red box).

The next major result is that of DNA based dynamics of these structures, which are the major accomplishments of this thesis (Figure 6.6). In the first novel experiment, conducted in a flow cell set-up (see Appendix 6), spectra are taken of fully assembled structures that are thought to exhibit EIT. They are hydrated in a 0.5 M NaCl buffer solution, and then a 0.01% SDS solution is flowed in, bringing the concentration of Na^+ to $3.5 * 10^{-4}$ M. This should lower the T_m of the solution (see section 5.1.2) to below room temperature, causing the DNAs to electrostatically repel one another and disassemble. This structural change is reflected in the spectral data; we see the scattering spectra exhibits two peaks that change into one peak upon the addition of the SDS solution. The peak that remains (or appears) is the dipolar resonance from the parallel rods. This experiment shows that by tuning the salt concentration, the orthogonal rod can be plasmonically decoupled from the parallel rods through chemical means, causing the EIT feature to disappear.

The second experiment demonstrates that dehydrating the DNA will cause it to collapse (Figure 6.6). This should bring the orthogonal rod closer to the parallel rods, causing them to plasmonically couple more strongly, which should increase the extent of EIT splitting. The dehydration is achieved by exposing the DNA to acetone, then isopropanol, followed by high vacuum. The spectrum for the hydrated assembly shows two peaks rather close together, and when the structure is dehydrated, the width of the transparency window increases by about 100 nm (the change in DNA distance is expected to be around 10 nm).[97] This strong response shows the true potential of this technique in seeing very large spectral changes in small distance variation of this metamaterial.

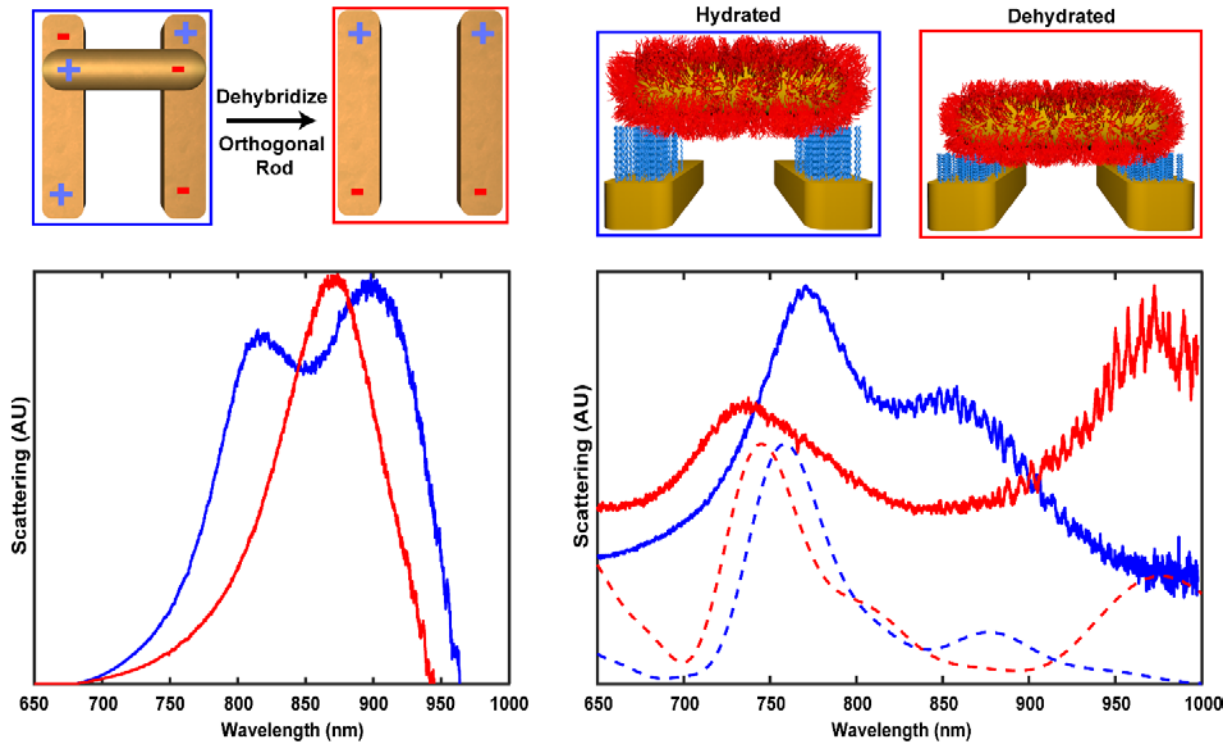

Figure 6.6: DNA dynamics. Left: Dehybridization of rods due to removing sodium ions. The orthogonal rod is electrostatically repelled from the parallel rods, and the EIT feature disappears as the rods decouple. Right: Modulation of dynamics by dehydrating the DNA. This causes the orthogonal rod to couple more strongly with the parallel rods, enhancing the EIT effect.

Upon further asnalysis, the appearance of the red peak upon salt based dehybridization of the orthogonal rod is unexpected. We attribute it to the 'dipole resonance of the parallel rods' but that mode should not be excited by the orthogonally polarized light. After several control experiments with only the parallel rods (results not shown), it was clear that the polarizer could not completely eliminate modes coming from the parallel rods—the measured dark field signal of the parallel rods with parallel polarization is about twice as intense as the signal of the parallel rods with orthogonal polarization (this turns out to be because the dark field optics in a transmittance set up will not completely preserve the polarization of the light). Figure 6.6 shows the normalized scattering of the rods, but the un-normalized scattering shows that the red peak we see, if it is from the parallel rods, is actually always there and is a hidden component of the blue spectra seen in buffer. If we subtract the SDS peak from the buffer peak, we should see the true peak of the EIT structure with the orthogonal polarization (because we subtracted out the parallel polarization). This black trace shows a very nice transparency window, and a very nice EIT effect, which is what we expect to see (Figure 6.7).

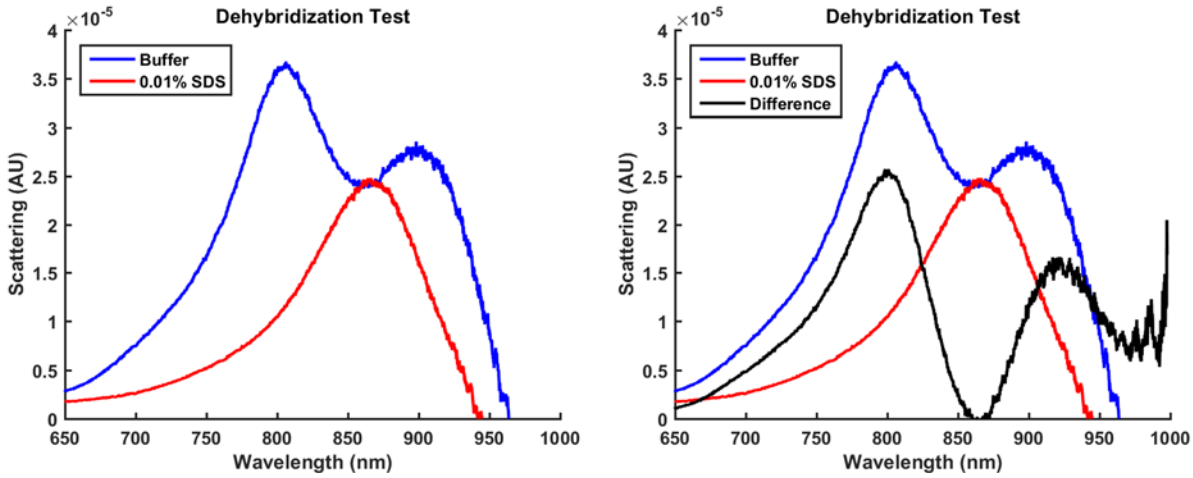

Figure 6.7: Data correction for dehybridization of EIT structures. Left: un-normalized data showing that the peak in the 0.01% SDS solution is less intense than the assembled structure in buffer. Right: When this less intense peak in SDS is subtracted from the spectra in the buffer, a very nice EIT effect is observed. This black trace is what we think the 'true' EIT spectra in buffer solution should be.

6.3: Experimental

For the experiments, I place a linear polarizer (effective from 600 to 1100 nm) in between the lamp and the dark field condenser (NA 1.2-1.4). This ensures that the incident light is polarized along the orthogonal rod, and that the EIT effect can be observed. The light is collected in a 40x air objective (NA 0.60). I also place a petri dish with water on top of the linear polarizer to act as a filter to absorb IR light that could be absorbed by the buffer and detrimentally heat the sample. Our microscope has three viewing ports—one to the eye pieces, one to a camera to take pictures of what the sample looks like, and one to a spectrometer and CCD that will capture the spectrum of individual assemblies.

6.3.1: Sample Preparation for DNA Hydrated/Dehydrated Tests.

A detailed version of the sample preparation is described in Appendix 7. Because it would be experimentally difficult to use a flow cell to dehydrate the system, we simply take the hydrated spectra using the lithographed arrays on a glass slide, with some buffer and a coverslip to protect it from the immersion oil. After the hydrated spectra are acquired, we removed the coverslip and washed off the salt using a 0.3 M ammonium acetate solution (ammonium acetate is a salt that can be sublimated away), and removed the PMMA with acetone followed by isopropanol, and dried with N_2 gas. We then placed the slide in the SEM to correlate the spectra to actual assemblies. After SEM, we took these now dehydrated slides (with their DNA collapsed), and took dark field images of the same assemblies (Figure 6.6).

6.3.2: Flow Cell of Intercalators and Ethanol

The next step was to try to fine tune the change of DNA on a much smaller scale—instead of removing the orthogonal rod by lowering the cation concentration or completely collapsing the DNA, a more nuanced approach was desired. We sought to manipulate the DNA by only a few nanometers using reversible methods, such as introducing DNA intercalators or by changing the dielectric constant, to cause the DNA to reversibly collapse in the flow cell. We then planned to flow in buffer to restore the original state.

The first attempt was to insert an intercalator between the stacked bases of the DNA to push them apart. There are many molecules that can do this, and the literature is especially focused on such molecules that become fluorescent only upon binding, as they are commonly used as dyes for DNA electrophoresis.[98–100] Ethidium bromide is one of the most common intercalators, and has been used to expand the rise per base of DNA assembled nanoparticle superlattices.[101] We chose to use the intercalator SYBR gold due to health and safety concerns over ethidium bromide. It is worth noting that the health and safety of SYBR gold is not currently known as it is a proprietary compound, so safety precautions equal to that if we were using ethidium bromide were instated. FDTD simulations show that there would be a small but certainly observable decoupling effect if the intercalators bound in the DNA (one intercalator per three DNA bases) with an expansion of 3 angstroms per intercalated SYBR gold (Figure 6.8).[102]

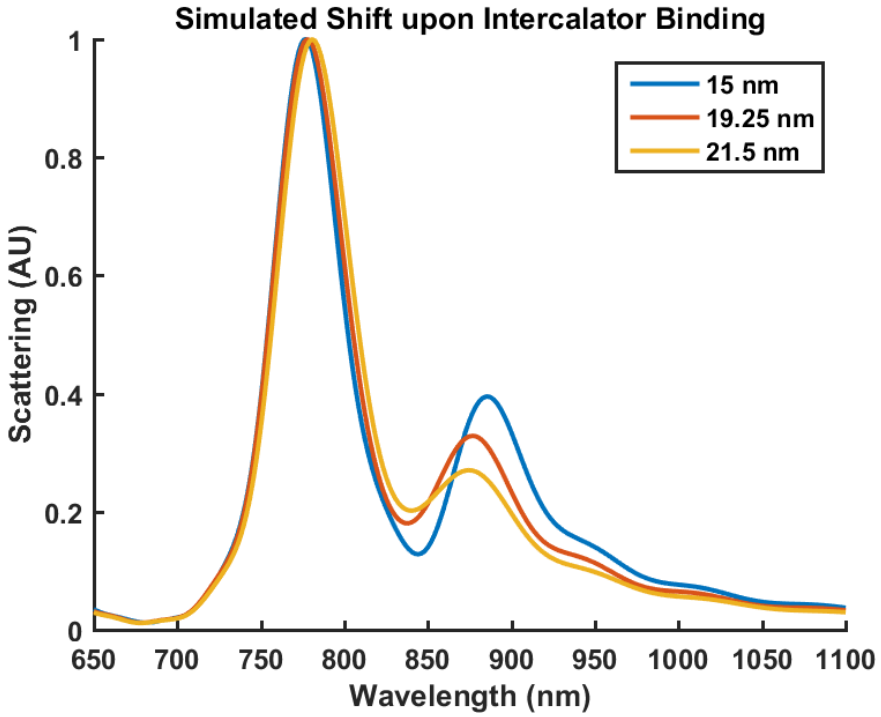

Figure 6.8: Lumerical FDTD simulation of EIT response to intercalators. By flowing in SYBR gold, we expected to expand the DNA distance from the programmed 15 nanometers to almost 22 nanometers, weakening the EIT effect.

However, the actual results were equivocal; no real difference could be seen between the structures in buffer with or without the intercalators. There were some shifts, but the shifting was not consistent in any one direction (Figure 6.9).

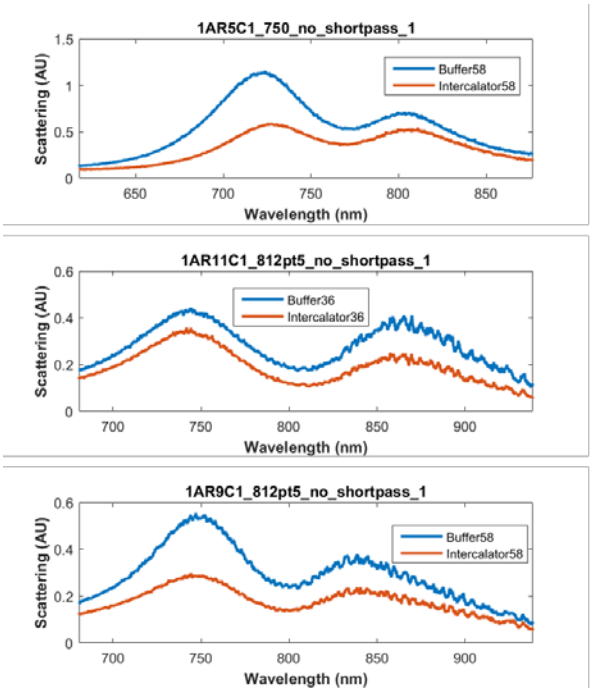

Structure Name	Shift of High Energy Peak (bluer peak) in nm	Shift of Low Energy Peak (redder peak) in nm
1AR5C1	+ 1.7	-1.6
1AR11C1	-2.9	0
1AR9C1	0.4	0.8

Figure 6.9: Intercalator results. Single assembly spectra for structures in buffer are shown in blue, and the same structures after flowing in SYBR gold are shown in orange. The table on the right shows the peak shifts for each structure—these representative results show that there is little to no shift in these experiments.

We decided that perhaps slightly moving the orthogonal rod away from parallel rods was too weak of an effect to be properly seen. Instead, we decided to change the dielectric conditions of the assembly by flowing in a mixture of buffer and ethanol. Jarad Mason's work in the Mirkin group has shown that this can cause DNA assembled superlattices to contract.[79] FDTD simulations predicted a slightly larger shift (Figure 6.10). To test this, we flowed in a solution of 50% ethanol, and 50% 0.3 M NaCl, 0.01 M PBS buffer. Like the intercalator study, we saw equivocal results, and no consistant change upon going from buffer to an ethanol solution (Figure 6.11).

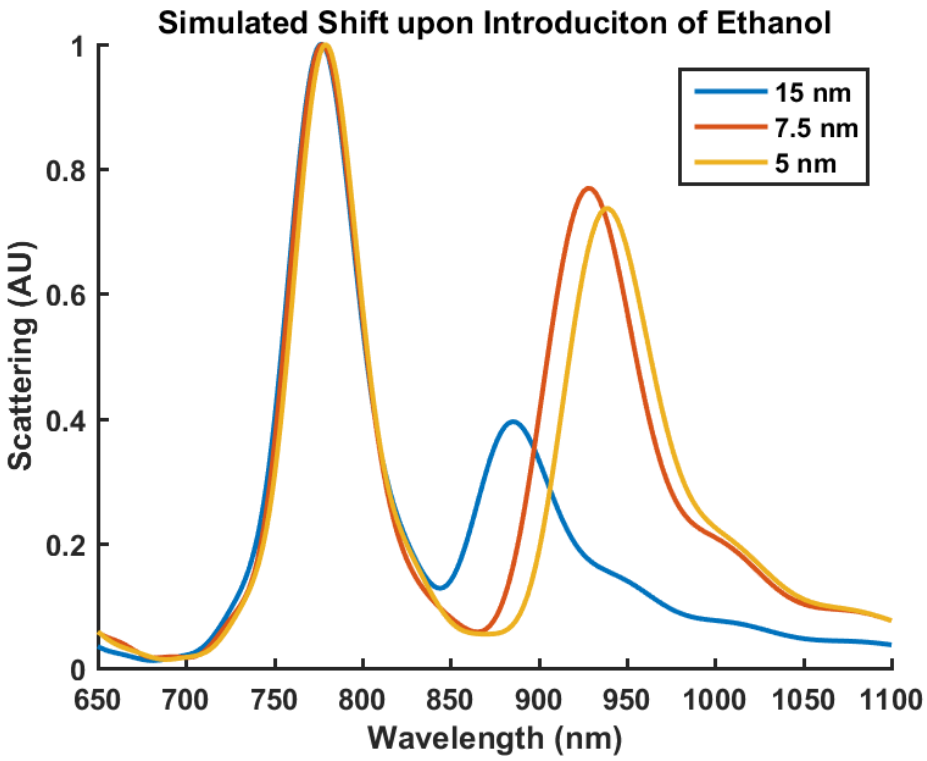

Figure 6.10: Lumerical FDTD simulation of EIT response to changing dielectric. By flowing ethanol, we expected to shrink the DNA distance from the programmed 15 nanometers to 5 nanometers, greatly increasing the EIT splitting.

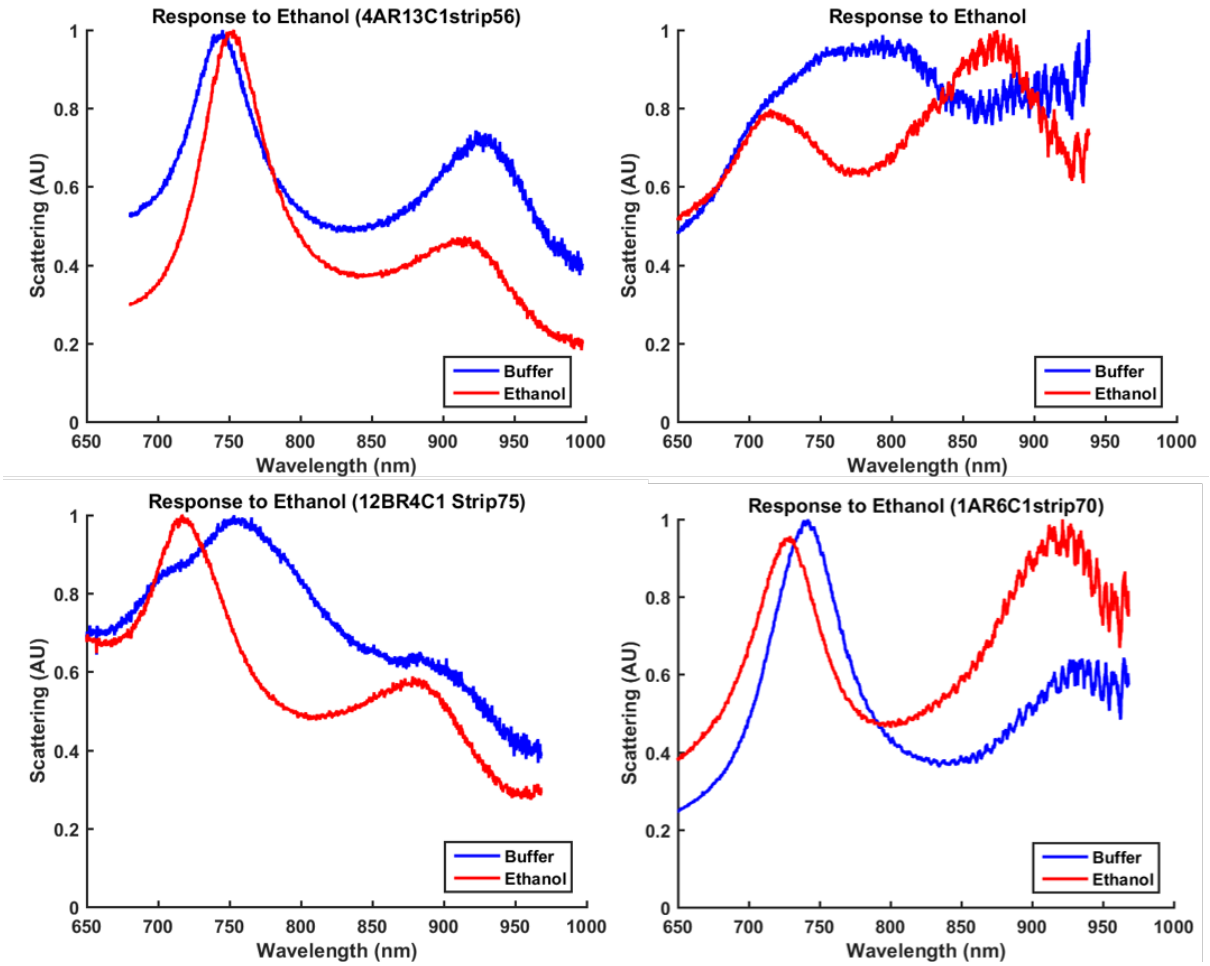

Figure 6.11: Response of structures to 50% ethanol/buffer solution. Spectra of structures in buffer are shown in blue, and the spectra of the same structure in ethanol/buffer solution is shown in red. There is much less movement in these structures than one expects from FDTD simulations, and the results are equivocal.

We believe that the failed dynamics may stem from the fact that there could be non-specific interactions between the DNA on the orthogonal rod and the PMMA side walls of the trench, preventing the orthogonal rod from moving very much. One reason for this is that it is consistent with other results. For the DNA collapsing tests, the PMMA trench was removed with acetone—in this case, the DNA on the orthogonal rod would be free to move. In the dehybridization test, the low salt concentration would cause the negatively charged rod to leave the trench completely as it would be repelled by the negatively charged DNA on the parallel rods. Further experiments should be done to remove the PMMA after assembly, and then mount the slide into a flow cell and try again.

6.4: Dark Field problems

Salt based changes in flow cell

As noted in the experimental section, when I conducted the dehybidization tests, I would see an unexpected peak from the just the parallel rods that should not have been excited by the orthogonally polarized light. Sometimes this peak from the parallel rods was strong enough that

the low energy peak from the assembled structures in buffer were in the same place. Subtracting the peak seen in the 0.01% SDS solution from the EIT feature seen in buffer exposes the 'true' EIT peak that one would expect to see if the polarization were perfect. It is very important that the intensity for these experiments are not normalized (they were initially normalized to easily visualize the peak shift), as this can lead to very misleading graphs where it can look like the peak 'doesn't shift' upon removal of the orthogonal rod. That could lead to the misinterpretation that the orthogonal rod is only contributing to the high energy peak for many of the structures (Figure 6.12 and Table 5).

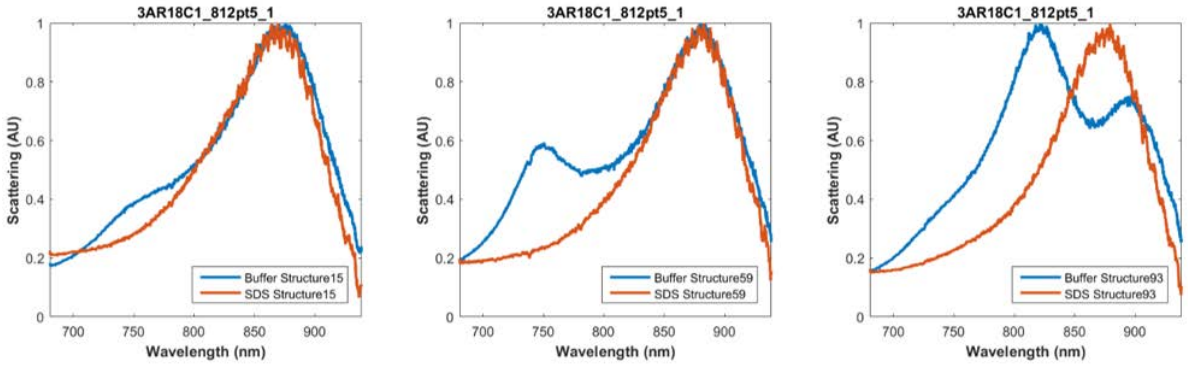

Figure 6.12: Normalized peak changes upon flowing 0.01% SDS solution to dehybridize rods. The blue trace is in buffer, the orange trace is in SDS. The leftmost spectrum does not appear be an EIT structure, but has a weird shoulder that indicates that it potentially could be. The middle spectrum shows two peaks going to one, but the second peak overlaps exactly with the low energy mode to the EIT. The right spectrum more obviously corresponds to a correctly dehybridized structure.

Table 5: Peak shifts in flow cell for twenty-two normalized structures

	Change upon Flow with Water (4 nm or more shift)	Static upon Flow with Water (4 nm or less shift relative to separate QW)	Change upon Flow with Water (10 nm or more shift)	Static upon Flow with Water (10 nm or less shift relative to separate QW)
Number	10	12	5	17
Percent	45%	55%	23%	77%

When the data is plotted in an non-normalized fashion and the peak from the parallel rods in SDS is subtracted from the structure in buffer, a much clearer EIT peak will appear, which we believe is close to the 'true' EIT peak that should be seen in buffer, as the parallel polarization of the parallel rods are now subtracted out (Figure 6.13).

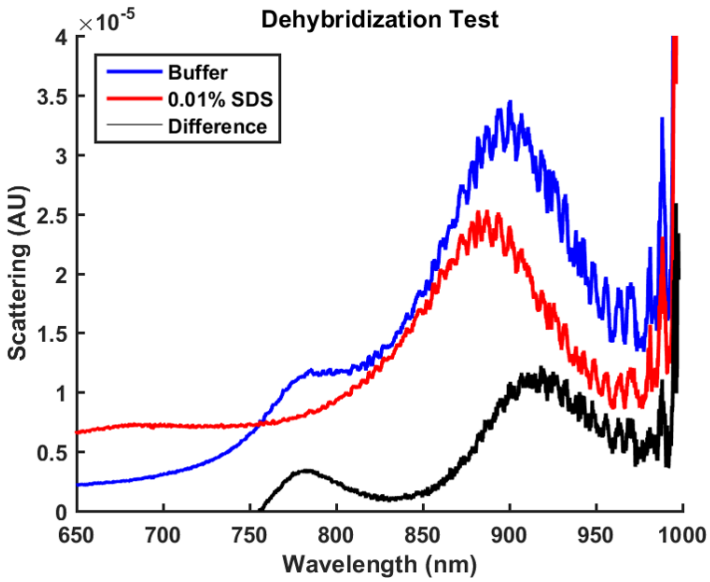

Figure 6.13: Correction for parallel rod peak during dehybridization tests.In this case, it is clear to see that the resonance from the parallel rods played a large role in the spectra taken in buffer, but if it removed, the EIT feature is more clearly seen. The EIT feature in this case is not great because the peak from the parallel polarization of light is rather strong.

Non-specific binding of rods to the surface and cleaning of the rods

The DNA coated rods can sometimes non-specifically stick to the PMMA during the three and a half hour incubation. To try to combat this, the slide is washed vigorously with buffer (sprayed from a pipette or a syringe) over the region of interest, and is submerged in a buffer solution overnight. This cleaning procedure works to varying degrees of success depending on the sample. The most surefire way to remove non-specifically bound rods is to remove the PMMA with acetone followed by an IPA rinse (standard sample prep before putting the slide in the SEM). Brief bursts of sonication (three seconds) will sometimes work to remove the rods, but not always (Figure 6.14). It is not clear why there is such variability in the cleaning procedures. The reason why the PMMA is not always removed before dark field imaging is that it acts a protective layer from the coverslips to prevent the assembled structures from being scratched off. However, future work with the ethanol and intercalators should probably be conducted without a PMMA layer.

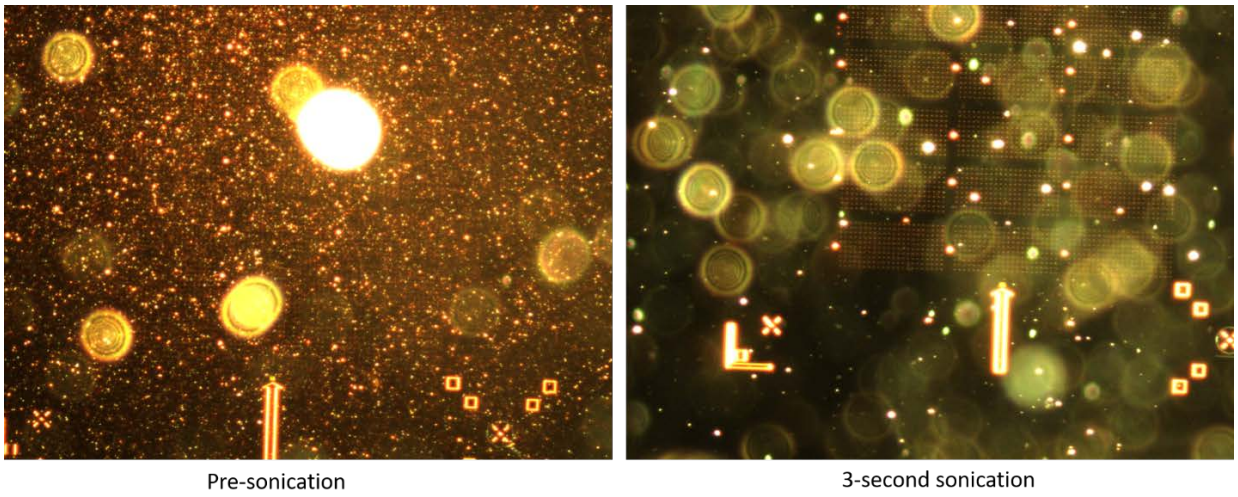

Figure 6.14: Non-specific binding of DNA coated rods to PMMA. Left: Dark field image of flow cell after 3.5 hour incubation and vigorous washing with buffer shows that rods still bind to the surface (the many, many small dots of light). Right: Sometimes quick sonication of the same substrate can remove the rods that ware bound to the surface, and the grid of structures is able to be seen. The arrow and boxes are alignment markers that are visible in both the pre and post-sonicated images.

Dark Field False Positive of EIT:

Occasionally, the dark field spectra alone will give a false positive. For instance, if the second layer exposure is off by several nanometers (but still under the diffraction limit so it can't be detected in dark field as a separate scattering spot), and the orthogonal rod manages to bind non-specifically to the ITO coated cover slip, the dark field spectra of the diffraction limited spot will contain spectral information for both the lithographed parallel rods and the isolated orthogonal rods, even though they are not properly assembled (Figure 6.15). Because the dipole resonance and the resonance from the parallel rods are spectrally distinct, two peaks will be observed in the dark field scattering spectrum (Figure 6.16). In these cases, the structure is not expected to be dynamic, so the spectra should not change upon changing the environment. Therefore, the dynamic tests discussed earlier ought to be able to discriminate between properly assembled EIT and these false positives. It should be noted that in the instances when the second layer exposure is so far off, none of the assemblies on the entire slide will be correct.

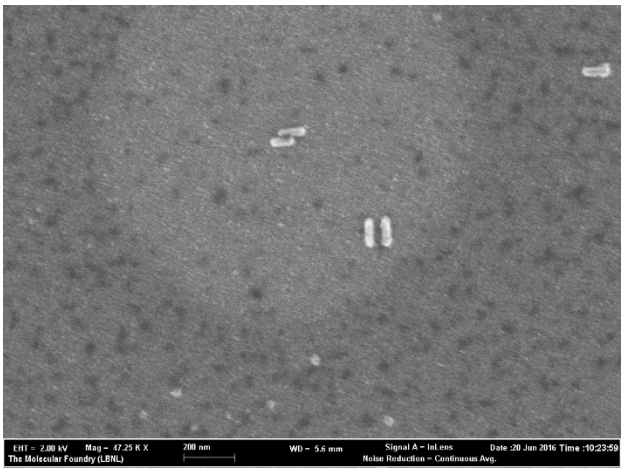

Figure 6.15: SEM of false positive of EIT. SEM showing poor second layer exposure leads to orthogonal rods non-specifically binding to the ITO surface within the diffraction limited spot of the parallel rods. This can lead to false positive EITs.

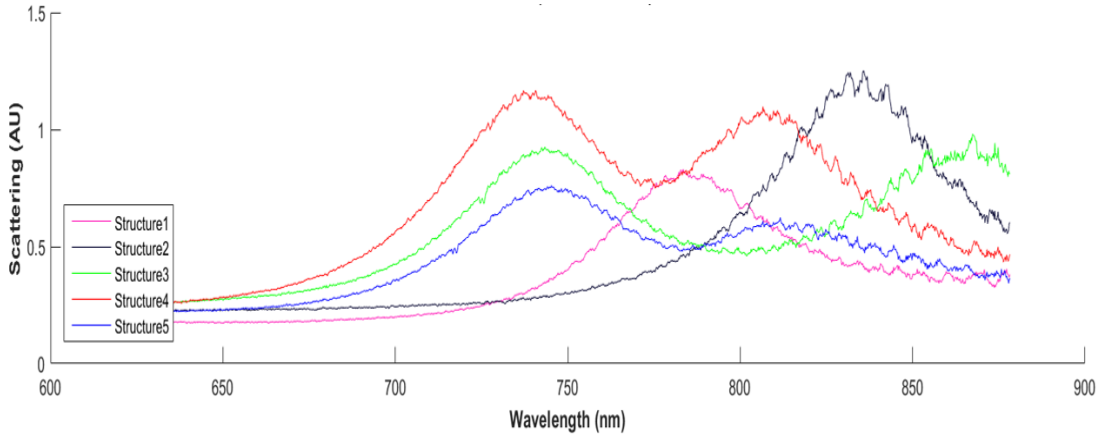

Figure 6.16: Dark field of false positive EIT. The red, blue, and green traces show two peaks, but the structure is not properly assembled (see Figure 6.15).

6.5: MATLAB Processing and Analysis

The raw data from the dark field is given on a 1340 × 100 pixel CCD and outputted as a grey scale image. The *x*-axis, which is 1340 pixels long, is in wavelength, while the y-axis, which is 100 pixels tall, represents the spatial position of the arrayed gold structure. The intensity of each pixel from the CCD is proportional to the number of scattered photons collected at that wavelength and position (Figure 6.17).

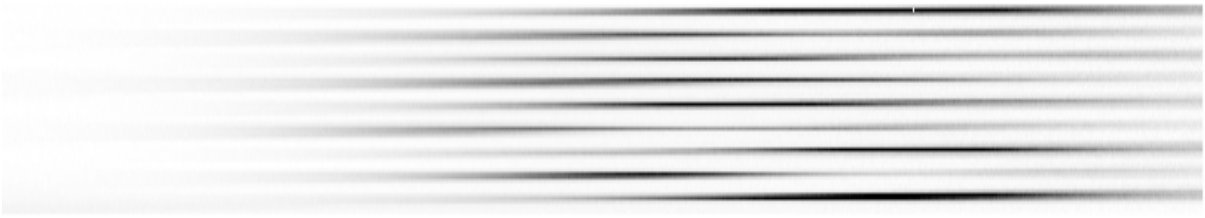

Figure 6.17: Si CCD of arrayed structures (reverse color). The y-axis is physical space, and the x-axis is wavelength. The spectra of each structure appears as a black strip, and the darker areas correspond to higher intensity scattering—closer to the plamson resonance of the assembly.

In post-processing, the numerical value of each greyscale pixel is converted to intensity, and in this case the more photon counts at that pixel, the more 'black' it is, and the fewer photon counts, the lighter it is. Because the assembled structures are lithographed in neat arrays, more than one assembled structure is present in the field of view at once. On average, the spectra from eight assemblies can simultaneously be collected. Custom MATLAB code is then used to scan down the spatial axis and see how many 'bright' maxima are present. Each maxima corresponds to a structure.

Because of the large number of groves on the grating (300 groves per mm), a range of only 250 nm can be acquired at a time. Therefore, each structure has at least three spectra taken to cover the wavelength range of interest, one with the grating centered at 750 nm, 812.5 nm, and 875 nm. The spectra for individual assemblies are stitched together using a weighted average. That is, when stitching spectra together in their overlapping regions, if two pixels for the same wavelength have different intensities, the data point taken with the grating centered at a nearer wavelength to the point in question is given more weight.

A well-known problem with Si CCD detectors is that they begin to suffer from an effect known as etaloning in the near IR (Figure 6.18).[103] This effect induces periodic oscillations in the spectra that are artifacts of the detector. In order to try to reduce this effect, a calibrated lamp with known intensity (HL3 plus Vis-NIR light source calibrated for absolute irradiance, 350-2400 nm, Ocean Optics) was used to generate a calibration file for the spectrometer in an attempt to post-process out the etaloning error. This techniques was met with limited to mild success.

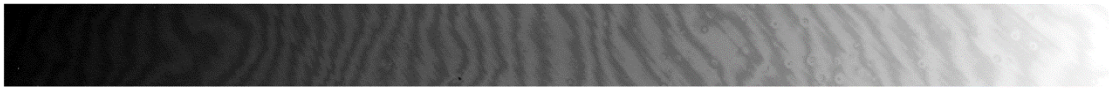

Figure 6.18: CCD image of etaloning. Ocean Optics source with the grating centered at 875 nm. On the right side of the image (longer wavelengths) the oscillating intensity changes are more pronounced (white is higher intensity).

To generate the lamp spectra by which we divide our data to see only the scattered light, we divide the spectra of our structures either by the NIST lamp data or the scattering of a piece of Teflon tape, which we can approximate as a white light scatterer. Other research groups using a transmission dark field set up use random dust particles on their sample as a white light scatterer, which we believe may not as accurate as the Teflon tape to scatter white light.[104] (In reflectance dark field set ups, a mirror can be used to get the lamp spectrum.)

In summary, dark field spectroscopy allows us to visualize single assemblies that exhibit EIT (or not), and can track their dynamics as they are dehybridized or are dehydrated. It is an invaluable tool for measuring the spectra of these dynamic metamaterials.

Chapter 7 : Conclusions

In this dissertation, a metamaterial that exhibits EIT and responds to a chemical stimulus has been assembled through a combination of the lithographic techniques and DNA mediated self-assembly. Two chemical stimuli were successfully tested; concentration of sodium ions can be used to decouple the plasmonic components and decrease the EIT effect, and the DNA can be dehydrated to make the nanorods couple more strongly, enhancing the EIT effect. This thesis serves as a step-by-step guide into designing a fabricating such a device, and details various successes and drawbacks of this approach.

This responsive metamaterial might be particularly useful in the area of biological sensing. By measuring the change in the EIT effect (which is non-linear to displacement of the orthogonal rod), one could back out the interaction of the DNA with whatever molecule or stimuli is perturbing the DNA. In this way, it might be possible to gain insight into DNA/analyte interactions. Such a system would be an improvement over the plasmon rulers discussed in Chapter 5. The work presented in this dissertation represents a step forward in creating a dynamic, chemically responsive metamaterial and could be applied to advancing the efficacy of functional materials.

References

(1) Wasilewski, P.; Kletetschka, G. *Geophys. Res. Lett.* **1999**, *26* (15), 2275–2278.

(2) Hecht, E. *Optics*, 3rd ed.; Addison Wesley Longman: Reading, Massachusettes, 1998.

(3) Feynman, R. P. *Am. Phys. Soc.* **1959**, 22–36.

(4) Alivisatos, A. P. *Science.* **1996**, *271* (5251), 933–937.

(5) Pelton, M.; Bryant, G. *Introduction to Metal-Nanoparticle Plasmonics*, 1st ed.; John Wiley & Sons, and Science Wise Publishing: Hoboken, New Jersey, 2013.

(6) Kundu, P. K.; Samanta, D.; Leizrowice, R.; Margulis, B.; Zhao, H.; Börner, M.; Udayabhaskararao, T.; Manna, D.; Klajn, R. *Nat. Chem.* **2015**, *7* (August).

(7) Douglas, S. M.; Bachelet, I.; Church, G. M. *Science* **2012**, *335* (6070), 831–834.

(8) Liu, Y.; Zhang, X. *Chem. Soc. Rev.* **2011**, *40* (5), 2494–2507.

(9) Kanté, B.; Park, Y.-S.; O'Brien, K.; Shuldman, D.; Lanzillotti-Kimura, N. D.; Jing Wong, Z.; Yin, X.; Zhang, X. *Nat. Commun.* **2012**, *3*, 1180.

(10) Wu, C.; Khanikaev, A. B.; Shvets, G. *Phys. Rev. Lett.* **2011**, *106* (10), 1–4.

(11) Ni, X.; Wong, Z. J.; Mrejen, M.; Wang, Y.; Zhang, X. *Science.* **2015**, *349* (6254), 1310–1314.

(12) Biagioni, P.; Huang, J.-S.; Hecht, B. *Rep. Prog. Phys.* **2012**, *75* (2), 24402.

(13) Boller, K.; Imamoğlu, A.; Harris, S. E. *Phys. Rev. Lett.* **1991**, *66* (20), 2593–2596.

(14) Garrido Alzar, C. L.; Martinez, M. a. G.; Nussenzveig, P. *Am. J. Phys.* **2002**, *70* (1), 37.

(15) Liu, N.; Langguth, L.; Weiss, T.; Kästel, J.; Fleischhauer, M.; Pfau, T.; Giessen, H. *Nat. Mater.* **2009**, *8* (9), 758–762.

(16) Gu, J.; Singh, R.; Liu, X.; Zhang, X.; Ma, Y.; Zhang, S.; Maier, S. a.; Tian, Z.; Azad, A. K.; Chen, H.-T.; Taylor, A. J.; Han, J.; Zhang, W. *Nat. Commun.* **2012**, *3*, 1151.

(17) Zhang, S.; Genov, D. A.; Wang, Y.; Liu, M.; Zhang, X. *Phys. Rev. Lett.* **2008**, *101* (4), 1–4.

(18) Liu, N.; Hentschel, M.; Weiss, T.; Alivisatos, A. P.; Giessen, H. *Science* **2011**, *332* (June), 1407–1410.

(19) Kane Yee. *IEEE Trans. Antennas Propag.* **1966**, *14* (3), 302–307.

(20) Angelopoulos, M. *IBM J. Res. Dev.* **2001**, *45* (1), 57–75.

(21) Zailer, I.; Frost, J. E. F.; Chabasseur-Molyneux, V.; Ford, C. J. B.; Pepper, M. *Semicond. Sci. Technol.* **1996**, *11* (8), 1235–1238.

(22) Chang, T. H. P. *J. Vac. Sci. Technol.* **1975**, *12* (6), 1271–1275.

(23) Gorelick, S.; Guzenko, V. a; Vila-Comamala, J.; David, C. *Nanotechnology* **2010**, *21* (29),

295303.

(24) McPeak, K. M.; Jayanti, S. V.; Kress, S. J. P.; Meyer, S.; Iotti, S.; Rossinelli, A.; Norris, D. J. *ACS Photonics* **2015**, 150213102249000.

(25) O'Handley, R. C.; Burge, D. K.; Jasperson, S. N.; Ashley, E. J. *Surf. Sci.* **1975**, *50* (2), 407–433.

(26) Rodahl, M.; Höök, F.; Krozer, A.; Brzezinski, P.; Kasemo, B. *Rev. Sci. Instrum.* **1995**, *66* (7), 3924–3930.

(27) Lu, C.; Lewis, O. *J. Appl. Phys.* **1972**, *43* (11), 4385–4390.

(28) Tesler, A. B.; Maoz, B. M.; Feldman, Y.; Vaskevich, A.; Rubinstein, I. *J. Phys. Chem. C* **2013**, *117* (21), 11337–11346.

(29) Benjamin, P.; Weaver, C. *Proc. R. Soc. A Math. Phys. Eng. Sci.* **1960**, *254* (1277), 177–183.

(30) Vogt, K. W.; Kohl, P. A.; Carter, W. B.; Bell, R. A.; Bottomley, L. A. *Surf. Sci.* **1994**, *301* (1–3), 203–213.

(31) Jiao, X.; Goeckeritz, J.; Blair, S.; Oldham, M. *Plasmonics* **2009**, *4* (1), 37–50.

(32) Aouani, H.; Wenger, J.; Gérard, D.; Rigneault, H.; Devaux, E.; Ebbesen, T. W.; Mahdavi, F.; Xu, T.; Blair, S. *ACS Nano* **2009**, *3* (7), 2043–2048.

(33) Kuttge, M.; Vesseur, E. J. R.; Verhoeven, J.; Lezec, H. J.; Atwater, H. A.; Polman, A. *Appl. Phys. Lett.* **2008**, *93* (11).

(34) Kannan, B.; Kulkarni, R. P.; Majumdar, A. *Nano Lett.* **2004**, *4* (8), 1521–1524.

(35) Personick, M.; Mirkin, C. *J. Am. Chem.* … **2013**, *135* (49), 18238–18247.

(36) Niu, W.; Zheng, S.; Wang, D.; Liu, X.; Li, H.; Han, S.; Chen, J.; Tang, Z.; Xu, G. *J. Am. Chem. Soc.* **2009**, *131* (2), 697–703.

(37) Ye, X.; Gao, Y.; Chen, J.; Reifsnyder, D. C.; Zheng, C.; Murray, C. B. *Nano Lett.* **2013**, *13* (5), 2163–2171.

(38) Walsh, M. J.; Barrow, S. J.; Tong, W.; Funston, A. M.; Etheridge, J. *ACS Nano* **2015**, *9* (1), 715–724.

(39) Frens, G. *Nat. Phys. Sci.* **1973**, *241* (105), 20–22.

(40) Turkevich, J.; Stevenson, P. C.; Hillier, J. *Discuss. Faraday Soc.* **1951**, *11* (c), 55.

(41) LaMer, V. K.; Dinegar, R. H. *J. Am. Chem. Soc.* **1950**, *72* (11), 4847–4854.

(42) Murray, C. B.; Kagan, C. R.; Bawendi, M. G. *Annu. Rev. Mater. Sci.* **2000**, *30* (1), 545–610.

(43) Polte, J.; Ahner, T. T.; Delissen, F.; Sokolov, S.; Emmerling, F.; Thünemann, A. F.; Kraehnert, R. *J. Am. Chem. Soc.* **2010**, *132* (4), 1296–1301.

(44) Bastús, N. G.; Comenge, J.; Puntes, V. *Langmuir* **2011**, *27* (17), 11098–11105.

(45) Reiss, H. *J. Chem. Phys.* **1952**, *20* (8), 1216–1227.

(46) Zheng, H.; Smith, R. K.; Jun, Y. -w.; Kisielowski, C.; Dahmen, U.; Alivisatos, A. P. *Science.* **2009**, *324* (5932), 1309–1312.

(47) Peng, X.; Wickham, J.; Alivisatos, a P. *J. Am. Chem. Soc.* **1998**, *120* (21), 5343–5344.

(48) Jana, N. R.; Gearheart, L.; Murphy, C. J. *J. Phys. Chem. B* **2001**, *105* (19), 4065–4067.

(49) Murphy, C. J.; Jana, N. R. *Adv. Mater.* **2002**, *14* (1), 80–82.

(50) Nikoobakht, B.; El-sayed, M. A. **2003**, No. 16, 1957–1962.

(51) Ye, X.; Zheng, C.; Chen, J.; Gao, Y.; Murray, C. B. *Nano Lett.* **2013**, *13* (2), 765–771.

(52) Chargaff, E. *Experientia* **1950**, *6* (6), 201–209.

(53) Franklin, R. E.; Gosling, R. G. *Nature* **1953**, *171* (4356), 740–741.

(54) Watson, J. D.; Crick, F. H. C. *Nature* **1953**, *171* (4356), 737–738.

(55) Nelson, D. L.; Cox, M. M. *Lehninger Principles of Biochemistry*, 5th ed.; W. H. Freeman and Company: New York, 2009.

(56) Franklin, R. E.; Gosling, R. G. *Nature* **1953**, *172* (4369), 156–157.

(57) Matray, T. J.; Kool, E. T. *J. Am. Chem. Soc.* **1998**, *120* (24), 6191–6192.

(58) Jin, R.; Wu, G.; Li, Z.; Mirkin, C. a; Schatz, G. C. *J. Am. Chem. Soc.* **2003**, *125* (6), 1643–1654.

(59) Seeman, N. C. *J. Theor. Biol.* **1982**, *99* (2), 237–247.

(60) Zheng, J.; Birktoft, J. J.; Chen, Y.; Wang, T.; Sha, R.; Constantinou, P. E.; Ginell, S. L.; Mao, C.; Seeman, N. C. *Nature* **2009**, *461* (7260), 74–77.

(61) He, Y.; Ye, T.; Su, M.; Zhang, C.; Ribbe, A. E.; Jiang, W.; Mao, C. *Nature* **2008**, *452* (7184), 198–201.

(62) Li, Y.; Liu, Z.; Yu, G.; Jiang, W.; Mao, C. *J. Am. Chem. Soc.* **2015**, 150331070322009.

(63) Alivisatos, A.; Johnsson, K.; Peng, X.; Wilson, T. E.; Loweth, C. J.; Bruchez, M. P. J.; Schultz, P. G. *Nature* **1996**, *382* (15), 609–611.

(64) Mirkin, C.; Letsinger, R.; Mucic, R.; Storhoff, J. *Nature* **1996**, *382* (15), 607–609.

(65) Jones, M. R.; Seeman, N. C.; Mirkin, C. A. *Science.* **2015**, *347* (6224), 1260901–1260901.

(66) Claridge, S. A.; Goh, S. L.; Fréchet, J. M. J.; Williams, S. C.; Micheel, C. M.; Alivisatos, A. P. *Chem. Mater.* **2005**, *17* (7), 1628–1635.

(67) Mastroianni, A. J.; Claridge, S. a; Alivisatos, a P. *J. Am. Chem. Soc.* **2009**, *131* (24), 8455–8459.

(68) Yan, W.; Xu, L.; Xu, C.; Ma, W.; Kuang, H.; Wang, L.; Kotov, N. A. *J. Am. Chem. Soc.*

2012, *134* (36), 15114–15121.

(69) Sönnichsen, C.; Reinhard, B. M.; Liphardt, J.; Alivisatos, A. P. *Nat. Biotechnol.* **2005**, *23* (6), 741–745.

(70) Liu, G. L.; Yin, Y.; Kunchakarra, S.; Mukherjee, B.; Gerion, D.; Jett, S. D.; Bear, D. G.; Gray, J. W.; Alivisatos, a P.; Lee, L. P.; Chen, F. F. *Nat. Nanotechnol.* **2006**, *1* (1), 47–52.

(71) Jun, Y.-W.; Sheikholeslami, S.; Hostetter, D. R.; Tajon, C.; Craik, C. S.; Alivisatos, A. P. *Proc. Natl. Acad. Sci.* **2009**, *106* (42), 17735–17740.

(72) Lee, S. E.; Chen, Q.; Bhat, R.; Petkiewicz, S.; Smith, J. M.; Ferry, V. E.; Correia, A. L.; Alivisatos, A. P.; Bissell, M. J. *Nano Lett.* **2015**, *15* (7), 4564–4570.

(73) Macfarlane, R. J.; Lee, B.; Jones, M. R.; Harris, N.; Schatz, G. C.; Mirkin, C. A. *Science.* **2011**, *334* (October), 204–208.

(74) Macfarlane, R. J.; Jones, M. R.; Senesi, A. J.; Young, K. L.; Lee, B.; Wu, J.; Mirkin, C. A. *Angew. Chemie Int. Ed.* **2010**, *49* (27), 4589–4592.

(75) Jones, M. R.; Macfarlane, R. J.; Lee, B.; Zhang, J.; Young, K. L.; Senesi, A. J.; Mirkin, C. A. *Nat. Mater.* **2010**, *9* (11), 913–917.

(76) Auyeung, E.; Cutler, J. I.; Macfarlane, R. J.; Jones, M. R.; Wu, J.; Liu, G.; Zhang, K.; Osberg, K. D.; Mirkin, C. A. *Nat. Nanotechnol.* **2011**, 1–17.

(77) Macfarlane, R. J.; Jones, M. R.; Lee, B.; Auyeung, E.; Mirkin, C. a. *Science* **2013**, *341* (6151), 1222–1225.

(78) Young, K. L.; Jones, M. R.; Zhang, J.; Macfarlane, R. J.; Esquivel-Sirvent, R.; Nap, R. J.; Wu, J.; Schatz, G. C.; Lee, B.; Mirkin, C. a. *Proc. Natl. Acad. Sci.* **2012**, *109* (7), 2240–2245.

(79) Mason, J. A.; Laramy, C. R.; Lai, C. T.; O'Brien, M. N.; Lin, Q. Y.; Dravid, V. P.; Schatz, G. C.; Mirkin, C. A. *J. Am. Chem. Soc.* **2016**, *138* (28), 8722–8725.

(80) Rothemund, P. W. K. *Nature* **2006**, *440* (7082), 297–302.

(81) Dietz, H.; Douglas, S. M.; Shih, W. M. *Science.* **2009**, *325* (5941), 725–730.

(82) Marras, A. E.; Zhou, L.; Su, H.-J.; Castro, C. E. *Proc. Natl. Acad. Sci.* **2015**, *112* (3), 713–718.

(83) Kühler, P.; Roller, E.-M.; Schreiber, R.; Liedl, T.; Lohmüller, T.; Feldmann, J. *Nano Lett.* **2014**.

(84) Kuzyk, A.; Schreiber, R.; Fan, Z.; Pardatscher, G.; Roller, E.-M.; Högele, A.; Simmel, F. C.; Govorov, A. O.; Liedl, T. *Nature* **2012**, *483* (7389), 311–314.

(85) Zhou, C.; Duan, X.; Liu, N. *Nat. Commun.* **2015**, *6*, 8102.

(86) Kuzyk, A.; Schreiber, R.; Zhang, H.; Govorov, A. O.; Liedl, T.; Liu, N. *Nat. Mater.* **2014**, *13* (9), 862–866.

(87) Urban, M. J.; Dutta, P. K.; Wang, P.; Duan, X.; Shen, X.; Ding, B.; Ke, Y.; Liu, N. *J. Am. Chem. Soc.* **2016**, *138* (17), 5495–5498.

(88) Urban, M. J.; Zhou, C.; Duan, X.; Liu, N. *Nano Lett.* **2015**, *15* (12), 8392–8396.

(89) Douglas, S. M.; Marblestone, A. H.; Teerapittayanon, S.; Vazquez, A.; Church, G. M.; Shih, W. M. *Nucleic Acids Res.* **2009**, *37* (15), 5001–5006.

(90) Pryce, I. M.; Aydin, K.; Kelaita, Y. A.; Briggs, R. M.; Atwater, H. A. *Nano Lett.* **2010**, *10* (10), 4222–4227.

(91) Jeong, Y.-G.; Han, S.; Rhie, J.; Kyoung, J.-S.; Choi, J.-W.; Park, N.; Hong, S.; Kim, B.-J.; Kim, H.-T.; Kim, D.-S. *Nano Lett.* **2015**, *15* (10), 6318–6323.

(92) Smith, J. M. Anisotropies in discrete DNA-assembled gold nanoparticle structures, University of California, Berkeley, 2014.

(93) Ma, W.; Kuang, H.; Wang, L.; Xu, L.; Chang, W.-S.; Zhang, H.; Sun, M.; Zhu, Y.; Zhao, Y.; Liu, L.; Xu, C.; Link, S.; Kotov, N. A. *Sci. Rep.* **2013**, *3* (Copyright (C) 2014 U.S. National Library of Medicine.), 1934.

(94) Claridge, S. A.; Liang, H. W.; Basu, S. R.; Fréchet, J. M. J.; Alivisatos, a P. *Nano Lett.* **2008**, *8* (4), 1202–1206.

(95) O'Brien, M. N.; Radha, B.; Brown, K. A.; Jones, M. R.; Mirkin, C. A. *Angew. Chemie Int. Ed.* **2014**, *53* (36), 9532–9538.

(96) Pedrotti, F. L.; Pedrotti, L. S.; Pedrotti, L. M. *Introduction to Optics*, 3rd ed.; Pearson Addison Wesley: San Francisco, 2007.

(97) Radha, B.; Senesi, A. J.; O'Brien, M. N.; Wang, M. X.; Auyeung, E.; Lee, B.; Mirkin, C. A. *Nano Lett.* **2014**, *14* (4), 2162–2167.

(98) LePecq, J. B.; Paoletti, C. *J. Mol. Biol.* **1967**, *27* (1), 87–106.

(99) Rye, H. S.; Yue, S.; Wemmer, D. E.; Quesada, M. a; Haugland, R. P.; Mathies, R. a; Giazer, A. N. *Nucleic Acids Res.* **1992**, *20* (11), 2803–2812.

(100) Bahrami, A. R.; Dickman, M. J.; Matin, M. M.; Ashby, J. R.; Brown, P. E.; Conroy, M. J.; Fowler, G. J. .; Rose, J. P.; Sheikh, Q. I.; Yeung, A. T.; Hornby, D. P. *Anal. Biochem.* **2002**, *309* (2), 248–252.

(101) Pal, S.; Zhang, Y.; Kumar, S. K.; Gang, O. *J. Am. Chem. Soc.* **2015**, *137* (12), 4030–4033.

(102) Biebricher, A. S.; Heller, I.; Roijmans, R. F. H.; Hoekstra, T. P.; Peterman, E. J. G.; Wuite, G. J. L. *Nat. Commun.* **2015**, *6*, 7304.

(103) *Spectroscopic Etaloning in Back Illuminated CCDs (Princeton Instruments)*; 1997.

(104) Fu, Y. H.; Kuznetsov, A. I.; Miroshnichenko, A. E.; Yu, Y. F.; Luk'yanchuk, B. *Nat. Commun.* **2013**, *4*, 1527.

(105) Hurst, S. J.; Lytton-Jean, A. K. R.; Mirkin, C. a. *Anal. Chem.* **2006**, *78* (24), 8313–8318.

Appendix 1: Materials & Buffers

Chemicals:

DL-dithiothreitol (DTT, 99%), sodium phosphate monobasic (NaH_2PO_4, 99%), sodium phosphate dibasic (Na_2HPO_4, 99%), sodium dodecyl sulfate (SDS, 99%), Gold (III) chloride trihydrate ($HAuCl_4 \cdot 3H_2O$, ≥ 99.0%), Silver nitrate ($AgNO_3$ ≥ 99.999%), Sodium borohydride ($NaBH_4$ ≥ 99.99%), Ascorbic acid (≥ 99.0%), hydrogen peroxide (30% in water), Hydrochloric Acid (HCl, 37% in water), and isopropanol (IPA, 99.5 %) were purchased from Sigma Aldrich. Acetone (99.5 %), Nitric Acid (15.8N), Ammonium acetate (98.5%), and sodium chloride (NaCl, ≥ 99.0%) were purchased from Fisher Scientific. Hexadecyltrimethylammonium bromide (CTAB, ≥ 98.0%) and sodium oleate (≥ 97.0%) were purchased from TCI America. All oligonucleotides were purchased from Integrated DNA Technologies. Poly methyl methacrylate, (PMMA, 950K, 4% in anisole) and methyl isobutyl ketone (MIBK/IPA 1:3 Developer) were purchased from MicroChem. Sulfuric acid (95%) was purchased from EMD Millipore. Milli-Q water (18.2 MΩ·cm) generated from a Synergy® Water purification system purchased from EMD millipore was used in all the experiments. Gold grain/shot (99.990% purity) for evaporation was obtained through the Lawrence Berkeley National Lab Precious Metals Program.

Buffers:

To prepare a 0.17M phosphate buffer used to cleave the disulfides that might be present in the DNA stock solution, 11.4681g Na_2HPO_4 and 0.5085g NaH_2PO_4 are dissolved in 500 mL of Milli-Q water. For actual reduction of a DNA solution, 0.0154 g of DTT was added to a 1 mL aliquot of this stock.

The 0.1 M Phosphate Buffer, pH = 7.4, was a precursor for other buffers, and was made by dissolving 5.7 g Na_2HPO_4 and 1.18 g NaH_2PO_4 were dissolved in 500 mL of Milli-Q water.

The linking buffer was used to hybridize the orthogonal rod to the parallel rods was composed of 0.01% SDS, 0.01M PBS (a 10x dilution of the 0.1M phosphate buffer), and 0.5 M NaCl.

Appendix 2: Preparation of Lithographed Arrays

The first laborious step in lithography is to clean everything and make sure that there is no dust. A single dust particle in the region of interest can ruin an entire exposure, and therefore, the experiment.

Glass coverslips (24 x 60 x 0.17 mm) were cleaned via sonication for 20 minutes while submerged in acetone followed by a 20 minute sonication in isopropanol. They were then dried thoroughly with nitrogen gas. The dry coverslips were then submerged in fresh piranha (3:1 sulfuric acid to hydrogen peroxide) for 5 minutes, and vigorously cleaned in MilliQ water. They were then dipped in isopropanol and dried with nitrogen gas.

Safety Note: It is imperative that all organic residue is removed from the glass slide before submerging in piranha, as piranha will violently react with organics.

A 10 nm of ITO was evaporated on the glass slide to make it more conductive for e-beam lithography. The ITO coated coverslips were then sonicated again in acetone followed by isopropanol (20 minutes each), and dried under nitrogen gas. Next, 950 PMMA in anisole (A4) was spin coated on the slide for 30 seconds at 4000 rpm. They were baked on a 150 °C hotplate for 5 minutes. The resulting height of the PMMA layer was approximately 190 nm as measured by an Alpha-Step IQ Surface Profiler.

The first layer parallel rods and alignment markers were written via e-beam lithography (CRESTEC CABL Series High Resolution Electron Beam Lithography Systems, Japan) with a 50 keV acceleration voltage. After exposure, the patterns were developed in 3:1 IPA to MIBK developing solution for 2 minutes, followed by 1 minute in pure IPA, and dried under nitrogen gas.

The second layer exposure was done as follows. 950 PMMA A4 was spin coated on the parallel rods at 4000 rpm for 30 seconds, baked at 150 °C for 5 minutes, and e-beam lithography is performed as before. This second layer exposes the trenches that guide assembly of the colloidal orthogonal rods binding to the parallel rods. These openings are about 140 nm by 55 nm as measured by SEM (they need to be rather large, as the hydrodynamic radius of the colloidal rods with DNA is close to 120 x 50 nm). The second layer exposure is then developed in 1:3 MIBK to IPA for 2 minutes, rinsed in IPA for 1 minute, and dried under nitrogen gas.

Appendix 3: Gold Nanorod Synthesis

Before starting, all glassware was cleaned with aqua regia (3:1 HCl to HNO_3) and rinsed with copious amounts of Milli-Q water.

First, a growth solution was made by dissolving 3.6 g of CTAB and 0.4936 g of sodium oleate in 100 mL of Milli-Q water at 50 °C. The solution was allowed to cool to 30 °C, and 7.2 mL of 0.004 M silver nitrate was added to the solution, and was stirred for 15 minutes. Next, 100 mL of 0.001M $HAuCl_4 \cdot 3H_2O$ was added and stirred for 90 minutes, until the solution turned clear (Au^{3+} is reduced to the metastable Au^{1+}).

While the gold growth solution was sitting for 90 minutes, the, gold seeds were made by diluting 5 mL of a 0.2M stock solution of CTAB with 2.5 mL of MilliQ water and 2.5 mL of 0.001M solution of $HAuCl_4 \cdot 3H_2O$, at 30 °C. Next, 0.6 mL of fresh 0.01M $NaBH_4$ was diluted to 1mL of ice cold water and was injected into the seed solution to reduce the gold, and stirred vigorously for two minutes. The seed solution was then allowed to age for 30 minutes with no stirring.

Next, after the growth solution had stirred for 90 minutes, 0.6 mL of 37% HCl was added to the growth solution, and was stirred at 400 rpm for 15 minutes. Next, 0.5 mL of 0.064 mM of ascorbic acid was added. Finally, 100 µL of the as synthesized seeds were added to the solution, and the rods were left at 30 °C overnight. Rods were spun down twice and resuspended in Milli-Q water.

A trick to increase the uniformity and quality of the nanoparticles is to ‘dispose’ of a small portion of the pellet when decanting the supernatant after centrifugation. The nanoparticles that are not as tightly packed into the pellet are usually the smaller and spherical products, and will more easily leave with the supernatant. The remaining rods in the pellet are therefore of higher quality. Xingchen’s explanation to me probably puts it best, “Don’t try to save every nanoparticle when you decant the supernatant. If the is a little runny and you lose some particles, those are the spheres. The rest is what we care about.”

Appendix 4: DNA Addition to Rods

DNA is added to rods according to previous methods.[75,95] As-synthesized rods were brought to 0.05M CTAB in such a concentration that the OD_{760} (the longitudinal peak) of the solution was 1. In order to functionalize the rods with DNA, 1 OD_{260} of DNA is needed per mL of diluted rod solution. For example, if 12 mL of rods in 0.05M CTAB is to be functionalized, 12 OD_{260} of DNA A Anchor is needed.

This DNA A Anchor is first incubated with DTT (0.1M, or 0.0154g DTT/mL) in a pH 8.4 PBS buffer and is allowed to sit for one hour to reduce any disulfide linkages between the 3'thiols on the DNA. The total volume of this solution should be less than 0.5mL so it can be easily purified in a NAP-5 column (GE Healthcare).

While the DNA incubates with the DTT, the rods are centrifuged at 11,000 rcf for 10 minutes, and the supernatant is carefully discarded. The rods are resuspended in equal amount of Milli-Q water. The rods are centrifuged for a second time at 11,000 rcf for 10 minutes, the supernatant is carefully discarded, and resuspended in a smaller amount of water (around 0.4mL).

The DNA A Anchor with reduced thiols is purified by running it through a NAP-5 column, and is added directly to the cleaned and concentrated rod solution.

Note: Add the purified DNA as soon as possible to the spun down rods, as the rods will start to etch and become more sphere-like because they have no ligand to stabilize them when they are in Milli-Q water. Also the reduced DNA will start to reform disulfides if they sit too long after being purified by NAP-5 column without being added to the gold nanorods. The first rod centrifugation is usually done before running the DNA through the column and the second centrifugation is done while the DNA is running through the column.

After 30 minutes to 1 hour, the rod/DNA solution is brought to 0.01% SDS and 0.01M PBS (pH 7), and sits for an additional 30 minutes to 1 hour at 37 C.

In 30 minute increments, an amount of 2.0 M NaCl is added to bring the total concentration to 0.05 M, 0.1 M, 0.2 M, 0.3 M 0.4 M and finally 0.5 M NaCl. The rod solution is kept at 37 C throughout, and it is sonicated and vortexed for 10 seconds before each addition of salt (this increases the DNA loading on the gold nanorods).[105] After the final salting, the rods with DNA should sit undisturbed for 16 hours to allow for maximal loading.

Next, the rods are spun down three times at 10,000 rcf for 7 minutes, and resuspended in 0.01% SDS only (there is no salt or PBS in this solution). On the final resuspension, use only a little amount of solvent, like 100-500 µL, and transfer to a microcentrifuge tube. Using only a little solvent for the resuspension makes the subsequent steps more facile.

At this time, the concentration of rods is determined via UVvis (the extinction coefficient used is $1.1*10^9$ $M^{-1}*cm^{-1}$).[75] Linker A DNA at 20,000x rod concentration is added, and the solution is brought to 0.5 M NaCl, 0.01 M PBS, and 0.01% SDS. It is then heated for 30 minutes at 70 °C and then allowed to cool to room temperature to anneal the anchor and linker strands. At this point

the rod solution is centrifuged and concentrated to 10 nM as determined by UVvis. This solution is stable for weeks to months. Even if the rods settle out, they can be vortexed to be re-dispersed, and behave normally.

Appendix 5: DNA Based Assembly of the Metamaterial

Note: Even after developing the PMMA following the second layer exposure, there is a small residual layer of PMMA in the trenches that are covering the 'exposed' portion of the parallel rods. It is critical to do a brief O_2 plasma etch of the residual PMMA on the region of interest on the parallel rods. If this step is not done, gold parallel rods remain buried and the thiol groups on the DNA cannot bind to the surface.

The slide with the parallel rods and the trenches for the orthogonal rods is exposed to oxygen plasma (Harrick) for 30 seconds on low.

DNA addition to the gold parallel rods is slightly modified from previous protocol and proceeds as follows.[95] DNA B Anchor is treated for 60 minutes with 0.1M DTT, and purified through a NAP-5 column, and is brought to a final concentration of 1 µM in a buffer solution of 0.5 M NaCl and 0.05 M PBS. 500 µL of this solution was dropped on the region of interest using a micropipette and was placed in a covered petri dish overnight with a smaller petri dish full of water to increase the humidity and discourage evaporation. The glass slide is then submerged in MilliQ water to remove nonspecifically bound DNA B Anchor, quickly dried with nitrogen gas, and is placed back in the dry petri dish. Linking buffer (0.5 M NaCl, 0.01 M PBS, 0.01 % SDS) with 0.5 µM Linker B DNA is added to the region of interest with a micropipette. The covered petri dish was placed on a pre-heated hot plate set at 70 °C for 30 minutes to allow for DNA hybridization and annealing, and was then removed from the hotplate to cool to room temperature. At this point, excess buffer is very carefully pipetted off and/or blotted off with a technicloth, *but the lithographed region of interest is not dried so salt does not crystallize on the slide.*

50 µL of 10 nM rods previously functionalized with A linker DNA is placed on the region of interest for 3.5 hours in the covered petri dish. (Three hours is necessary for high yield binding, while after four hours the edges of the droplet begin to dry on the PMMA surface, making dark field difficult as they are highly scattering.) The slide is then rinsed with linker buffer, followed by submersion in linker buffer overnight and additional vortexing to remove rod that non-specifically bound to the PMMA. Afterwards, the back of the glass slide is cleaned with MilliQ water and dried (to eliminate the danger of salt crystalizing on the back of the slide) and excess linking buffer is blotted off the front.

Appendix 6: Flow Cell Assembly

Flow Cell Materials:

Glass Slides (Fisher, 75 mm x 25 mm x 1 mm, cat. # 12-550D), Glass coverslips (Fisher, 24 x 60 mm, 0.13-17, cat. # 12-545-M). Technicloth (TX609). Devcon 5 minute epoxy, Quick Dry Top coat (Revlon ®), Permanent Double sided tape (Permanent Scotch, 3M), Tubing (0.58 ID x 0.960 OD, wall thickness 0.2 mm), Syringe (3mL luer lock, Norm-Ject cat # ??), Needles (22G 1½ short bevel premium glide, BD, cat # 305159), Teflon tape (Swagelok PTFE, cat # MS-STR-8), and Immersol 518 F (Ziess) was used as microscope immersion oil.

Flow Cell Assembly

A thick glass slide (75 mm x 25 mm x 1 mm) that has two 2 mm holes drilled in it (1 cm from each outer short edges, and 12.5 mm in from the long edges) to form the inlet and outlet. It is then sonicated with acetone and IPA for 20 minutes each, vigorously dried under nitrogen, and is submerged for 5 minutes in fresh piranha. It is cleaned in copious amounts of MilliQ water, briefly dipped in IPA, and is then dried under nitrogen gas. Finally, it is subjected to O_2 plasma treatment for three minutes on high. Two needles (22G 1½ short bevel premium glide) are bent 90 degrees using pliers, and are glued over the drilled holes using epoxy. To prevent leaks, top coat (Revlon ®) is coated over the epoxy. The slide is then flipped over and placed in a 3D printed stand. On the back, four strips of permanent double sided tape are placed to define the edges of the flow cell. Excess tape is cut off by a razor blade. *It is critical to make sure that no tape sticks out over the edges, as the tape is leaky when wet and will later need to be completely sealed.* This top of the flow cell is placed on the ITO slide with the region of interest within the taped off channel. The top and bottom slide are sealed together with epoxy, followed by several layers of Revlon ® top coat. Tubing (0.58 ID x 0.960 OD, wall thickness 0.2 mm) is then connected to the inlet and outlets, and linker buffer is flowed through to test for leaks, which are then sealed with the Revlon ® top coat.

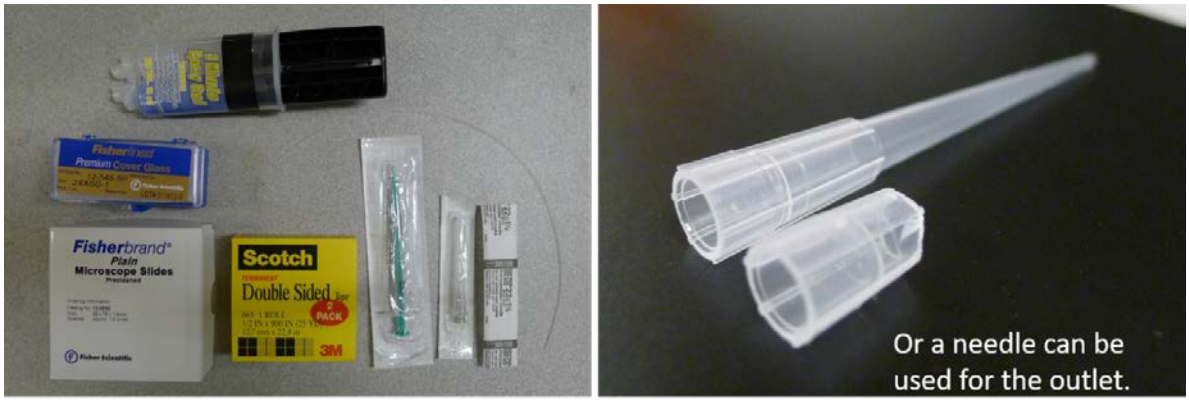

Figure S.0.1: Materials for flow cell. I prefer to use a needle for both the inlet and outlet so the waste material can be captured in the vial. This I important for the intercalator work where the intercalators can be highly toxic.

Safety note: *It is important to flow in using a syringe with a luer lock to prevent leaks, and the outlet tubing is connected to a septa capped vial.*

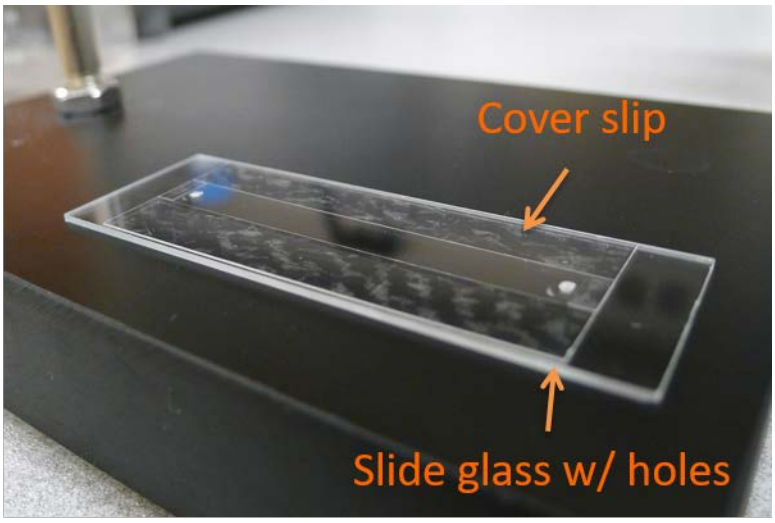

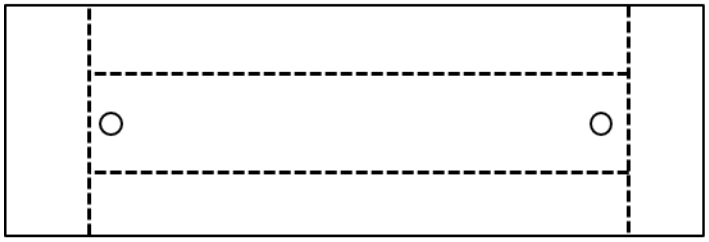

Figure S.0.2: Schematic of putting tape on the glass slide.

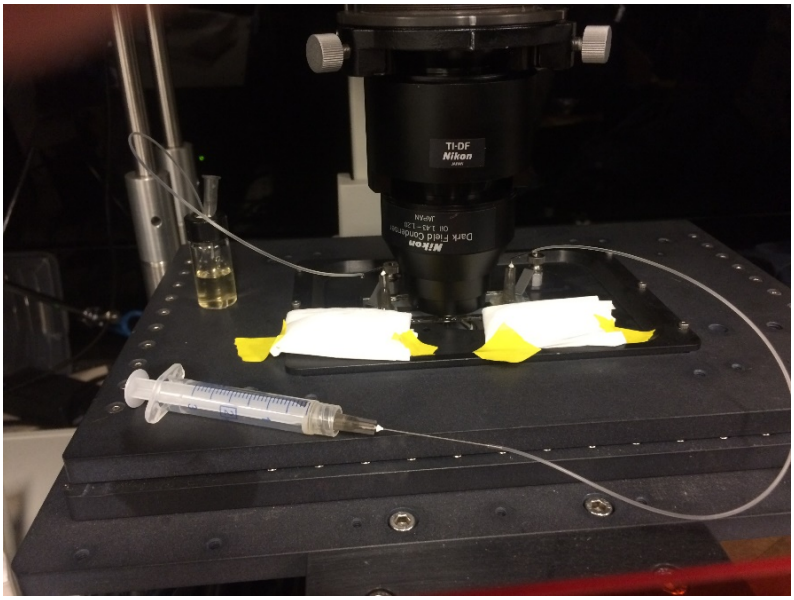

Figure S0.3: Assembled flow cell in the dark field.

Appendix 7: Hydrated/Dehydrated Dynamic Procedure

The ITO covered glass slide with the assembled EITs and intact PMMA are made as described in Appendix 2. 50 µL of linking buffer is applied to the region of interest. A new coverslip is sonicated for 20 minutes in acetone and IPA, vigorously dried with nitrogen gas followed by 5 minutes in piranha. It is copiously washed with water, and briefly dipped in isopropanol and dried with nitrogen gas. It is then treated for three minutes under O_2 plasma on high to make it hydrophilic. This top coverslip is then placed on the ITO slide, and the buffer is spread evenly between the two. A piece of Teflon tape is wrapped around it to act as a white light scattering object (see Section 6.5: MATLAB Processing and Analysis).

The slide and coverslip are then put in a transmission mode dark field microscope for single assembly imaging.

After imaging, the slides are taken out of the dark field microscope, the immersion oil is washed off the top coverslip with isopropanol, and the whole assembly is immersed in linking buffer so the two slides can be separated carefully with tweezers.

Next, the slides are prepared for scanning electron microscopy by removing salt with ammonium acetate and are put in a vacuum desiccator. The slides are then submerged in acetone to remove the PMMA (this also dehydrates the DNA). It is followed by rinsing in IPA and dried under nitrogen flow. When the sample is mounted in the SEM, it is exposed to high vacuum, ensuring that the DNA is completely collapsed. During SEM, the correctly assembled structures are identified and matched to their spectra (this is facile as the structures are in ordered arrays, so one can figure out the position in both the dark field and in the SEM to make sure the coordinates of the structures match).

Once the slide is taken out of the SEM, this dehydrated sample is placed back in the dark field (but upside down) and the immersion oil is placed on the back of the slide. Dark field is taken of the structures of interest as identified by SEM and by dark field in the hydrated state, and the spectra of the hydrated and dry states of the EIT structures are compared.